PAGE DE GARDE DE DUG TYPE
TOUTES CES INFORMATIONS SONT NÉCESSAIRES POUR LA CONFORMITÉ DU DIPLÔME

2021

DIPLÔME D'UNIVERSITÉ DE GEMMOLOGIE

présenté
devant l'Université de Nantes
U.F.R. des Sciences et des Techniques

par
M. Léonard CORNUZ

The relationship between the geological context and the inclusions found into the emeralds of the Mingora district (Swat Valley, Pakistan).

soutenu publiquement le *9 juin 2021*
au Département des Sciences de la Terre et de l'Univers
devant la commission d'examen composée de :

M. E. FRITSCH	**Professeur des Universités**	**Président**
M. C. LATOUCHE	**Maître de Conférences des Universités**	**Vice-Président**
M. C. EWELS	**Directeur de Recherche CNRS-IMN**	**Examinateur**
M. S. KARAMPELAS	**Chef Gemmologue au LFG**	**Examinateur**
M. F. NOTARI	**Directeur du GGTL-Genève**	**Examinateur**
M. B. LASNIER	**Professeur émérite**	**Invité**

«Wenn wir einen Kristall zu Boden werfen, zerbricht er, aber nicht willkürlich, er zerfallt dabei nach seinen Spaltrichtungen in Stücke, deren Abgrenzung, obwohl unsichtbar, doch durch die Struktur des Kristalls vorher bestimmt war. Solche rissige und gesprungene Strukturen sind auch die Geisteskranken.» (Freud, 1948)

Contents

Acknowledgements

I would like to specially thank Franck Notari for suggesting the topic of the emeralds of Mingora, for providing samples from the GGTL collection, for taking care of the import of the rock samples, for allowing me to spend hours at the microscope in his office, for giving full access to the GGTL Laboratories for sample preparation and analyses, and of course for sharing his passion for gems through countless valuable pieces of advice. I would also like to thank the whole GGTL team for their enthusiastic help and advice regarding the guideline for the analyses when I was on-site, especially Dr. Eric May to answer nicely to my numerous and disparate inquiries, at any time of the week. I would like to thank Jean-Claude Michelou, although no longer with us, for his advice, information about the ongoing mining methods in Swat Valley and also for the arduous sampling and export. On the Lausanne University laboratories side, I would like to thank Benita Putlitz for the great help and time allowed for correct sample preparation. I also thank Martin Robyr for his availability and explanations about the specificities of the microprobe, and Pierre Vonlanthen for his great help with the SEM and for his time to explain the important matters, from the first analysis to the data export. I would also like to thank Laurent Nicod and Youness Zangui in the thin section lab for their time to prepare/show me how to correctly prepare my samples. On the side of the mineralogical Museum of Lausanne, I would like to thank the Curator Nicolas Meisser for his exhaustive explanations on mica and chlorite composition. On the Nantes University side, I would like to thank Prof. Fritsch for the quality of his various teaching during the DUG weeks and his availability during the rest of the time and Laurent Lenta for the preparation of the thin sections. Furthermore I would like to thank Marie-Agnès Béal (AB Collection, Rolle, Switzerland) for helping me to cut/polish part of my samples for the microscope observations. I would like to thank Jules Reymond for the careful re-reading and my mother for her Adobe Suite lessons and advice on the layout. I would also thank Friedrich Menges for a complete and time-limited spectragryph license for the duration of the study. And of course I would like to thank my DUG promotion for the good moments spent in Nantes.

Acronyms and Abbreviations

Minerals

bt: biotite
cr: chromite
cpy: chalcopyrite
cal: calcite
chl: chlorite
em: emerald
fuc: fuchsite
FI: Fluid inclusions
gt: goethite
dol: dolomite
mag: magnesite
ms: muscovite
qtz: quartz
rut: rutile
tlc: talc
tur: tourmaline
phl: phlogopite
py: pyrite

The minerals abbreviations are derived from Chapter 12 of IUGS Subcommission on the Systematics of Metamorphic Rocks (SCMR) (Siivola and Schmid, 2007)

Geology
I-type: Granite from an igneous source
ITSZ: Indus-Tsangbo Suture Zone (Nepalese/Indian suture)
MMT: Main Mantle Thrust, or Indus Suture mélange group
MMTMG: Main Mantle Thrust (or Indus Suture) mélange group
MR: mafic rocks
S-type: Granite from a sedimentary source
UMR: ultra-mafic rocks

Instruments
EDX-SEM: Energy-Dispersive Scanning Electron Microscope
ED-XRF: Energy-Dispersive X-ray fluorescence spectrometry
FTIR: Fourier-Transform Infrared spectrometry
LA-ICP-MS: Laser Ablation–Inductively Coupled Plasma-Mass Spectrometry
LIBS: Laser-Induced Breakdown Spectroscopy
SIMS: Secondary ion mass spectrometry
PL : Photoluminescence
UV-Vis-NIR spectrometer : Ultraviolet-Visible-Near Infrared spectrometer
XRD: X-Ray diffraction

Others
BSE: Backscattered electrons
DUG: Gemology Diploma in Nantes University (http://www.gemnantes.fr)
e-ray: extraordinary ray
Ltd.: Private limited company
o-ray: ordinary ray
PPL: Plane Polarized Light
RI: Refractive Index (n)
RL: Reflected Light
SE: Secondary electrons
SG: Specific Gravity [g/cm^3]
XPL: Crossed Polarized Light

Introduction: motivation of the study

The following experimental study is part of the DUG (Gemology Diploma in Nantes University) under the supervision of Prof. Emmanuel Fritsch (IMN, Nantes University, France) and Franck Notari (Managing director of GGTL Laboratories, Geneva, Switzerland). The study focuses on the relationships between the emeralds of Mingora (Swat Valley, Pakistan), their inclusions and the local lithologies. The optical proprieties of the Mingora emeralds will be also investigated, as well as their chemical composition and the spatial association of their inclusions. The observations and analyses on the Mingora emeralds will be compared with the observations and analyses accomplished with the rock samples of the bearing-lithologies.

The subject is interesting for several reasons. First the growing interest for colored stones mining and for emeralds as well: the value per carat for gem quality emeralds has reached high prices and allowed to start large scale mining operations on large deposits. The actual interest can be illustrated by the auctions held in Lusaka, Zambia in October 2017 by Gemfields Group Ltd., with a US$21.5 million profit (Giuliani et al., 2018), or by the discovery of giant emerald pieces such as *Inkalamu* (5,655 ct) in Zambia (Gemfields 2018 report). Another example is the purchase of assets in the Coscuez Mine by Fura Gems in November 2017 (Fura 2018 report). The second reason regards the reports issued by gemological laboratories. Reports specify the origin determination on demand; the value of the emerald may change drastically for a similar quality/size stone, depending on the geographic origin and mining areas, due to historical factors or popular culture (Karampelas et al., 2019). Certification is getting trickier with the numerous emerald occurrences around the world, sometimes with overlapping similarities due to the same formation context (Giuliani, 2000). In-deep studying of an emerald's features, such as its chemical fingerprint and its distinctive inclusions due to the genetic host rock will add identification keys for a reliable origin certification. Small chemical features (e.g. trace elements) are powerful tools when combined with other advanced methods to detect an origin (Karampelas et al., 2019). Some significant deposits around the world are already broadly studied but others are lacking gemological reviews or have not been updated for several decades. This is the case of the Mingora area (Gübelin, 1982; Henn, 1988; Kazmi and Snee, 1990). Moreover the characteristics of emeralds (color, quality) tend to change after years of exploitation due to the heterogeneities of the deposits. Thus updates are needed. Fortunately the accuracy, affordability and size of advanced equipment in gemological laboratories have evolved during the last decades and now allow for precise routine measurements. Undoubtedly, in the future gem labs will be able to make use of more and more advanced equipment, used only experimentally at the moment, and the quantity and quality of data will be the critical point. A last reason is the interesting mingling of gemological data (e.g. inclusions description) with geological data (e.g. accessory minerals occurring along emeralds). This can highlight similarities but also help to complete the big picture of the formation of the emeralds.

The Mingora emerald district still has a lot of other potential prospects, and the data obtained will maybe help to explore other emerald deposits in comparable host rocks (Arif et al., 2010). My motivation for this study was based on my personal interest in gemstones deposits and helped by my geological background in ore deposits. The viability of the study was induced by the cooperation of different actors. The availability of emerald samples as research material out of the Mingora deposit was possible by the purchase by the GGTL Laboratories from Imperial Colors Co., Ltd.. Rock samples of the local host rock were provided by Imperial Colors Co., Ltd.. The availability of the instruments of GGTL Laboratories, along with the instruments of both Nantes and Lausanne Universities made the analyses present in the study possible.

Context of the study

Proprieties of emeralds

Generalities

The beryl group is part of the cyclosilicates, it includes different gem varieties; the green V-Cr-rich variety being emerald. Schwarz and Schmetzer (2002) defined emeralds as "yellowish green, green or

bluish green, natural or synthetic beryls, which reveal distinct Cr and/or V absorption bands in the red and blue-violet ranges of their absorption spectra.". The pale green beryl is not considered as emerald because the color is provided by Fe only (Hänni, 1991; Smith, 2009). The refractive index (RI) varies between 1.577-1.583 (+/- 0.017), with values up to 1.59-1.60 for particular sources (Zambia, Madagascar, Pakistan). Birefringence (δ) is between 0.005-0.009 and specific gravity (SG) is set at 2.72 g/cm^3 (+0.18/-0.05) (Gemological Institute of America, 2016). Because of their distinctive crystal structure, emeralds are part of the hexagonal system (point group 6/m 2/m 2/m). Their habits are either massive aggregates or hexagonal columnar crystals, with 6 first-order prismatic faces ({1011}), 2 pinacoidal faces ({0001}) and rare additional second-order prism faces ({1012}, {1122}) (O'Donoghue, 2008). The 6 first-order and the 2 pinacoidal faces coincide with the 6 prismatic growth sectors and the 2 pinacoidal growth sectors (Fig. 1) (Giuliani et al., 2019). Emerald gem crystals often contain a large amount of fissures or even cavities, which affect their clarity and retail value. The common treatment is executed by application of polymer, wax, oil or resin in order to fill the voids (Chen et al., 2016).

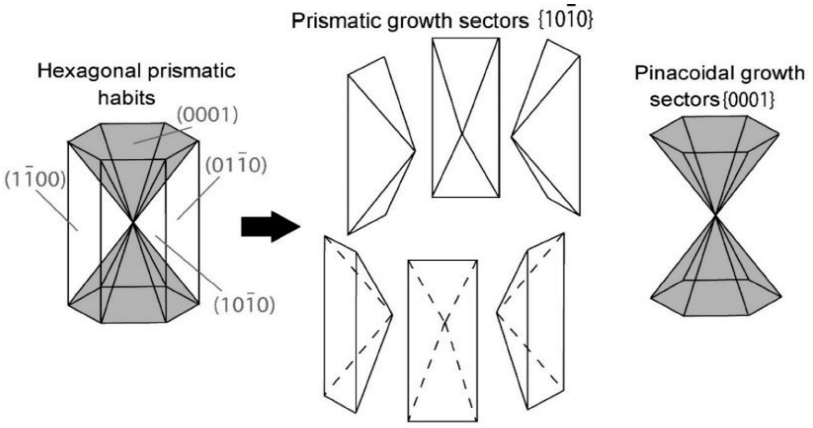

Figure 1: The common prismatic habit of beryl, with the 6 prismatic and 2 pinacoidal crystal faces and the different related growth sectors (Giuliani et al., 2019).

Chemical proprieties of emeralds and analytical methods

The ideal chemical formula of beryl is $Be_3Al_2SiO_{18}$. The crystal structure of emerald is made of parallel planes (0001) of linked rings of 6 silicate tetrahedra. The stacking of these silicate rings form large hollow channels parallel to the C-axis, where different ions or molecules are trapped (alkali ions, H_20, CO_2, noble gas). Cavities have a variable diameter and the positive ions in the channels balance the charge when a substitution occurs in the structure. These substitutions may occur as Be^{3+} sites replaced by Li^+ (Aurisicchio et al., 1994) or more often $^{IV}Al^{3+}$ sites replaced by Fe^{2+}, (Mg^{2+}, Mn^{2+}), Cr^{3+}, V^{3+}, Ti^{4+} (Groat, 2014). Substitutions for Cr^{3+} can vary from 25 ppm concentrations (Wood and Nassau, 1968) to 34'000 ppm (Andrianjakavah et al., 2009). Concentrations of V^{3+} vary from 34 ppm to 10'000 ppm (Rondeau et al., 2003). Other ions can also occur as traces in the crystal structure, such as Ce^{3+}, Sc^{3+}, La^{3+}, Rb^+, Cs^+ (Giuliani et al., 2019). Chemical substitutions, for both majors and trace elements (<100 ppm), are helpful to check the authenticity of the gem, to understand its geological growth context and also potentially to determine its origin. Therefore chemical analyses are a powerful tool for emeralds and the desired accuracy of the instrument is decisive. But budget limitations, induced micro-damages and daily ease of use also need to be taken into account. Previously confined to specific domains (e.g. universities) because of their price or regular operating challenges, some advanced analytical instruments are nowadays purchased by gemological laboratories and new standards are developed for this new specific application. For example, ED-XRF (Energy-Dispersive X-ray fluorescence), already in use in many other applications (metallurgy, food industry), identifies the minerals/atoms with a non-destructive incident spot of X-rays (1-10 mm Ø) and the resulting global fluorescence. The quick acquisition of major/minor element data (Na to U), little preparation needed and entry-level price (depending on the manufacturer) of ED-XRF all make for a useful tool in gemological laboratories.
On the other hand, the following instruments are still used more for research purposes than for routine analyses in gem labs: standardless EDX-SEM (Energy-Dispersive on a Scanning Electron Microscope) is used for discrete semi-quantitative microanalysis or chemical maps of major/minor elements (Na >). The detection of the elements is done by an electron beam (Ø ~1 µm) hitting the surface of the sample

in a high vacuum, producing backscattered electrons (BSE), secondary electrons (SE), X-rays and photons. BSE are used to calculate elements percentages on the spot. The operating costs, preparation of the samples (coating process) constant quality of the high vacuum, size limits in the chamber and micro-damages induced by the high voltage electron beam (2-8 µm deep) need to be weighed with its exceptional capacities.
The Electron Probe Microanalyzer (EPMA) method is close to that of the EDX-SEM but produces quantitative analyses (B to U). An electron spot beam (Ø 1-2 µm) hits the sample in high vacuum and multiple WDS (Wavelength-Dispersive) crystal spectrometers collect X-rays/electrons. Analyses lead to micro-loss (visible damage with SEM), and precise measurements require perfect polishing and flatness of the sample.
Other notable methods are LIBS (Laser-Induced Breakdown Spectroscopy) or LA-ICP-MS (Laser Ablation–Inductively Coupled Plasma-Mass Spectrometry) to analyze trace elements, and SIMS (Secondary ion mass spectrometry) for the analysis of isotopes (DUG sessions 2018-2019, pers. comm by the operators, 2018-2019).

Usual inclusions in emeralds and determination

The inclusions found in emeralds are denominated as the "jardin" (*garden* in French) and can be of different nature. Fluid inclusions (FI), negative crystals, solid inclusions (minerals) or healing fissures or fractures are part of the landscape observed in the emeralds. inclusions depend on the geological growth context and on the introduction timing; they can be proto- (before), syn- (during), or epigenetic (after the mineralization of the emerald). For this reason, the nature and composition of the country host-rock and the incoming mineralizing fluids (pressure, temperature, salinity) play a key-role in providing the different elements forming the inclusions. For example, the common paragenetic internal assemblage in contact metamorphic emerald-types are minerals from the mica and amphibole group (Schwarz, 1994). The hydrothermalism depending on the type of context forms different inclusions: in a metamorphic-metasomatic context in metamorphic rocks it produces calcite and dolomite, but in a metasomatic-hydrothermal-type in sedimentary rocks it forms albite, calcite, dolomite, pyrite and a lot of multi-phase FI. To identify the paragenetic assemblage without damaging the host emerald, few methods are useful; microscopy can tell more about the habit of the inclusion (Gübelin and Koivula, 1997), Laser Raman Microspectrometry allows to measure the vibrational nature of the inclusion (Le Thi Thu, 2008) and Microthermometry gives insights on the salinity of FI (Marshall et al., 2016). All these methods bring up supplementary clues, helping for origin determination. Other methods, as mentioned in the previous chapter, can precisely analyze the chemical composition of the inclusion, but may damage the host if the inclusion is not outcropping.

Rock samples and chemical analyses

Regarding rock analyses, most of the microanalyses on the gems are also applied on rock samples (ED-XRF, EDX-SEM, EPMA, LA-ICP-MS). As for the microscopy in the gemological laboratory, the first observations are also carried out on thin sections of the interesting rock samples (Sturm, 2010). Thin sections are made by sawing the rock sample and then polishing it until its thickness reaches 30 µm, which allows light to pass though. The rock preparation is then glued on a piece of glass and sometimes covered (for transmitted light observation only). Microscopy is an effective way to judiciously prepare the next steps of microanalyses. When whole rock analyses are wanted, XRD (X-Ray diffraction) is helpful to analyze the major elements of a rock sample. The sample needs to be finely crushed and packed in a holder, then placed under an inclined and moving X-Ray source. The inclined detectors capture the produced diffracted X-Ray wavelengths and identify the percentage of each mineral phase present in the sample (DUG sessions 2018-2019, pers. comm by the operators, 2018-2019).

UV-Vis-NIR, FTIR, PL, Raman spectrometry applied to emeralds

The optical proprieties of emeralds are directly linked to the crystal structure and the chemical composition. The color is often the result of one or a combination of several elements (Fritsch and Rossman, 1988) and the absorptions of the ordinary (o-ray) and extraordinary-ray (e-ray) give valuable indications about the estimated chemical composition and, thus, the origin of the color. The instrument

used is a UV-Vis-NIR (Ultraviolet-Visible-Near Infrared) spectrometer, which evaluates the absorption of an incoming UV-white light through the sample. The spectral fingerprint of the emeralds is another valuable characteristic to determine the geological growth context (and mining sources), because small variations of chromophore elements influence the final absorption and color. For this reason, Smith (2009) (Fig. 2) classified emeralds based on their color-causing mechanisms and added general locations; Class I if for Colombian emeralds, Class II for Afghanistan, Zimbabwe (Sandawana), Class III for China and others and Class IV for Nigeria and others.

As seen before for the chemical analyses of the inclusions, other methods are used to identify and characterize the emeralds by vibrational spectrometry. FTIR (Fourier-Transform Infrared spectrometry) is the spectral absorption or emission in the IR domain of a sample, useful for the detection of impregnation and for the sourcing (Qiao et al., 2019). Raman spectrometry is another method used to determine the nature of the material, with a laser-excitation followed by the acquisition of the Raman effect (Bersani et al., 2014). PL (photoluminescence) analyzes the PL emission of emeralds under a laser source and can be used for the identification of the origin of emeralds (Thompson et al., 2017).

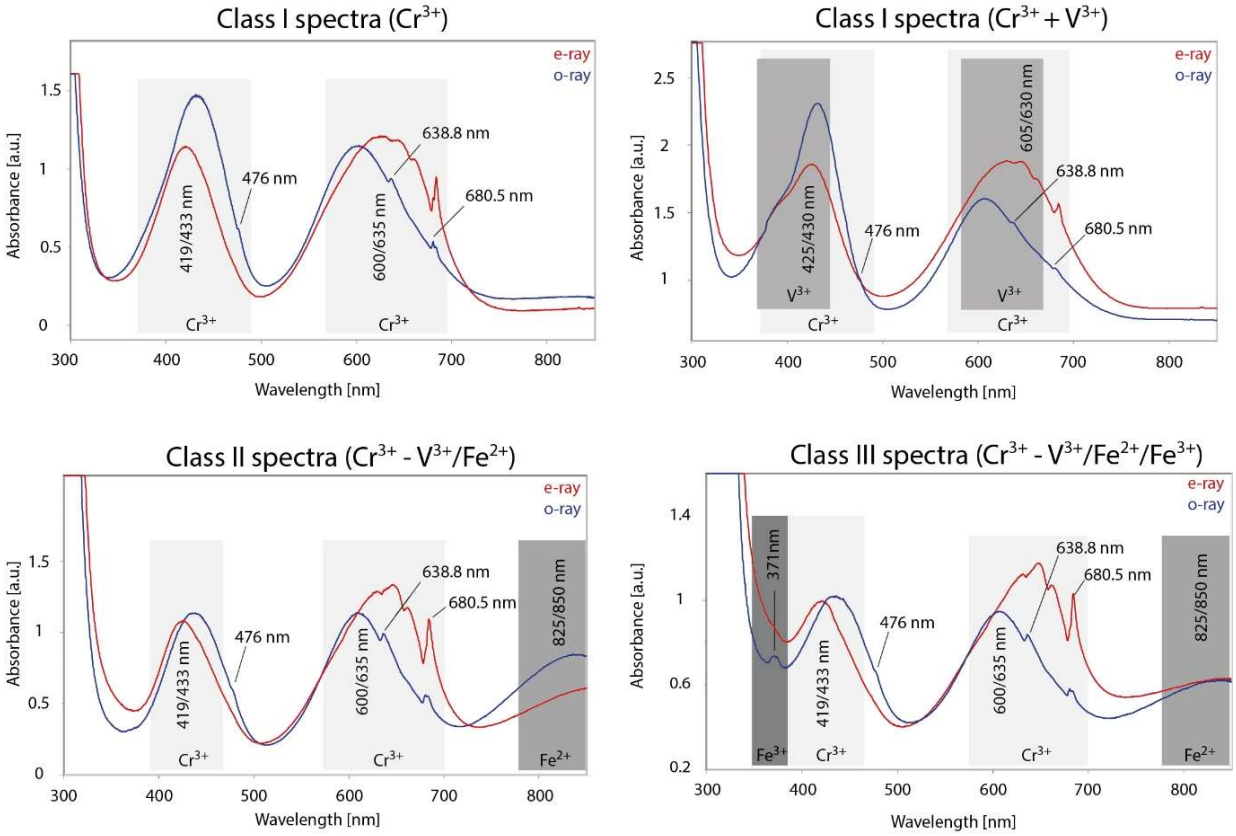

Figure 2: UV-Vis-NIR absorbance graphs for spectral classification in Smith (2009) (modified after original data). ***Class I*** *shows Cr^{3+} absorption only, or with V^{3+}.* ***Class II*** *shows the absorption of Cr^{3+} and potentially V^{3+}, and various Fe^{2+} absorption depending the source.* ***Class III*** *shows the combination of the absorption of Cr^{3+}, potentially V^{3+} and both oxidation state of iron.* ***Class IV*** *(not represented in the article) is the rare combination of V^{3+} only and both oxidation state of iron.*

Worldwide emerald deposits and genetic models

Emeralds are found in few economic deposits around the world, but occur on the five continents, and certainly Antarctica (Anderson, 2013; Reeves, 2014). The types of geological processes creating these deposits are not linked, as expressed by their respective ages or by their hosting lithologies (2,96 Ga for Gravelotte's oldest emerald deposit in South Africa, 9 Ma for Khaltaro's youngest deposit in Pakistan) (Giuliani et al., 2019). In 2019, the biggest emeralds producers are situated in Colombia, Brazil and Zambia, each of these giant deposits having specific geological features. The formation of emerald is the result of the fortuitous interaction of different geochemical reservoirs; the needed elements are

beryllium (Be), found in the continental lithosphere (crustal granites and pegmatites, aplites, quartz veins) and chromium (Cr) and vanadium (V), which are preferentially found in oceanic lithosphere (mafic or ultra-mafic rocks, abbreviated M-UMR, such as dunite, lherzolite) (Giuliani et al., 2018). When the fore-mentioned elements and the right pressure/temperature conditions occur, the formation of emerald may occur. Giuliani (2019) classifies the formation environment in several genetic types: type I (tectonic-magmatic) accounting for ~ 65% of the world production, type II (tectonic-metamorphic) can either be type IIA (7% of world production, e.g. pegmatites in M-UMR in Brazil) or IIB (28% of world production, e.g. black shales in Colombia) (Giuliani et al., 2018).

Proprieties of Mingora emeralds

Generalities

Mingora emeralds are found as aggregates or single crystals mixed with the hosting assemblage; they form clusters with various levels of resorption (Kievlenko, 2003). Their color may vary from pale to deep green, with a distinctive bluish-yellowish dichroism (Fig. 3), and can be heterogeneous with sharp concentric color transitions (Behmenburg, 2001; Kazmi and Snee, 1990). A specific feature of the Mingora emeralds is their high refractive index (n_o=1.582-1.591, n_e=1.590-1.602, δ = 0.007) (Gübelin, 1982). These high RI values can be explained by the presence of alkali ions, water, and substantial Mg and Fe (Wood and Nassau, 1968). Their specific gravity ranges between 2.74-2.78 g/cm^3 (Kievlenko, 2003) and they lack luminescence under SW-LWUV because of high Fe content (Kazmi and Snee, 1990).

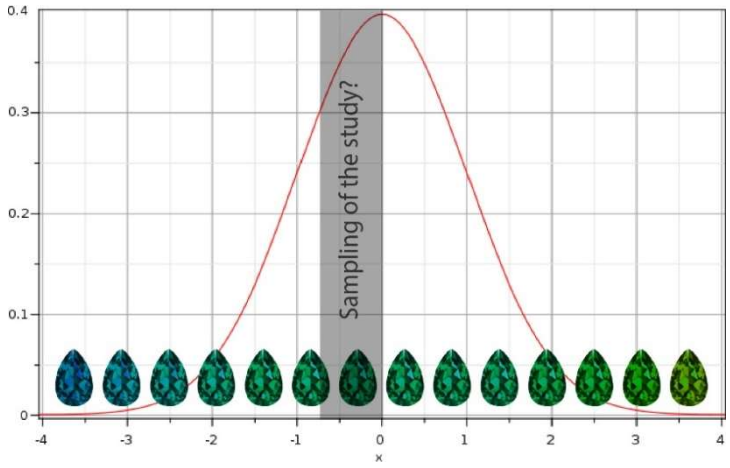

Figure 3 : Theoretical gaussian distribution of the color of gems extracted from a single deposit. The selection bias will generalize the color for the whole deposit only based on the few collected samples (modified after Franck Notari's talk during DUG sessions).

Mine	Mingora (2)		Mingora (1)	
Sample	SDA-25		SEM 51-53/P3	
No. of grains	2		1	
No. of analyses	51		22	
Composition	mean	s.d.	mean	s.d.
SiO_2	62.8	2.2	62.7	1.7
Al_2O_3	13.1	0.5	14.2	0.5
FeO	0.91	0.21	0.52	0.05
MgO	2.50	0.32	2.46	0.11
CaO	0.01	0.01	0	
Na_2O	2.06	0.18	2.11	0.11
K_2O	0		n.d.	
TiO_2	0.01	0.01	0.01	0.01
MnO	0		0	
V_2O_3	0.04	0.01	0.06	0.03
Cr_2O_3	1.17	0.42	0.39	0.45
F	0.02	0.03	n.d.	
Cl	0.01	0.01	n.d.	
BeO(calc)[1]	13.0		13.1	
BeO[2]	9.49		10.49	

Figure 4: Microprobe analyses on Mingora emeralds (after Kazmi and Snee, 1990, modified).

Chemical proprieties of Mingora emeralds

The chemical composition of Mingora emeralds shows the biggest Mg-Na-Fe content found in emeralds (Mg/(Mg+Fe) ratio at 0.8), high Cr content (< 2 wt%), no or close to no vanadium (< 0.02 wt%), some Sc (0.5 wt%) and no F or Cl (Arif et al., 2011; Behmenburg, 2001; Giuliani et al., 2018; Gübelin, 1982; Kazmi et al., 1986; Kazmi and Snee, 1990). On Fig. 4, Cr shows strong chemical variations depending on the sample and a similar correlation between Mg and Na concentration is well-known (Karampelas et al., 2019).

Usual inclusions in Mingora emeralds

Mingora emeralds hold a multitude of specific inclusions, which help to their identification. Fluid inclusions (negative crystals, jagged-blocky two-phase, elongated growth tubes, two phases curved secondary, healing fissures parallel to the basal plane, zigzag lines), late basal fractures and solid mineral inclusions provide a large amount of criteria to identify them. Common solid inclusions occurring in "contact-metamorphic" emeralds are micas (biotite (bt)-phlogopite) and amphiboles (large range), which are derived from the host rock or brought during the volatile pegmatitic phase. The multiple late phases of hydrothermalism bring other carbonates (Gübelin and Koivula, 1997). Minerals which can be found as inclusions are carbonates (recrystallized sharp rhombohedral Fe-dolomite, Fe-magnesite, calcite), micas (fuchsite, biotite), the talc series (sharp monocrystal), the chlorite series, the amphibole series and the spinel series (chromite, hercynite, magnetite). Rarer inclusions are also present such as pyroxenes (enstatite), euhedral pentlandite, molybdenite, pyrrhotite, rutile, hematite, feldspar, antigorite, euhedral gersdorffite (Giuliani et al., 2018; Gübelin and Koivula, 1997, 2008; Kazmi and Snee, 1990; Schwarz, 1994; Schwarz and Pardieu, 2009).

Mingora deposit and genetic model

Figure 5: General map of Pakistan. Mingora is marked by the red star (©OSM).

The Mingora emerald mining area is in the Swat District, in the Khyber Pakhtunkhwa Province, Northern Pakistan (Fig. 5). The mining area (~200 m × 1000 m) is on the northeastern heights of Mingora City, situated along the Swat River, 160 km North of Islamabad. Nowadays, the expansion of Mingora City nearly encompasses the mining claims. The Mingora deposit is part of a larger emerald district, with numerous emerald deposits and prospects in the same lithologies (Fig. 6). Examples include the Alpurai-Lilaunai area, the Barkotkai village, the Gujar Kili village and the Spin Obo-Kuh area (Arif, 1999). The largest and most productive deposit is the Mingora deposit, followed by the Gujar Kili deposit. The general tectonic context is that of the closure of the Tethys ocean and the collision of the Asian plate with the Indian plate, causing the orogeny of the Hindukush-Himalaya-Karakoram mountain ranges and associated suture zones. The Nepalese/Indian suture is called the Indus-Tsangbo Suture Zone (ITSZ) and its continuity in Pakistan is called the Main Mantle Thrust (MMT). The collision and closure in Swat is estimated at 45 ± 5 Ma (Arif, 2003; Kazmi and Snee, 1990). This event is associated with post-collisional magmatism (I- type granitic intrusions) and related early hydrothermal fluid circulations at 32.7 ± 0.5 Ma (Di Pietro, 2008). These tectonic movements stacked numerous rock types of different origins together, such as a micro-continent, marine sediment sequences and series of an ocean floor. The different tectonic groups are (from North to South) the Kohistan Arc Sequence which is thrusted over the Indus Suture mélange group. This complex is then obducted onto the Indo-Pakistan plate along the MMT. The Kohistan Arc is composed of rock sequences from an intra-oceanic arc, such as amphibolites or the Kohistan gneiss batholith. The Main Mantle Thrust mélange group (MMTMG) is a mass of sediments from oceanic crust, continental margins and volcanic arcs (West to East: the Charbagh greenschist mélange, the Mingora ophiolitic mélange, the Shangla blueschist mélange). The Indo-Pakistan plate (Swat gneisses, Manglaur, Alpurai, Saidu schists) is an Indian subcontinent (Kazmi et al., 1986).

The Mingora deposit is located in the Mingora ophiolitic mélange (MMTMG group), stacked in-between the Charbagh greenschist mélange (West of the deposit) and the Saidu schists (East). Each mélange is separated by thrust faults (Fig. 6), slicing the whole into tectonic blocks (Arif et al., 2011, 2010; Kazmi et al., 1986). The Mingora mélange occurs sporadically as 10 to 100 m lensoidal bodies (Arif et al., 1996). It is made of a grey-green-white-brown fine to medium-grained chlorite(chl)-dolomite(dol)-

fuchsite(fuc)-magnesite(mag)-quartz(qtz)-tourmaline(tur) schist with clasts of greenschist, graphitic schist, serpentine, dolomite in a soft sheared foliated coarse matrix chlorite-talc(tlc)-dolomite schist. The deposit is heterogenous; the clast content of the schists changes depending on the location of the mine (preserved textures of pelagic sediments, pillow lavas in certain zones). The size of the clasts also changes (dolomite or serpentinite range from cm-lenses to several m-blocks) and the composition of the greenschist is variable (harzburgite, lherzolite, rare dunite) (Arif, 2003).

The lithology hosting the Mingora emeralds is a talc-magnesite-dolomite schist, covered by limonitization (Gübelin and Koivula, 2008; Kazmi et al., 1986). The bearing lithologies are striking N-S, dipping 25-75° West, and have a 50 m maximum thickness (Gübelin, 1982). The Mingora mélange protoliths underwent an early regional greenschist metamorphism (creation of the regional serpentinite-talc) and multiple episodes of hydrothermal activity (creation of the carbonate enrichment, of the quartz stockwork hosting mineralization and increased rock permeability). The semi-pervasive hydrothermal alteration (Si, Be, B, K, Ca transported by the fluids) presents a metasomatic zonal pattern: "An outer zone composed of talc-magnesite ± chlorite ± micas; an intermediate zone consisting of talc-magnesite with dolomite veins; and an inner zone with dolomite-magnesite-talc schists and quartz-dolomite ± tourmaline ± fuchsite veins. Emerald occurs disseminated in the inner and intermediate zones within or spatially associated with quartz-carbonate veins." (Giuliani et al., 2019). Thus, depending on the location of the mine, the metamorphic assemblage or the alteration may vary. In Mingora for example, the final alteration product is found, with only serpentinite blocks or talc-carbonate schists (Arif et al., 2011). These pervasive hot hydrothermal fluids are crucial for bringing Be(-B) in contact with Cr present in chromites in the serpentinites of the Mingora mélange. The question remains as to which rock supplied Be(-B) to the fluids: Arif et al. (2011) postulate for a hidden S-type granitoid pluton as a source, based on the beryl-bearing hydrothermal veins observed at Ilum Peak (25 km South Mingora). The age of the Malakand granite, as determined by $^{40}Ar/^{39}Ar$ muscovite is 22.8 ± 2.2 Ma (Maluski and Matte, 1984) which is close to the age of the fuchsite in em-qtz veins dated by $^{40}Ar/^{39}Ar$ at 23.7 ± 0.1 Ma (Dilles et al., 1994). Isotope values in emeralds are homogenous and present both magmatic and metamorphic signatures. However, δD values (fuchsite, tourmaline) of the Mingora deposit are close to that of the Malakand granites (fuchsite, tourmaline), supporting the theory (Arif et al., 2011, 1996). The estimated temperature of the mineralization fluids from the literature are various; the quartz+talc+magnesite assemblage is estimated in a range between 250-550°C (Arif et al., 1996), while the fluids are probably around 500°C (Schwarz and Pardieu, 2009). Based on the fluid inclusions, the crystallization temperature is estimated between 280-380°C (Kievlenko, 2003) or at 415 ± 18 °C (Kazmi and Snee, 1990). The mineralization is structurally controlled and suggests a formation during shearing and late-stage alteration. The emerald crystals occur as two main types (Fig. 7): earlier disseminated crystals in the ground mass of the talc-chlorite-dolomite schist, and fracture-filling/stockworks mineralization or around the tension gashes. The disseminated emeralds occur as small lenses/pockets (5-15 cm) between two parallel faults along shear zones. The fracture-filling is composed of small emerald(em)-qtz-calcite(cal) veinlets, at the fabric intersections or on the limonitized faults/joints. The stockwork is an abundant small em-tur-fuc-qtz veining. A minor occurrence is in a 15-30 cm layer of talcose around the qtz-filling of tension gashes, which could be associated to fracture-filling-type (Gübelin and Koivula, 2008; Kazmi et al., 1986). The mineralization is spatially associated with the contact between serpentinites and metasediment, sometimes inside the serpentinites. All this is crossed by abundant qtz-stockwork and qtz-veins (Arif, 1999).

To sum up the genetic model of mineralization, the deposit is hosted in a metamorphic ultramafic schist without pegmatite. Some metasomatic fluids followed deep structures in shear zones to reach the permeable mélange after leaching a S-granite intrusion. The Mingora deposit is classified as "Tectonic Metamorphic-Related Emerald Deposits Hosted in M-UMR" (Type IIA) or as "Tectonic Metamorphosed or Remobilized Type IA Deposits, Tectonic Hidden Granitic Intrusion-Related Emerald Deposits, and Some Unclassified Deposits" (Type IID) (Giuliani et al., 2019).

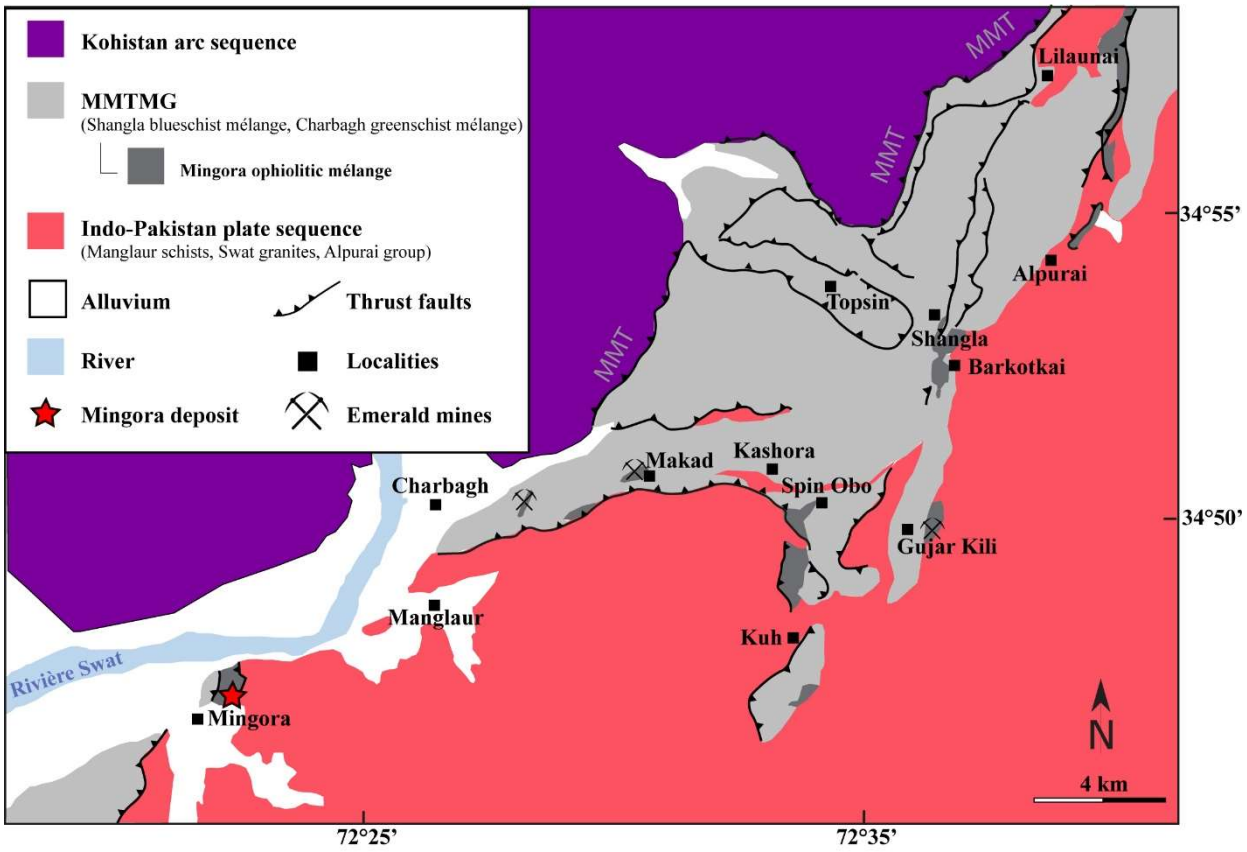

Figure 6: Tectonic map of the Mingora-Lilaunai area (after Arif and Moon, 2007, modified).

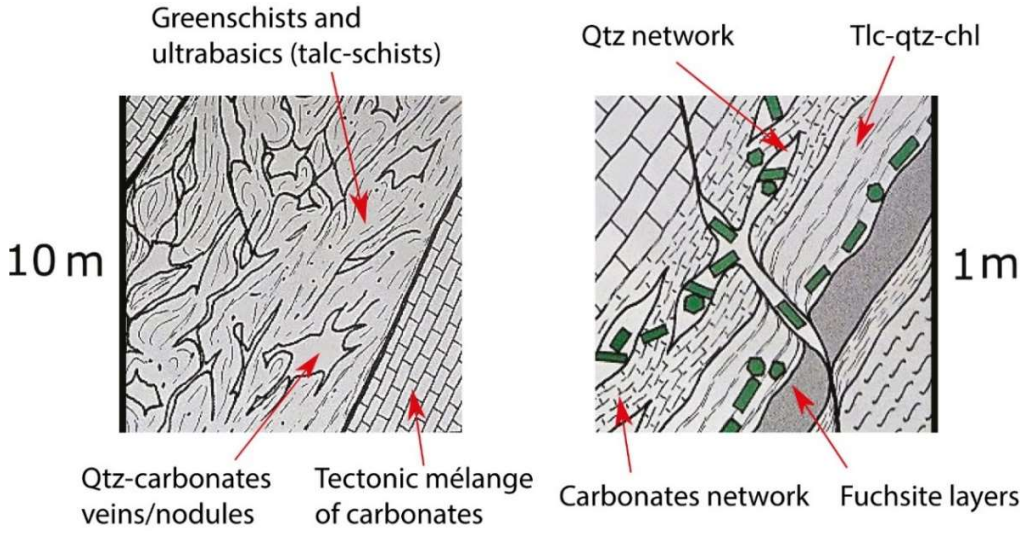

Figure 7: Model of "Schists without pegmatites: Emerald in carbonate-talc-schists and quartz lenses" for Swat, Pakistan (Schwarz, 2002, modified). Overview (left) and details (right).

Material and methods

Rock sampling and limits to the methodology

Due to restricted access to the extraction area, the sampling was accomplished by Imperial Colors Co., Ltd. in April 2019 (Fig. 8). A sampling list was elaborated based on different articles describing the mineralization and lithologies. The aim of the sampling was to collect the different minerals present close and away from the mineralization, and the minerals composing the mineralization itself. The side-objective to also sample the lithologies composing the deposit was left aside because of the amount of work and because of the meticulous description already accomplished with thin sections and precise trench sketches drawn in Kazmi and Snee (1990). The sampling list was set as follow: **1**) A piece of talc-magnesite schist with no mineralization associated, possibly with no alteration or quartz vein (Kazmi et al., 1986, p.3). **2**) Several serpentinite samples from the meter-long blocks stuck in the dominant talc-magnesite schist (Kazmi et al., 1986, p. 4). **3**) Samples of mineralized (ms-tur-em-qtz) veins. This sample will help to set the spatial distribution of the vein-hosted mineralization (Arif et al., 2011, p. 6, 2010, p. 5) **4**) Samples of the disseminated em-tur mineralization in the carbonate-talc schist. This sample will help to determine the spatial distribution of the disseminated ore (Arif et al., 2010, p. 5). **5**) A sample with metallic minerals (sulfurs, oxides) in the center of the mica sheets or in the quartz veins or disseminated in the host rock, preferentially visible to the naked eye (Arif and Moon, 2007, p. 3). The final collected samples only partially fulfill the fore-mentioned objectives, because of the sampling quantity, but give valuable information for that study. The gap between the sampling objectives and the in-field sampling is ordinary because of the heterogeneity of the deposit, and of the idealized description of the articles.

*Figure 8: **A** Mineralized section (Wall, LC-khalid-7). **B** Washing and sorting of the ore production of the day at Khalid Tunnel. **C** A miner with a jackhammer at Center Tunnel. (B-C Picture J.C Michelou)*

Description of the rock samples

The rock samples are of diverse types. There are fragments of soft oxidized leucocratic talc-schist with various composition and oxidation (fault breccias, unmineralized schist) to more melanocratic massive talc-schist (mineralized schist). There also are more competent fragments of emerald aggregates with quartz-feldspar veins, or of quartz veins with chlorite. One of the samples is the mine-run of the Khalid tunnel. Pictures and individual descriptions can be found in Annex III.

Choice of the emerald samples and limits of the methodology

The emerald samples from the GGTL collection were chosen for their ease of analysis with advanced instruments. Single translucent matrix-free crystals with a lot of inclusions were preferred, but smaller pieces were also selected to spot the maximum diversity of inclusions. The small thin stones helped for specific analyses such as UV-Vis-NIR spectrometry. The selection was carried out by Franck Notari with an immersion microscope in January 2019 on the inventory of Imperial Colors Co., Ltd. in Bangkok. The inventory of Imperial Colors Co., Ltd. was supplied in previous years by several tunnels of the Mingora mining area. The information about the exact location was not accessible. Since rock samples are not extracted at the same time or in the same zone as the emerald samples, a bias exists.

Due to the heterogeneity of the deposit, the size of the mining area and the specific geometry of the mineralization, the composition and the inclusions can change drastically depending on the samples. These variations can also be seen through color and clarity. As expected, and as for other studies, the limited number of samples also causes a selection bias and does not represent the whole deposit mineralization.

Description of the emerald samples

Figure 9: Emerald samples used for the study (ethanol, darkfield), with weight and dimensions.

The emerald samples for the study are single rough crystals (Fig. 9), with minor matrix and have a constant elongated hexagonal prismatic habit. Few of them are disproportionate (FN12490, FN12978) or etched on the surface (FN12976). Some samples display cluster growth (FN13156) or growth twinning (FN12979). The main part of the samples is severely included and not gem quality, except FN12984 which is a brilliant round cut stone. All emerald samples were extracted out of the Mingora deposit; the exact zone of extraction is not disclosed and the extraction date between the sample may vary. The emerald samples belong to the GGTL Laboratories (Geneva, Switzerland). The different analyses on emerald samples and rock samples are resumed in the annexes (XXIII, XXXIV).

Analytical procedures

Microphotography: The samples were either immersed into no-dust ethanol or let in air. In addition, optic fiber illumination was used in some specific cases and white balance was performed before each session. The microscope used was a Leica M205C Stereomicroscope, with "Z-stack program" for multifocus images. The scale was carefully merged on a second picture. The pictures were edited and enhanced with the Adobe Suite. **UV-Vis-NIR spectrometry:** The spectra were obtained on a 4-channels Asahi Spectra FHL-101, with an Exelita UV 300 W bulb and a white integrative sphere. Inside, a polarizing filter was added on the pinhole entrance and calibrated without the sample. Then the sample was stacked straight on a ring and set onto the polarizing filter in both orientations for 500 scans. **IR spectrometry:** The spectrum was acquired using a Bruker Vertex 70 FTIR spectrometer with a spectral sampling of 4 cm^{-1} for 100 scans. **Raman spectrometry:** For the FT-Raman data, the single spectrum was obtained using a Bruker MultiRAM FT-Raman Spectrometer, with a maximum power of 1 W and an accumulation of 500 scans at 4 cm^{-1}. Laser Raman Microspectrometry spectra were produced with a Horiba Jobin-Yvon LabRAM HR 800 spectrometer, with a green polarized laser beam at 532,1 nm (calibrated with silicate section) and 750 mW of maximum power as excitation source. The spectral acquisition time was 30 sec, without filter, through an Olympus optical microscope (x 50 large). The spectra were processed and identified partially using the Spectragryph-id v1.2.12 software with "excellent entries" of the RRUFF database (Lafuente et al., 2015). **XRF**: The data were acquired on an ED-XRF spectrometer Thermo Scientific ARL QUANT'X. the standards were either from Thermo Fisher or in-house standards (pure elements), and the parameters were set as routine analyses settings of the lab. A 2 mm-collimator was used (spot 3,5 x 3 mm). **EDX-SEM:** Backscattered electron images were taken using a Tescan Mira II LMU, operated at an acceleration voltage of 20 kV and a probe current of 1 nA. Standardless EDX analyses were carried out at a working distance of 21 mm using the AZtec 3.4 software published by Oxford Instruments. The carbon was taken out of the results and the analyzed spots were not located on a picture of the sample. The acquired data were sorted and the minerals named based on the bulk chemical composition tables and formulas of Deer et al. (2013). **EPMA:** The analyses were done on a JEOL JXA-8530F, with an acceleration voltage of 15 kV. For spot analyses, the beam size was 5 µm and the probe current set at 15 nA. For the Si, Al, Fe, Mg, Ti, Mn-detector, the analysis had a duration of 30 s on the peak and 20 s on the background. For the detector with K, Na, the analysis duration was 20 s on the peak and 10 s on the background. For the chemical maps, the probe current was set at 100 nA, with a dwell time of 40 ms. The maps are composed of 752x627 pts (3 µm/pt). **XRD:** The analyses were carried out on an ARL X'TRA powder diffractometer, with 0,02°-step between 2-65°, an integration time of 1,2 s and a scan rate of 1°/min.

Results

Classical gemology on emerald samples

The characteristics of the emeralds used for the study are presented in Fig. 10. The color grading was done naked eyes with a neutral background and based on Gemworld (2014). The clarity grading was also done naked eyes with a neutral background and based on GIA clarity grading chart (Type III-stones). Pleochroism colors were determined under microscope in no-dust ethanol with a polarized filter and based on Gemworld (2014) (Fig. 11). No fluorescence (LW, SW-UV) was observed on any samples.

Sample number	Color	Color distribution	Clarity	RI		Pleochroism	δ birefringence	SG [g/cm^3]
				n_o	n_e			
FN12490	Vivid slightly bluish green	Even	Severely included	1.56	1.6	Vivid slightly bluish green to vivid green	0.034	2.713
FN12491	Vivid slightly bluish green to vivid green	Uneven	Moderately included	1.59	1.6	Vivid bluish green to vivid green	0.012	2.756
FN12968	Vivid bluish green to strong bluish green	Even	Moderately included	1.59	1.6	Vivid blue green to vivid green	0.013	2.745
FN12969	Strong bluish green	Even	Severely included	1.59	1.59	Intense bluish green to strong blue green	0.006	2.760
FN12970	Strong bluish green to vivid green	Uneven	Severely included	1.59	1.6	Intense bluish green to strong blue green	0.009	2.785
FN12971	Vivid slightly bluish green	Even	Moderately included	1.59	1.59	Vivid bluish green to vivid green	0.007	2.743
FN12972	Vivid bluish green	Even	Severely included	1.58	1.59	Vivid blue green to vivid green	0.01	2.756
FN12973	Moderate bluish green	Even	Severely included	1.59	1.6	Intense blue green to strong bluish green	0.006	2.723
FN12974	Moderate bluish green	Even	Severely included	1.59	1.6	Moderate blue green to moderate bluish green	0.01	2.847
FN12975	Deep bluish green	Even	Severely included	1.59	1.59	Vivid bluish green to vivid green	0.006	2.759
FN12976	Dark green	Even	Severely included	1.58	1.59	Moderate blue green to moderate bluish green	0.008	2.835
FN12977	Light bluish green	Even	Severely included	1.59	1.6	Very light blue green to intense green	0.008	2.725
FN12978	Light bluish green to strong slightly bluish green	Uneven	Severely included	n.d.	n.d.	Light bluish green to light green	n.d.	2.983
FN12979	Intense slightly bluish green	Even	Moderately included	n.d.	n.d.	Light bluish green to light green	n.d.	2.724
FN12980	Intense slightly bluish green	Even	Severely included	n.d.	n.d.	Moderate blue green to moderate bluish green	n.d.	3.088
FN12981	Intense bluish green	Even	Severely included	n.d.	n.d.	Very pale green to light green	n.d.	2.683
FN12984	Vivid green to deep green	Uneven	Moderately included	1.58	1.59	Vivid bluish green to vivid green	0.011	2.734
FN13153	Vivid slightly bluish green	Even	Moderately included	n.d.	n.d.	Vivid green to strong bluish green	n.d.	2.673
FN13155	Vivid bluish green	Even	Moderately included	n.d.	n.d.	Vivid green to vivid bluish green	n.d.	n.d.
FN13156	Vivid slightly bluish green	Even	Moderately included	n.d.	n.d.	Moderate blue green to moderate bluish green	n.d.	n.d.

Figure 10: Gemological characteristics of the emerald samples

Sample modifications

Most of the faces of the rough hexagonal emerald prisms were cut-polished on a Pb-Sn polishing lap to 1-micron grid to obtain a "mirror-like" flat surface. Some samples were sawn in half (//C or ⊥C) with a vertical diamond wire saw. A sample was crushed with a steel mortar/pestle, before picking the interesting fragment under a microscope and set them up on the SEM sticky conductive plate (Fig. 12-left). SEM samples were coated with a 15 μm-carbon layer and the edges of the sample were painted with silver pasta and set in a vacuum for 12-hrs.

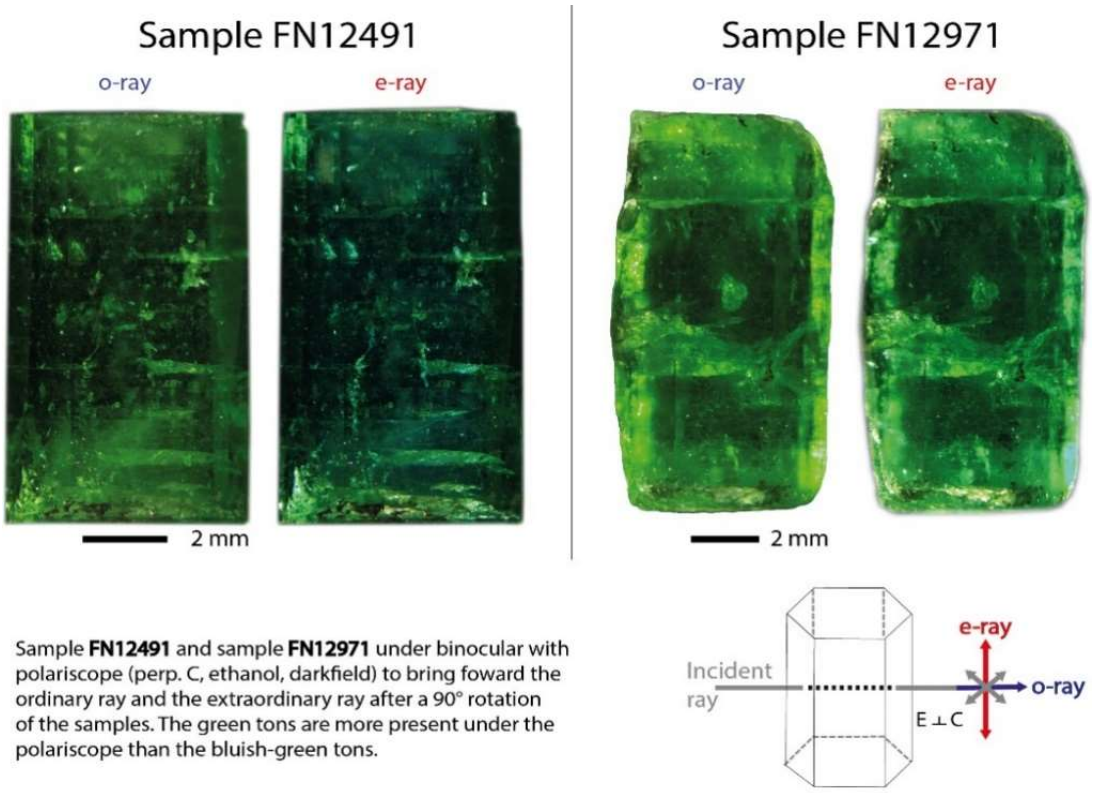

Figure 11: Pleochroism of the emerald samples

For EPMA, the samples were first casted in epoxy resin and polished successively to 1 µm. They were then put for 8 or 12-hrs in an oven and coated with a 15 µm-carbon layer (Fig. 12-center, right). Rock samples were first sieved to keep the finer part of the sample or grinded finely in an agate mortar/pestle, compressed in the sample holder and dried out in an oven for 12-hours. For thin sections, the samples were first cut in half before choosing the desired sample. Each analysis was performed with extreme care, respecting basic lab methodology. Samples were thoroughly cleaned with ethanol and handled with gloves, depending the instrument.

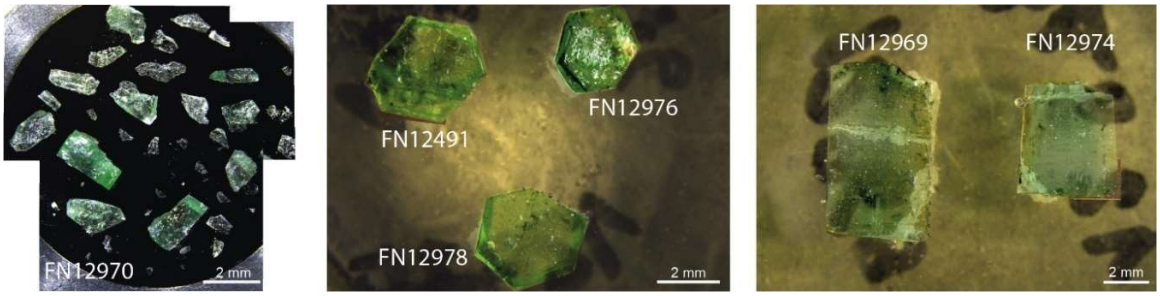

Figure 12: Sample preparation. (Left to right) Crushed samples for SEM analyses; the bigger pieces were verticalized during preparation and silver pasta applied on the side to avoid electron accumulation (air, brightfield). The three samples sliced (⊥C) and casted in epoxy resin for microprobe analyses; note the bubbles and brown polishing diamond powder occurring around the slices despite the care taken (air, brightfield). The two halved (//C) samples for microprobe analysis with a large fracture through FN12969 (air, brightfield).

Description of the inclusions

Microphotography allows to rigorously illustrate the "interior landscape" (Gübelin and Koivula, 1997) of the emerald samples. During the microphotography sessions, the description of the inclusions was done in parallel and helped to safely plan the next analyses. The supplementary pictures are presented in Annex II. Some specific features of the crystals emerged, such as the type/distribution of the inclusions, the type/distribution of the fluid inclusions, the brittle fracturing and the matrix-overplating.

The most common inclusions standing out are the solid mineral inclusions and the minute fluid inclusions; both features strongly affect the clarity. The most noticeable mineral in solid inclusions is dolomite, among carbonates, phyllosilicates, oxides. Dolomite occurs as various-sized inclusions (from < 50 µm to 0,5 mm), as single big crystals, as groups of isolated crystals or as aggregates, forming transparent to translucent *sharp crystallites* (Fig. 13-A, B, C). Some rare dolomite inclusions can be etch-disproportioned, with a granular sugary texture. The second most common mineral group found in the samples is micas, forming clouds of small flat platelets or translucent columnar inclusions (Fig. 13-D). The color saturation and light reflection may vary depending on the composition. In few samples, the color saturation and size of the micas (< 50 µm) make their observation difficult. There is no preferential orientation for the platy sheets or columnar micas crystals. Fluid inclusions occur in the vicinity of mica clouds.

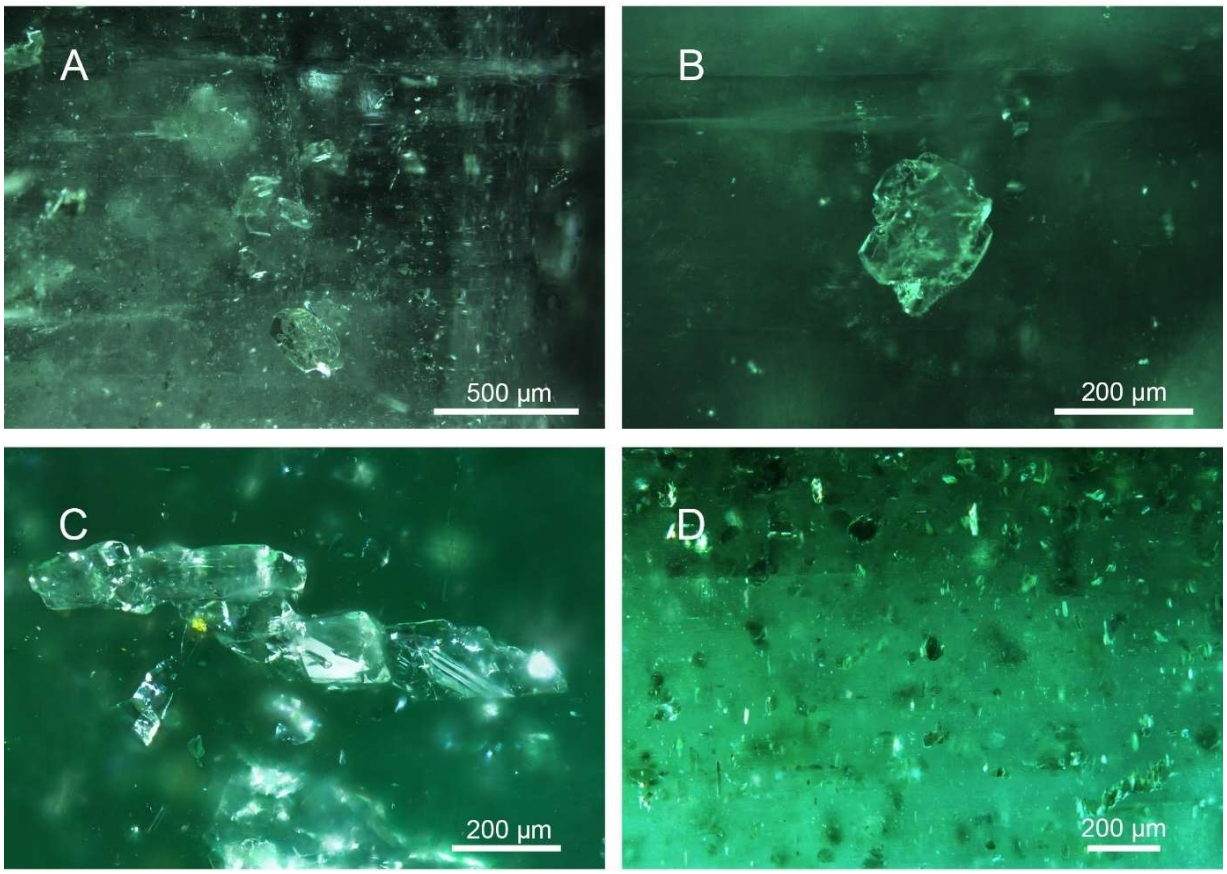

Figure 13: Solid inclusions (mica group and dolomite). ***A*** *Group of «sharp dolomite crystallites» (Gübelin and Koivula, 1997) with few of them formed as perfect rhombohedral. They are occurring within a cloud of minute fluid inclusions and platy columnar micas (FN12491, ethanol, darkfield).* ***B*** *Potential dolomite twinning (FN12491, ethanol, darkfield).* ***C*** *Cluster of sharp dolomite rhombohedra (FN12973, ethanol, darkfield).* ***D*** *Darker cloud of platy columnar phlogopite (FN12970, ethanol, brightfield).*

The next solid mineral phase occurring as solid inclusions is the chlorite group. Chlorite (Fig. 14-A, B, C) occurs as anhedral overplating sheets, as elongated chlorite lamellas on plans //C or as unoriented rounded platy sheets. The color and saturation are relatively constant (dark green) and the size of the chlorite sheets varies between 50 µm and 0,5 mm. The next mineral, found in smaller quantity as inclusion, is rutile (rut). Rutile grains can have two distinct crystalline forms: small euhedral orangy-black grains or yellowish-beige anhedral fine-grained aggregates (Fig. 14-D, E, F). The size of the rutile grains ranges from < 10 µm to 100 µm. Their strong color saturation helps to clearly identify the rutile grains in the emerald matrix. Sulfurs as solid inclusions occur in one sample only and are mainly

pyrite (py) grains and minor chalcopyrite (cpy) (Fig. 15-A, B, C). The grains constitute clusters and are euhedral, with specific color and reflectance. They are found with fluid inclusions and their size varies from 50 µm to 300 µm. They are surrounded by fractures and secondary fluid inclusions.

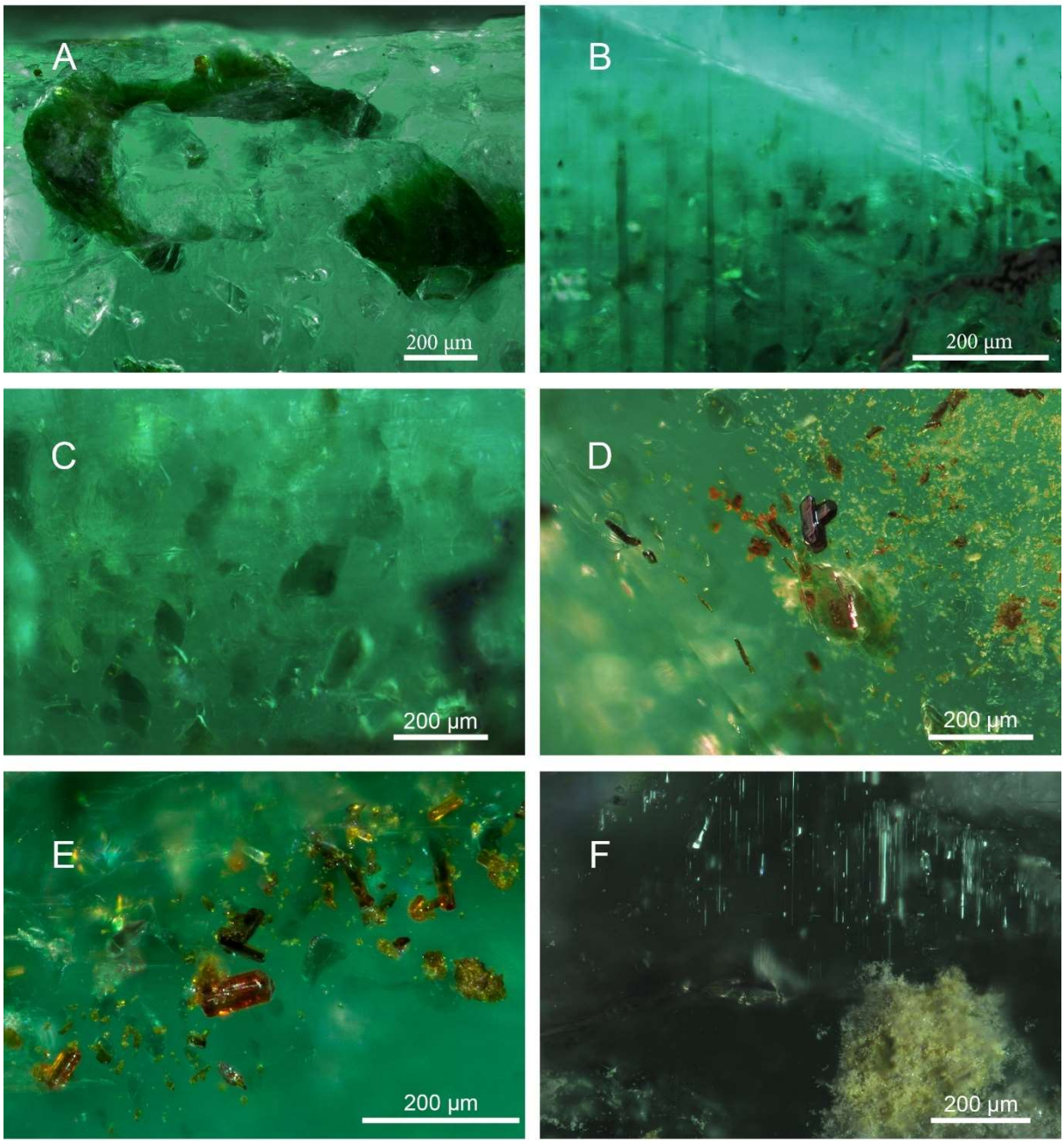

Figure 14: Solid inclusions (chlorite group and rutile). ***A*** *Chlorite on an unpolished prismatic face (FN12980, ethanol, darkfield).* ***B*** *Elongated chlorite lamellas oriented //C (FN12970, ethanol, darkfield).* ***C*** *Same cluster of «rounded and fuzzy Cr-chlorite» (Gübelin and Koivula, 2008), deeper in the sample (FN12970, ethanol, darkfield).* ***D*** *Two mineralogical types of rutile; a mossy yellowish-white aggregate and acicular, orange to black crystals, with common twins (FN12969, ethanol, brightfield).* ***E*** *Acicular twins of rutile close to the crystalline face, note the color shift between the grains due to REE content (GGTL Lab, personal communication) (FN12969, ethanol, brightfield).* ***F*** *Mossy yellowish-white rutile aggregate with rectilinear growth tubes (FN12973, ethanol, darkfield). Some of the darker mossy aggregates found could be iron-tinted magnesite (Gübelin and Koivula, 1997).*

Another opaque mineral is chromite (cr) (Fig. 15-D, E), occurring as sharp hexagonal black flakes dispersed on discrete growth planes or as small randomly distributed thin perorated circles (Cr-films). Their thickness affects the color saturation and changes between both types: light brown for the circles, black for hexagonal flakes. The last opaque mineral (Fig. 15-F), found as inclusion in two samples only, is black patches (10-30 µm) aligned along //C. The description in other articles suggests either chromite or gersdorffite (NiAsS).

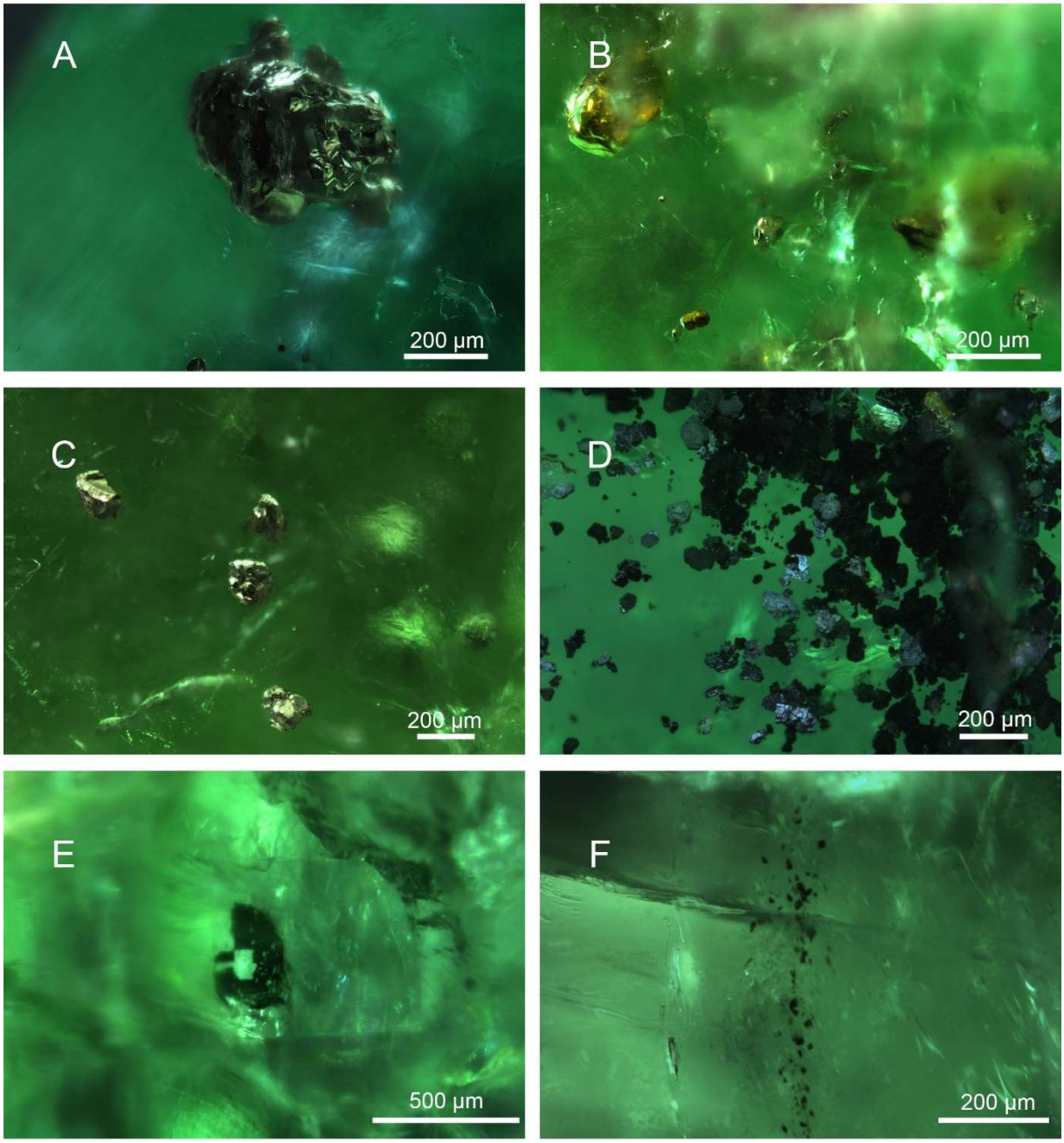

Figure 15: Solid inclusions (oxides and sulfurs). ***A*** *Rounded polyhedral pyrite grain (FN12975, ethanol, darkfield).* ***B*** *Cluster of sulfurs, composed of pyrite and chalcopyrite, based on the reflectance and the color (FN12975, ethanol, darkfield).* ***C*** *Cluster of pyrite grains, with some having a modified dodecahedron shape (FN12975, ethanol, darkfield).* ***D*** *Batch of «sharp chromite» flakes (Gübelin and Koivula, 2008; Kazmi and Snee, 1990) (FN12976, ethanol, darkfield).* ***E*** *Rare small thin perforated circle. Kazmi and Snee (1990) or Gübelin and Koivula (2008) described similar forms as either pyrrhotite or Cr-film (FN12978, ethanol, darkfield).* ***F*** *Patches of unidentified opaque minerals, gersdorffite lookalike, as described in Kazmi and Snee (1990) (FN12984, ethanol, darkfield).*

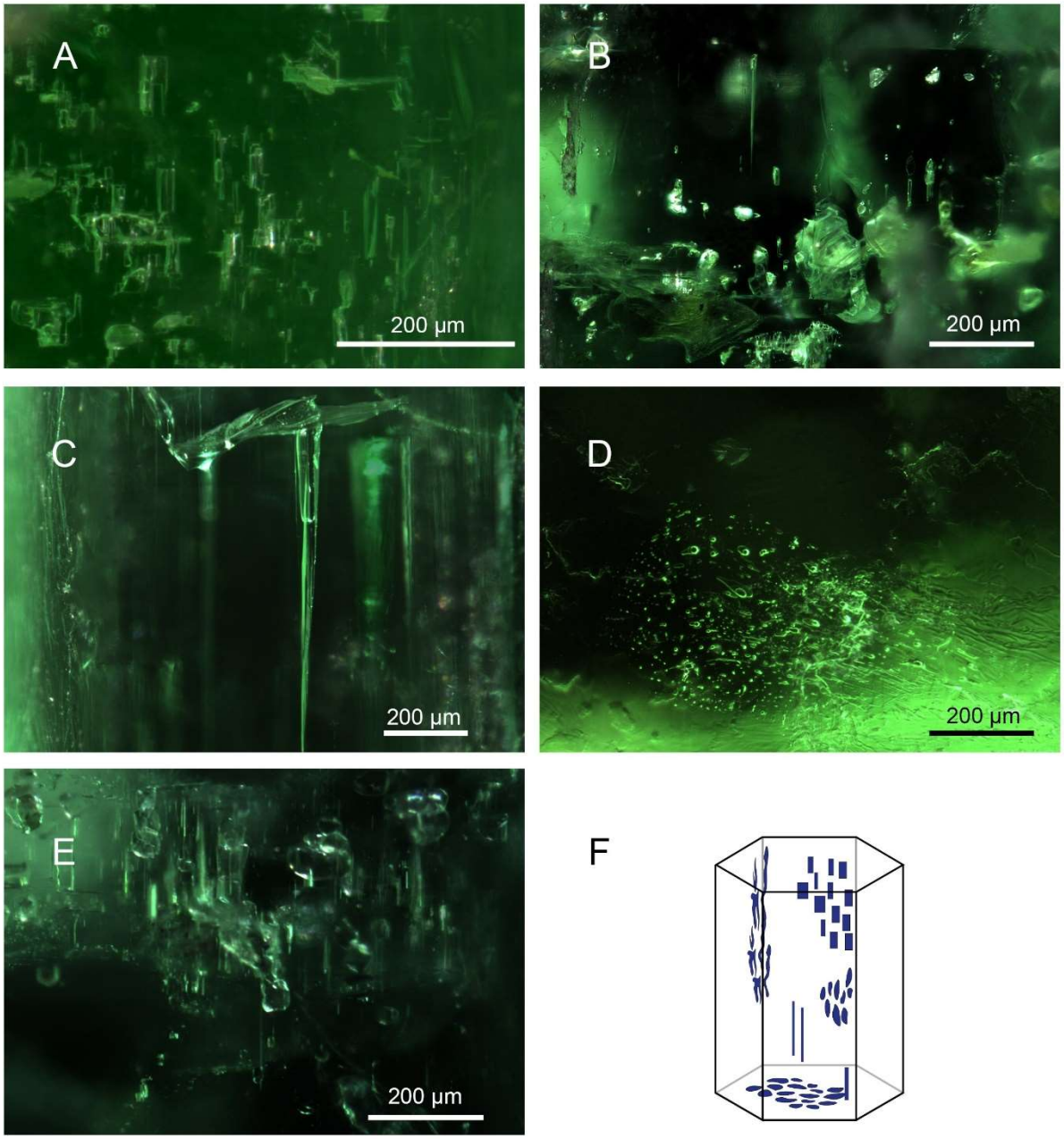

Figure 16 Primary and secondary fluid inclusions. ***A*** *Blocky two-phase fluid inclusions, aligned along the C-axis (FN12976, ethanol, darkfield).* ***B*** *Negative crystals, growth spikes (up) along with «repeated growth-restrictions» (Gübelin and Koivula, 1997) forming comb-like inclusions (bottom) (FN12968, ethanol, darkfield).* ***C*** *Bigger biphase growth spike inclusion (FN12968, ethanol, darkfield).* ***D*** *Secondary monophase and two-phase inclusions, the result of a healed fissure (FN12490, ethanol, darkfield).* ***E*** *Batch of small xenomorph transparent crystals coupled with growth tubes and curved alignment of secondary inclusions (bottom) (FN12968, ethanol, darkfield).* ***F*** *Sketch illustrating the different primary and secondary inclusions found in Mingora emeralds.*

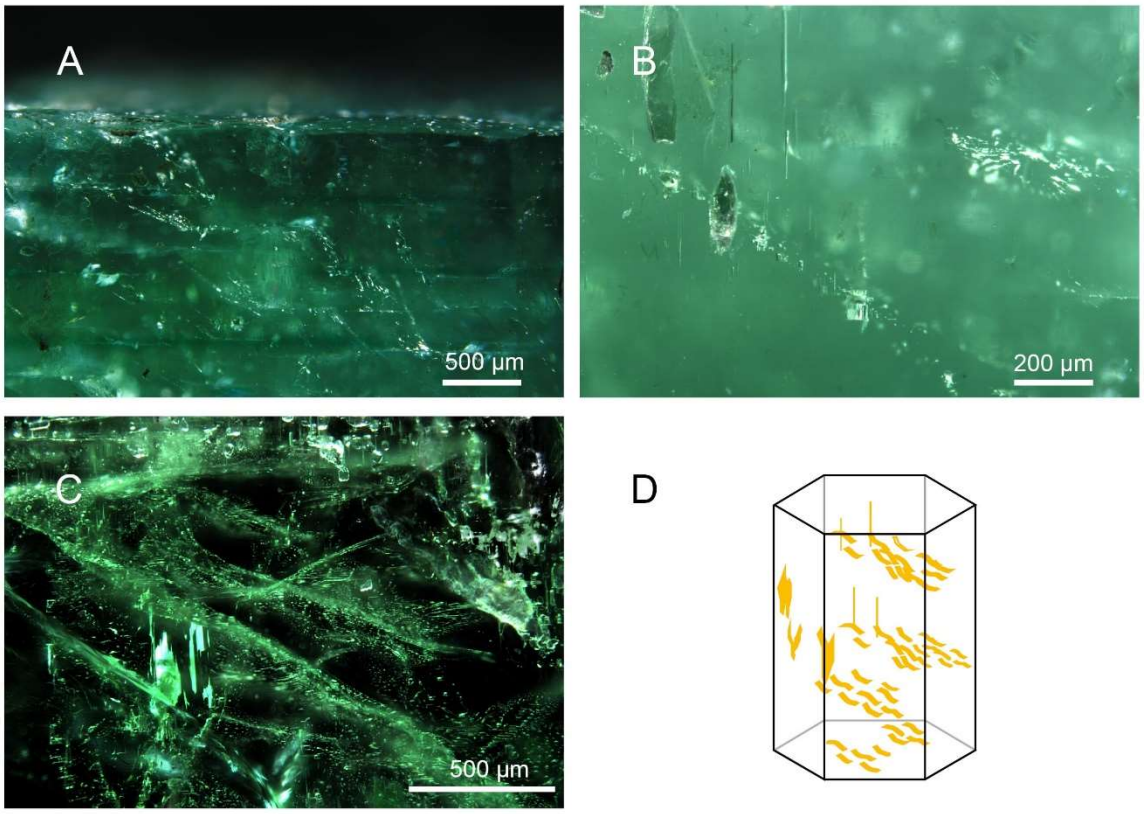

*Figure 17: Primary, secondary and pseudosecondary fluid inclusions. **A** Pseudosecondary fluid inclusions arranged on parallel planes and secondary on the cleavage planes (FN12970, ethanol, darkfield). **B** Growth tubes, elongated chlorite sheets, «curved arrangement spreading on basal cleavage» (Gübelin and Koivula, 1997) of secondary fluids inclusions (right) (FN12974, ethanol, brightfield). **C** Jagged fluid plane (left), zigzag line (bottom left), secondary diagonal inclusions, smaller growth tubes, primary inclusions and a batch of small xenomorph transparent crystals (FN12969, ethanol, darkfield). **D** Sketch illustrating the inclusions sets found in Mingora emeralds.*

The next important feature of the Mingora emeralds is the diversity of the fluid inclusions. The first category are the primary fluid inclusions, which are small and hardly discernible. Most of them are minute mono-biphase, forming clouds in the inner zones of the samples. But the primary fluid inclusions also comprise biphase growth spikes, growth tubes, blocky biphase, negative crystals, repeated growth-restrictions and clouds of minute biphase fluid inclusions (Fig. 16-A, B, C, E). The primary fluid inclusions are often located on a specific growth sector (often ⊥C) in the crystal and their size varies around 30-40 µm depending on the considered type. Pictures are hard to obtain, because cloudy minute fluid inclusions area are present all around those growth sectors. Secondary and pseudosecondary fluid inclusions are more obvious to detect. They include ⊥C healed fractures (Fig. 16-D) and recurrent parallel diagonal pseudosecondary-secondary fluid inclusion planes (Fig. 17-A, B, C). These fluid inclusions are mono- or biphase, and a lot more present as the primary fluid inclusions. Their size is the same.

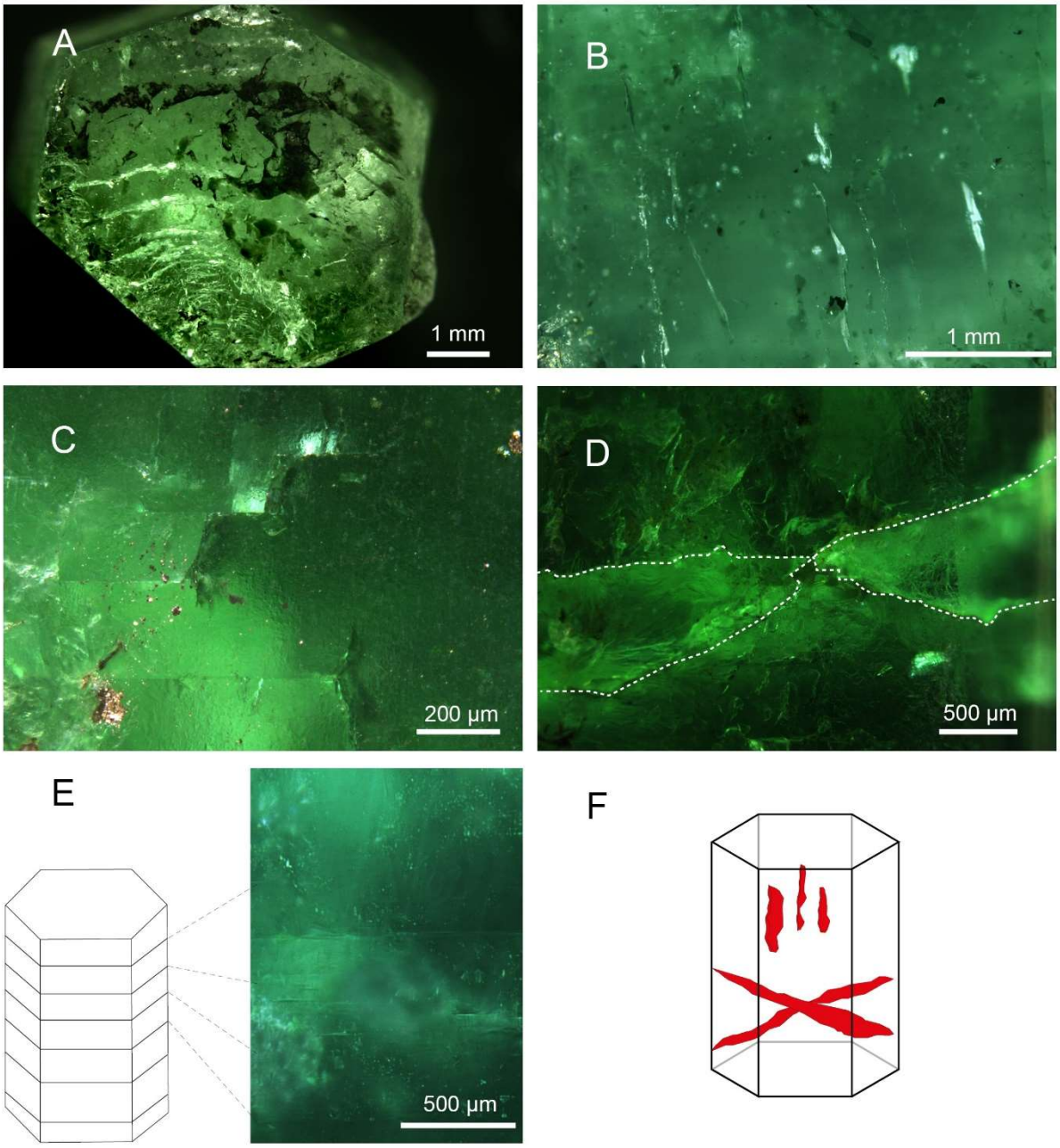

*Figure 18: Fractures. **A** Basal concentric fractures with no related solid inclusions inside (FN12974, ethanol, darkfield). **B** Wavy fractures parallel to the C-axis with no related solid inclusions inside (FN12974, ethanol, darkfield). **C** Diagonal fractures shifted by the cleavage plane and its «flat parallel fissures» (Kazmi and Snee, 1990) (FN12975, ethanol, darkfield). **D** Set of conjugated shear fractures crossing the prismatic faces (FN12971, ethanol, darkfield). **E** Cleavage planes, not discernible in every samples (FN12941, ethanol, darkfield). **F** Sketch illustrating the fractures found in the Mingora emeralds.*

Another striking feature seen in some samples is the brittle fracturation and the visible cleavage planes (Fig. 18-E). The fractures are different from the (pseudo-) secondary fluid inclusion planes because they have not been healed and show no related fluid inclusions. The fractures are conchoidal, run often across the whole sample, and can be along //C, between/on the cleavage planes or as conjugate shear fractures due to compression (Fig. 18-C, D), or as rare basal concentric fractures (Fig. 18-A). These types of fractures could underlie late deformation stages after the crystallization. Another important feature is the chemical and mineralogical distribution, named as “zonation”. Some of the crystals have a strong clarity contrast depending on the considered area (Fig. 19-A to F), with preferential chlorite-quartz-dolomite association in the cleanest zones, and micas-fluid inclusions in the fuzzy zones. The color

distribution in the stones also follows this mineralogical distribution, with a stronger color saturation on the rims of the hexagonal faces (Fig. 19-F as best example). The last noticeable feature in the samples is the introduction timing of the different inclusions. Rutile near the rim or on the brittle fractures (Fig. 20-A, B, C), or chlorite always situated as overplating or inside the external rims (Fig. 14-A, Fig. 20-E) suggest preferential inclusion growth. For chromite the sporadic distribution of the flakes are all along the growth (Fig. 20-G, H).

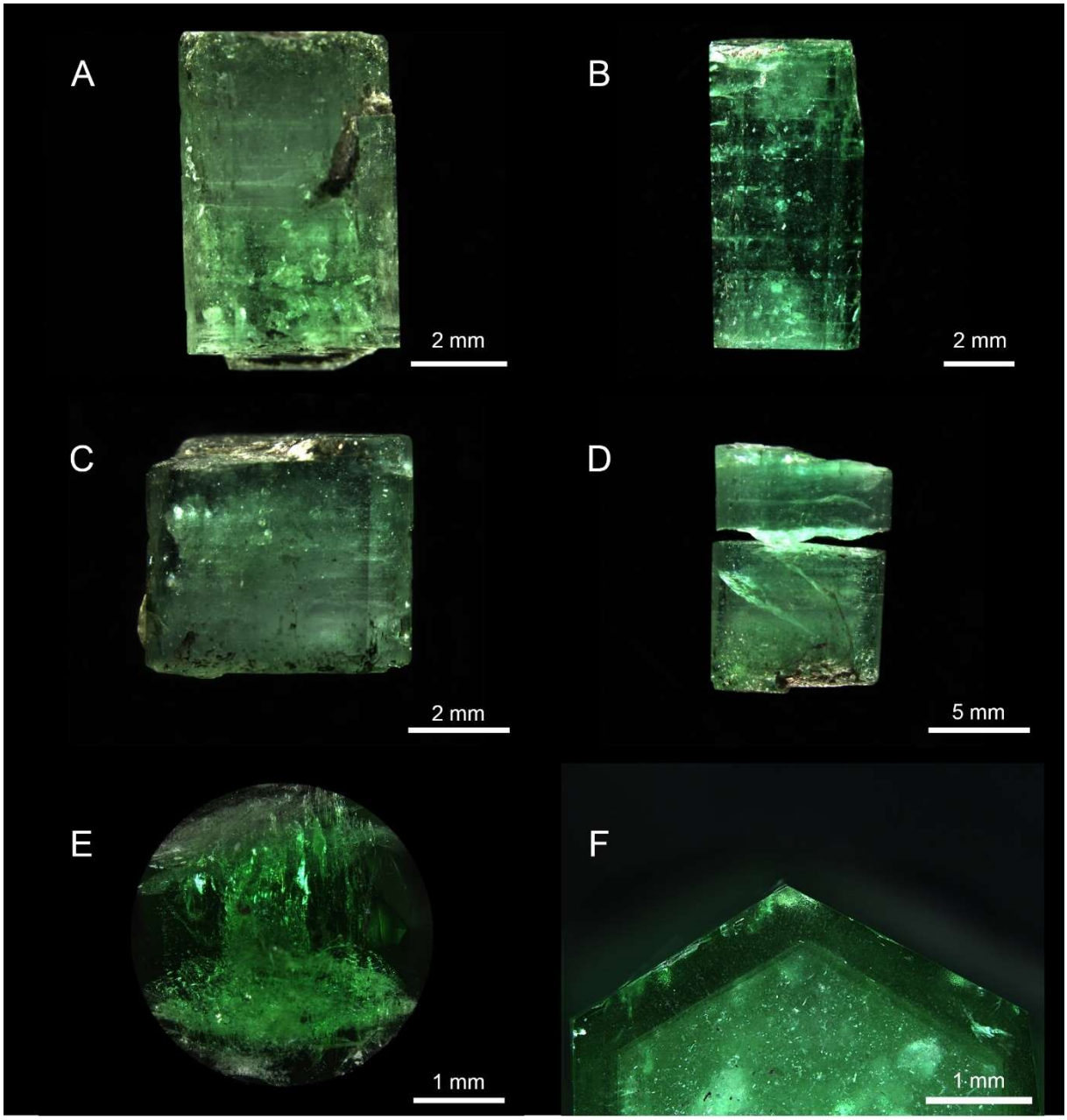

*Figure 19: Zonation **A** Two growth sectors; a pinacoidal fuzzy growth sector with micas and fluid inclusions (top and core), and a more translucent hexagonal prismatic sector with qtz-dol (bottom), talc overplating (FN12969, ethanol, darkfield). **B** Two well-defined fuzzy pinacoidal growth sectors with micas (top and bottom) and a transparent hexagonal prismatic growth zone in the middle of the crystal (FN12491, ethanol, darkfield). **C** A more translucent and saturated sector overgrowing on the bottom fuzzy core (FN12974, ethanol, darkfield). **D** Sample with a fuzzy sector (bottom) and a fractured translucent top, broken at the limit during preparation (FN12970, ethanol, darkfield). **E** Small brilliant-cut emerald displaying an uneven color distribution (from culet, FN12984, ethanol, darkfield). **F** Sharp color and mineralogical distribution, ⊥C view (FN12491, ethanol, darkfield).*

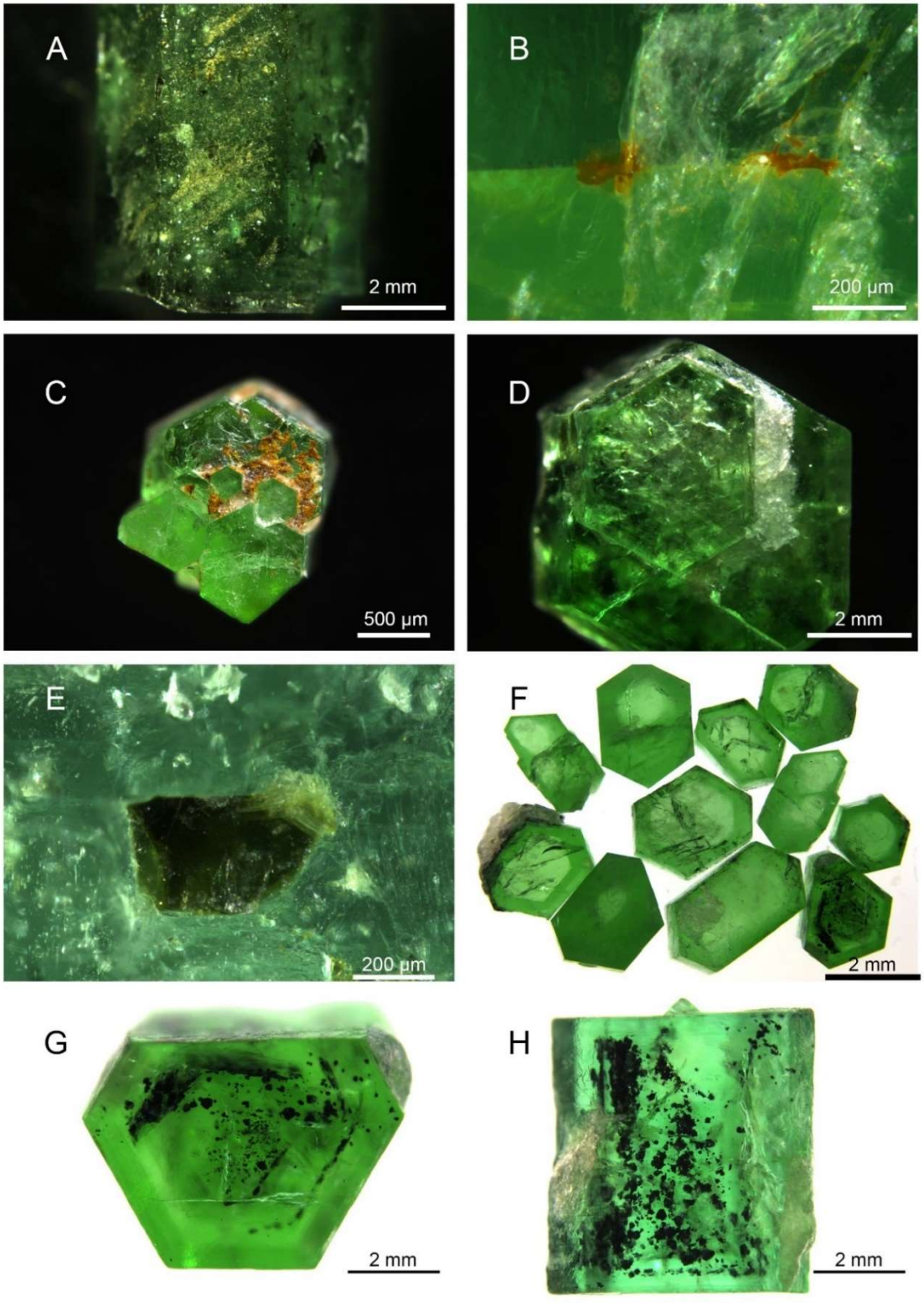

Figure 20: Introduction timing. ***A*** *Yellow rutile aggregates on a prismatic face spreading as diagonal trails, following the same angle as some of the fluid inclusions (FN12969, ethanol, darkfield).* ***B*** *Orange rutile aggregates formed at the interface of a cleavage plane (FN12972, ethanol, darkfield).* ***C*** *Pinacoidal faces of an emerald cluster, sprinkled with orange rutile aggregates and talc-magnesite (FN13156, ethanol, darkfield).* ***D*** *Microcrystalline magnesite on the pinacoidal face (FN12978, ethanol, darkfield).* ***E*** *Outcropping of dark green platy chlorite on an unpolished prismatic face (FN12977, ethanol, darkfield).* ***F*** *Smaller crystals displaying lighter colors in the core than on the rims. Note the residual talc-magnesite host rock left on some crystals (FN13155, ethanol, brightfield).* ***G-H*** *(pinacoid face-prismatic face) A piece of the previous lot illustrating the color disparities and chromite flakes in specific zones (FN13155, ethanol, brightfield).*

Analytical results

UV-Vis-NIR Spectrometry

On Fig. 21, 5 representative spectra are shown, with the spectra for the other samples to be found in Annex V. Few spectra are missing because of analytical limits (size, form, saturation) or bad timing of the sample preparation (crushing). The main absorptions are at 433, 610 nm (o-ray), and 419, 640, 680.5 nm (e-ray) and weaker absorptions at 476, 638.5, a doublet 680.5-684 (o-ray). There is a common flat 840-850 nm-bump and a 372 nm-dent and a small at 960 nm.

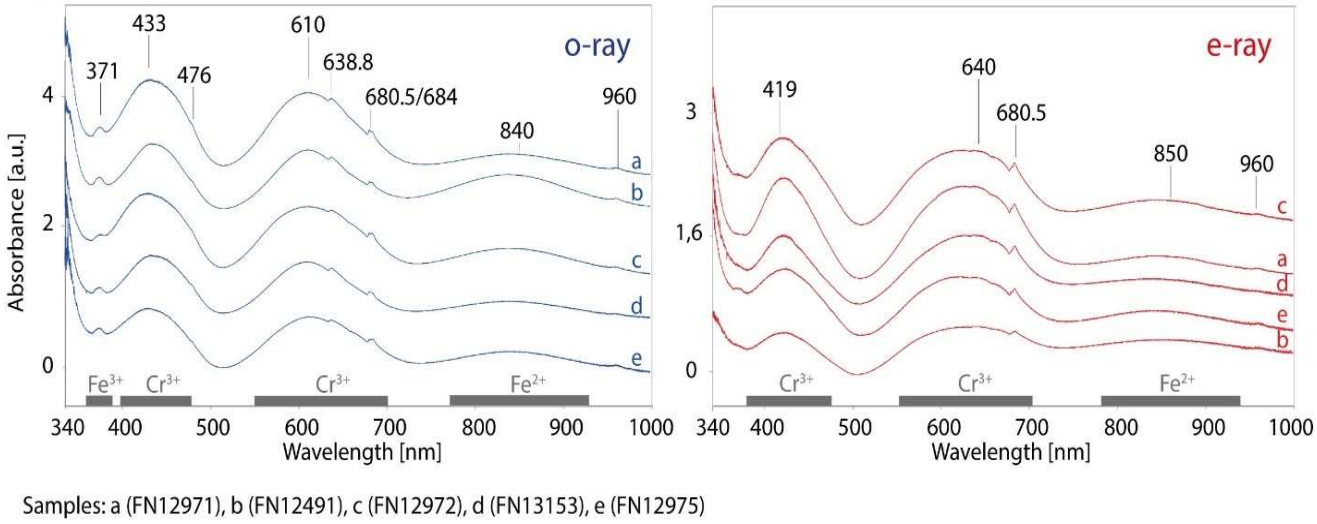

Figure 21: UV-Vis-NIR spectra of 5 samples, revealing the optical features of Mingora emeralds. The axes are set according to Smith (2009).

Raman

FT-Raman Spectroscopy

The FT-Raman results show the majors peaks of the FN12491 sample in two directions. The major peaks at 193.6, 401.6, 670-690 and 1071 also regularly appear during the Raman Microspectrometry and allow to determine which mineral provides the confocal signal, let aside the matrix effect. Regarding the strong fluorescence visible on the ray //C, a wavelength change of the laser, a filter, a shorter acquisition time, or smaller analytical volume (not the whole crystal like in this case) could have enhanced the quality of the spectrum.

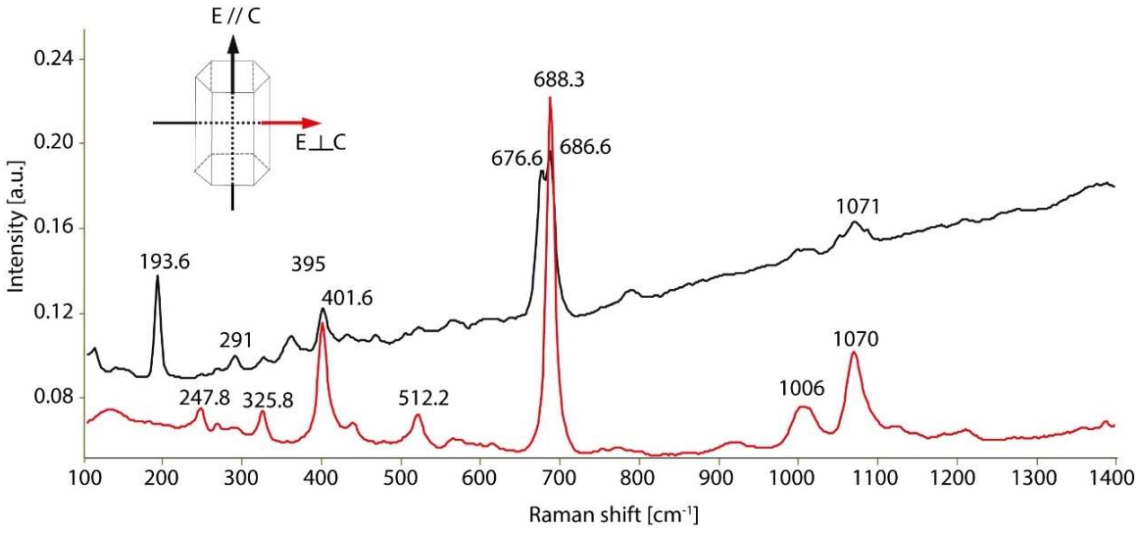

Figure 22: Absorbance Raman spectrum for the FN12491 sample

Laser Raman Microspectrometry

The results of the Raman Microspectrometry unveil numerous inclusions in the Mingora emeralds. These vibration spectroscopy analyses were organized before the SEM-microprobe sessions and helped to identify special inclusions; they were less difficult to recognize thereafter, based on their chemical composition. Numerous spectra were rejected because of the strong matrix effect of the emerald (as described on Fig. 22) and because of many inclusions producing a weak Raman signal. The location and the flatness of the outcropping inclusions lead to strong variations in the Raman signal. The minerals producing the weakest signal were part of the phyllosilicate family, mainly the talc inclusions and some chlorites. The fluorescence of the matrix, their weak intensity and their thickness produce phyllosilicates spectra with visible machine artifacts and a lot of spectral noise. Some exceptions within the phyllosilicates, like phlogopite, give more information about the nature of the mineral. The spectra for sulfurs/oxides are too close between each species to allow determination (like pyrite-pyrrhotite); SEM analyses put in evidence their lack of reliability. For dolomite, quartz, magnesite or rutile inclusions the signal is quickly acquired, and the S/N ratio is satisfying. The quick non-destructive acquisition saves time and keeps the geometry of the inclusions and the sample intact (aside from the polishing preparation for better spectra). The spectra of the inclusions are in Annex VII and VIII.

EDX

ED-XRF

XRF analyses were completed on all emerald samples (except on the crushed ones). The samples sawn in half allow to determine their internal composition and expose the heterogeneity of the Mingora emeralds. The major bias in these analyses is the large 2 mm-X-Ray spot encompassing also the composition of the overplating/outcropping inclusions. Fig. 23 exposes the representative data, the remaining data can be found in Annex XIV.

Sample	FN12491		FN12969		FN12974		FN12975		FN13153	
Site	prism	pinacoid	prism	core	prism	core	prism	pinacoid	prism	pinacoid
SiO_2	64,36	65,16	63,21	64,62	64,63	65,52	63,87	66,76	64,30	64,90
Al_2O_3	13,22	12,76	13,52	14,60	14,88	13,71	15,74	12,29	11,15	12,70
Fe_2O_3	2,43	2,24	1,91	1,93	1,70	2,17	1,78	1,29	2,97	2,36
MgO	3,52	3,88	2,84	2,95	2,83	2,78	2,89	3,69	3,68	3,29
CaO	0,06	0,38	3,05	0,55	0,05	0,40	0,37	0,02	0,05	0,18
Na_2O	1,08	0,64	1,18	1,03	1,73	1,19	1,01	0,96	1,47	1,21
MnO	0,04	0,03	0,02	0,02	0,01	0,01	0,01	0,02	0,04	0,04
Cr_2O_3	1,35	1,13	0,48	0,44	0,38	0,20	0,27	1,13	2,43	1,34
V_2O_5	0,14	0,07	0,15	0,14	0,13	0,17	0,17	0,13	0,08	0,06
Sc_2O_3	0,20	0,20	0,06	0,14	0,14	0,31	0,35	0,16	0,28	0,40
Rb_2O	0,00	0,00	0,00	0,00	0,00	0,00	0,00	0,00	0,00	0,00
Cs_2O	0,12	0,02	0,08	0,08	0,04	0,05	0,04	0,04	0,04	0,01
BeO (fixed)	13,50	13,50	13,50	13,50	13,50	13,50	13,50	13,50	13,50	13,50
Total	100,00	100,00	100,00	100,00	100,00	100,00	100,00	100,00	100,00	100,00

Figure 23: ED-XRF analyses of 5 samples, on hexagonal prismatic faces or on core/pinacoidal faces

EDX-SEM

EDX-SEM results for the emerald samples are the crucial data for the present study. After meticulous microscope observations, sessions of Laser Raman Microspectrometry to identify a first batch of inclusions, SEM provides a stock of 76 reliable semi-qualitative chemical analyses (Annex XII, XIII) and a closer look into the habit of the inclusions (Annex XV). Cross-checking between each method and statistics performed on the chemical analyses contribute to complete the inclusions landscape. The exact location of the analyses on each sample is missing. Among the results, recurrent inclusions are clinochlore (chlorite group) and the micas series with phlogopite, muscovite, biotite, phengite. The compositions of clinochlore inclusions are similar and micas seem to be part of a continuous series (Deer

et al., 2013). The other main inclusions are talc, dolomite(-siderite) and quartz; rarer inclusions include the pyroxene-amphibole series, an undefined series between talc-clinochlore, ferrichromite ($Fe^{2+}(Cr^{3+}, Fe^{3+})_2O_4$), rutile and zircon (-xenotime or apatite).

The sulfurs show also some interesting details, such as the single of chalcopyrite-pyrite-goethite (gt). An empty fluid inclusion with a cube of halite left is also present. The inclusions easily spotted by Raman Microspectrometry because of their size (dolomite, rutile, quartz) only account for a smaller part in the SEM data. Minor/trace elements are sometimes present in the inclusions, like Ti-biotite, Ni-talc or Ni-phlogopite or Ni-clinochlore, Mn-diopside, Zn-V-ferrichromite, Sc-halite, but the most usual is Cr. As displayed (Annex XX), Cr is preferentially found in chromite flakes, but the Cr-content is not higher in the mica group than in the chlorite group.

The three single-point analyses in the emerald matrix give another indication about the general chemical composition. They are semi-quantitative because of the SEM's detection limit for light elements and the recalculation of the values by the SEM software. Potential sources of inaccuracy are the orientation of the small phyllosilicates, possibly deviating the electron beam, contamination during the crushing, contamination of the SEM chamber by previous users or the loss of multiphase fluid inclusions during the trip to Lausanne University.

For the rock sample analyses by EDX-SEM, they complete the XRD results and the observations of the thin-sections. The chemical compositions of the three rock sample, extracted from two fault zones, shows platy minerals with a Mg-Si-O composition, with a large range of Mg/Si ratios (Annex XVII).

EMPA

EMPA analyses complete the big picture outset by the SEM analyses. For the 35 spot analyses, most of the tested inclusions are clinochlore, followed by micas, quartz, talc and continuous series (mica-talc) also detected at SEM. The locations of the spot analyses are relative (due to the missing locations) and classed by zone (core, half-way, rim), as displayed in Annex XXII-1. As observed during microscopic description and SEM analysis, the statistics on the few spots show a greater distribution of muscovite, the undefined platy inclusion and quartz in the core, with more clinochlore and biotite on the rim of the samples. In Annex XXII-2,3, the data of all clinochlore inclusions by microprobe are combined to underline potential variations of clinochlore composition between core and rim. The variations in major elements are small but recurrent. Mn-depletion in certain clinochlore inclusions can be spotted in the rim and there is more Ti in inclusions in the rims. The number of spot analyses does not allow to perform any reliable statistical analysis.

For the chemical maps, the five chosen elements on both samples outline the growth zonation and the enrichment/depletion, which is more or less highlighted depending on the sample. On the matrix side for FN12974, the most important characteristic is the Fe-depletion and the Cr-enrichment on the external rim. Strangely, the spot with the highest concentration is on top of a prismatic face. Mg-Na-Al do not show sharp variations, but two growth zones are discernible, with a light Al-enrichment, and a Mg-Na depletion from core to rim. On the side of the inclusions, the most Al-concentrated inclusions are the platy muscovite-phengite in the core (cf. SEM, microprobe spot analyses), followed closely by clinochlore in the core and in the rim. Mg-concentrated inclusions could be talc or clinochlore; Na-concentrated inclusions may be small portions of talc. The Fe-concentration on some inclusions matches with Al values and should be related to clinochlore. Finally, the Cr-concentration could be related to micas (cf. SEM). In the FN12491 sample, the matrix reveals more interesting features: Al decreases from core towards the rim, Mg-Na increase slightly towards the rim and the Fe-Cr increase is very pronounced. The Fe concentration acts in the opposite way as in FN12974 and Cr better displays the various irregular growth zones. Inclusions in FN12491 follow the same pattern as FN12974, with a small spot of Na-enriched talc and large elongated Mg-Fe-rich clinochlore parallel to growth striae (as described with the microscope). Note the relative impoverishment of Cr-clinochlore compared to the Cr-rich matrix. Potential sources of error for the analyses are the approximate flatness of the sample,

contamination by the polishing laps and by the diamond wire. The few microprobe results of identified minerals are close in composition to that of the SEM and thus testify reliable results for both methods. A misunderstanding occurred during the settings for spot analyses and Mn was analyzed instead of Cr. Moreover, the general picture for the distribution of the spot analyses on the samples was lost; only remains the description of the points (rim, half-way, core). Further analyses focused on the growth zones of the emerald samples were cancelled.

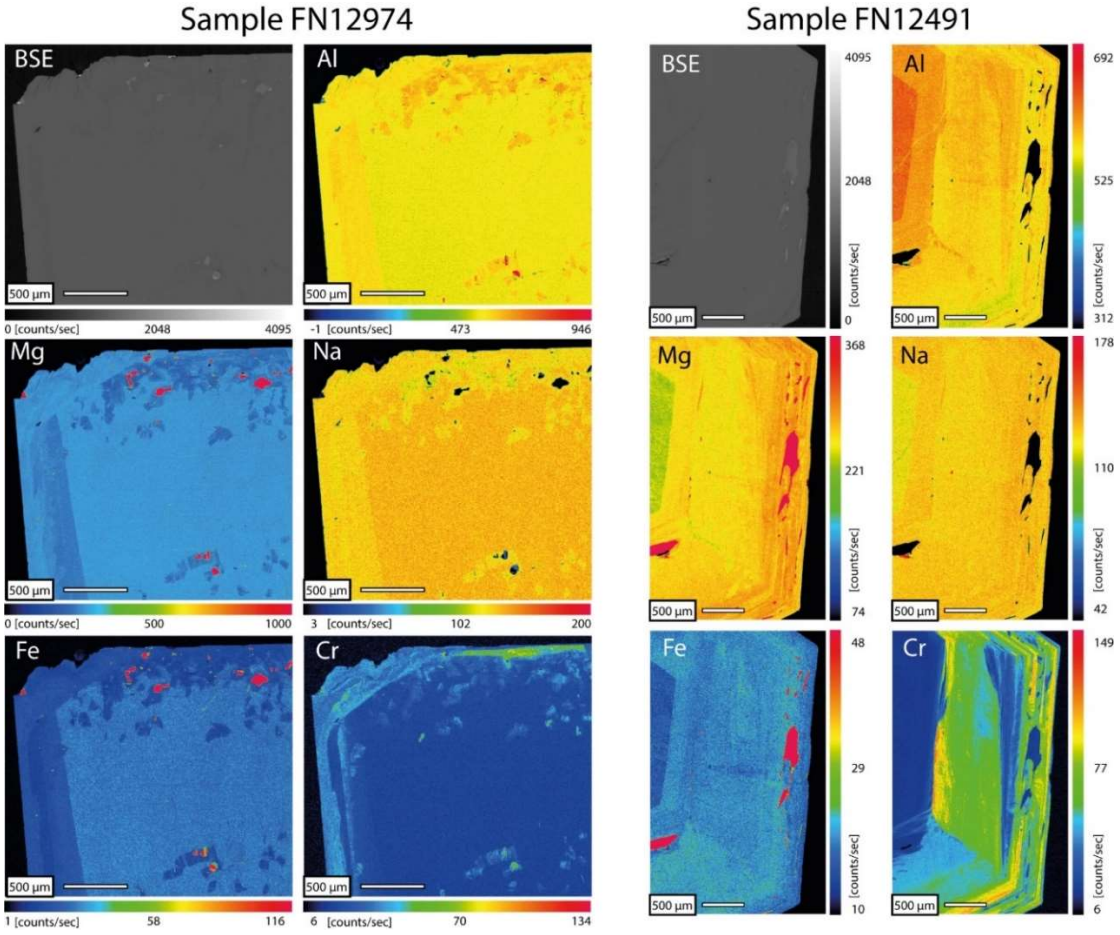

Figure 24: Microprobe chemical maps of FN12974 and FN12491 samples

XRD

The analysis (Annex X) on the emerald sample (FN 12970) was a test to detect another pattern of other phyllosilicates. Unfortunately, due to the low concentration in phyllosilicates only negligible pattern of chlorite appears. Whole-rock analyses (Annex XI) on the three powders obtained from the two different tunnels, the similarities in the patterns indicate an assemblage of multiple phases of altered talc-pyroxene group minerals.

Thin sections

Thin sections give other important insights into the source of the inclusions and their genesis. Some supplementary pictures can be found in Annex IX. As described earlier, emerald occurs disseminated in the tlc-mag-dol schist or associated with micas-qtz-carbonate veins. The recurrent inclusions observed are also present in the matrix or in the veinlets: omnipresent tlc-mag matrix with dol grains (Fig. 25-A), with intruding qtz-muscovite (ms) veinlets (Fig. 25-D). This allows to explain part of the inclusions. The disseminated chromite grains in the matrix or in the emeralds (Fig. 25-F), the micas pinpoints inclusions (Fig. 25-E), the cleavage fractures (Fig. 25-G) in the emeralds grains all show similarities.

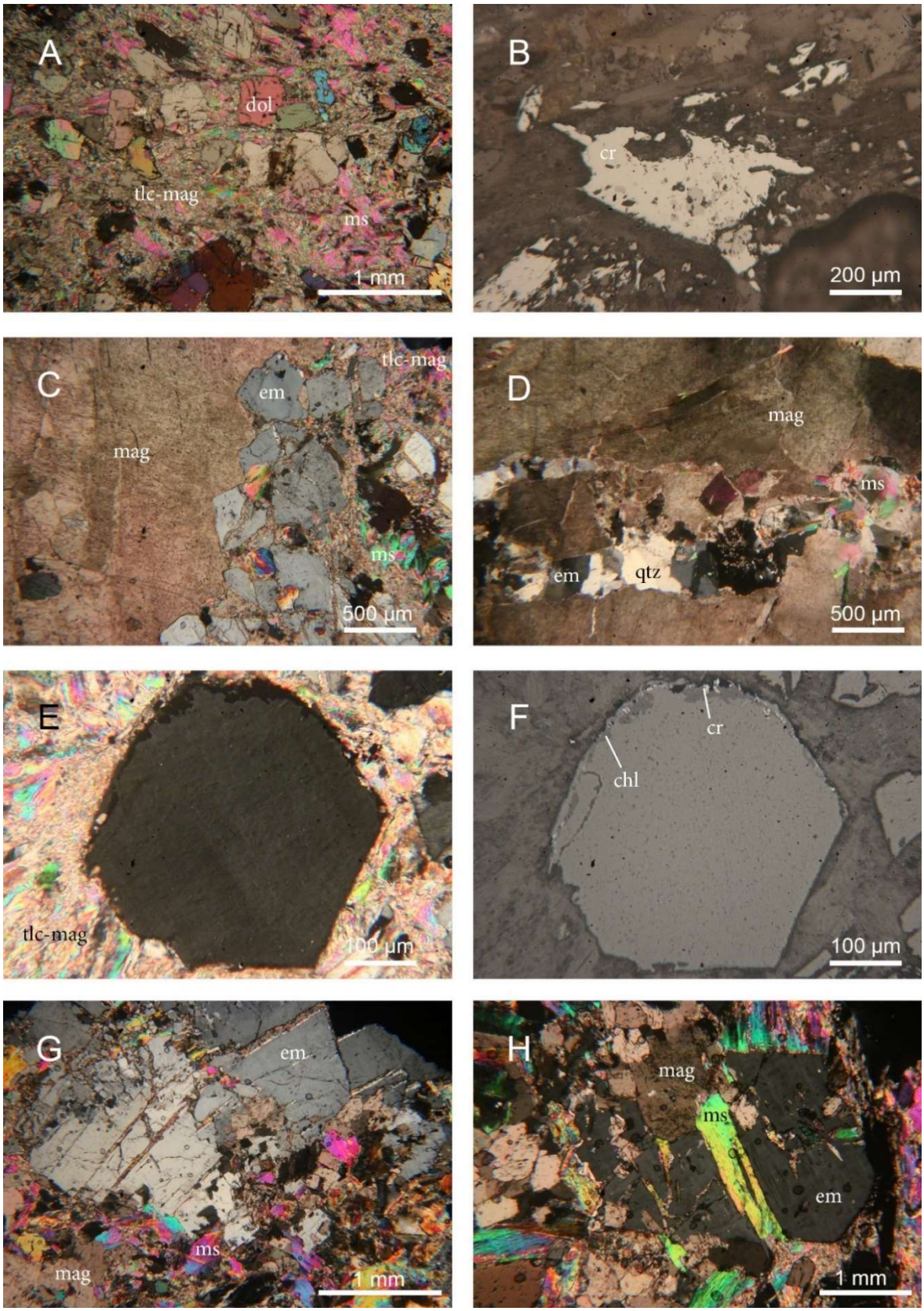

Figure 25: Thin sections. ***A*** *An unmineralized section of host rock; microboudin or isolated dolomite grains occurring along schistosity planes in a fine interbedded magnesite-talc-muscovite matrix (LC-khalid-5, XPL).* ***B*** *A chromite grain inside the magnesite-talc matrix; note the salmon-grey opaque inclusion mineral, which could be pyrrhotite (LC-khalid-6, RL).* ***C*** *Emerald mineralization (dark gray first-order) found in a fine magnesite-talc-muscovite matrix, at the interface with large grained magnesite (LC-khalid-8, XPL).* ***D*** *Emerald-quartz-muscovite veinlet cross-cutting large-grained magnesite (LC-khalid-8, XPL).* ***E*** *Basal section of emerald in a fine magnesite-talc matrix. Some pinpoint mica inclusions in the emerald are visible*

*(LC-khalid-8, XPL). **F** The same basal section with chromite grains and chlorite bands on the rim of the crystal (LC-khalid-8, RL). **G** Fractured emeralds along cleavage planes pervaded by fine magnesite, within a magnesite-talc-muscovite-dolomite matrix (LC-khalid-9, XPL). **H** Emerald crystal replaced by muscovite-magnesite (LC-khalid-9, XPL).*

Discussion

Host rock characterization

The observation of the thin sections brings hints about the genesis of the Mingora emeralds and helps to better understand the presence of several inclusions. The tlc-mag matrix and em-qtz-ms veinlets are omnipresent and the mineralogical assemblage can also be spotted inside the emeralds. Small details like the zonation in some chromite grains (Fig. 25-B) may support variations in the growth environment (fO_2, temperatures) during the genesis of the deposit (Arif, 2000). The assemblage of the sulfur grains inside the emeralds may also comfort this hypothesis. The results of XRD/SEM analyses give an idea of the protolith rock before the circulation of hydrothermal fluids inside the fault system, with a resulting rock which is a mix of pyroxenes ($MgSiO_3$) and talc ($Mg_4Si_3O_{12}$) with variable Mg/Si ratio.

Emerald identification and chemical variations

Based on the observations and analyses in the *Results* chapter, the emerald samples used for the study can be classified as emeralds (Schwarz and Schmetzer, 2002). The UV-Vis-Nir analyses match with the spectrum of beryl (Lafuente et al., 2015) and the absorptions for the ordinary (o-ray) and extraordinary (e-ray) rays give indications about the origin of the color. The transmission range for the samples are in the green (512 nm for o-ray) and in bluish-green (500 nm for e-ray). On Fig. 21, the main absorptions (433, 610, 419, 640, 680.5 nm) and weaker absorptions (476, 638.5, 680.5, and the doublet 680.5-684) are associated with the dispersed Cr^{3+} in octahedral coordination (Wood and Nassau, 1968). The flat 840-850 nm-bump is related to Fe^{2+} ions inside the octahedral Al^{3+} sites (Schwarz and Henn, 1992; Vapnik et al., 2006). The 372 nm-dent highlights the presence of Fe^{3+} in Si^{4+} sites (Schmetzer et al., 1984; Vapnik et al., 2006) and the bump at 960 nm is potentially water (GGTL, personal communication). The spectral class which matches the best for the Mingora samples is Class III (based on Fig. 2), with Cr^{3+} only and both oxidation states of iron. Smith (2009) classified the Swat emeralds as Class II/III.

The Raman signal for the representative sample shows the major peaks (Fig. 22) for natural non-treated emeralds situated between 100 and 1100 cm^{-1} (Lewis, 2001). The peaks are at 193.6 cm^{-1} (ring rotation), 247.8 cm^{-1} (ring rotation), 291 cm^{-1} (n.d., also in the Brazilian emeralds of Santa Terezinha), 325.8 and 395 cm^{-1} (deformation mode of the ring), 394-400 cm^{-1} (ring vibrations), 512.2 cm^{-1} (ring vibrations), 688.3 cm^{-1} (Be-O bond stretching, ring vibrations), 676.8-688 cm^{-1} (Be-O bond stretching), 1002.5-1007 cm^{-1} (Si-O bond stretching), 1067.5-1072.5 cm^{-1} (SiO or Be-O bond stretching). The additional bands present variabilities in their true shape and other peaks may be dependent on the origin of the sample (Bersani et al., 2014; Le Thi Thu, 2008; Moroz et al., 2000; Reshma et al., 2017).

The observation of inclusions unveils their specific internal features, highlighting their diversity, but also giving some identification keys. Concerning the determination of the origin of the samples, the quantity of samples is not sufficient to provide statistically recurrent features. The internal paragenetic assemblage of FN12976 (ferrichromite-py-cpy) is not similar to FN12970 (dol-chl) and shows the heterogeneity of the Mingora deposit. This raises also questions about the heterogeneity of the other deposits of Swat Valley (Shangla, Gujar Kili,…), due to the regional chemical variations in the lithologues (Arif et al., 2011).

XRF/SEM analyses on emerald matrices confirm the strong chemical zoning and its relationship with the color, exactly as the EMPA chemical maps predicted (Fig. 24). Small changes in major/minor elements influence the color saturation, such as the moderate bluish green of FN12974 and the vivid slightly bluish green of FN12491. On XRF analyses, Cr shows a large disparity depending on the

sample. Mg-Na compositions also show strange disparities (they should be more or less equal, based on Fig. 4, or on SEM data in Annex XV).

Moreover, the emerald sourcing for the study was not performed in-situ and the risk of mixing with other productive sources or the risk of treatment exist (see IR in Annex VI). Some of the described inclusions, the color zoning (chemical zoning) can also be found in other geological contexts (Schwarz, 1994; Zwaan et al., 2005), so other methods of characterization are needed as FTIR or PL.

Paragenetic diagram

Microscopic observations coupled with the different chemical analyses provide information to draw the growth history in a compiled paragenetic diagram (Fig. 26), this diagram represents the different phases of deformation endured and healed by the matrix, and the later deformation phases with brittle fracturing. For the fluid inclusions and fractures, the general primary fluid inclusions surround mica and dolomite crystals or are present in growth restriction zones inside the cores. The pseudosecondary and secondary fluid inclusions are located along the healed fissure planes. Late fractures can either be empty (air) or filled with late magnesite, rutile or host rock minerals. Given their distribution and their habit, quartz, calcite, the talc group, most of the micas, some sulfurs (pyrite, gersdorffite), the clinopyroxene-amphibole series (diopside) and the "undefined series" (between talc and mica, altered micas?) may be protogenetic inclusions. The talc-magnesite-dolomite schist host rock and its presumed protolith are chemically analogous with these inclusions. The syngenetic inclusions are rounded sulfurs-oxides grains, sharp rutile grains on preferential growth planes, ferrichromite flakes, magnesite, Cr-film and "rounded-fussy" or elongated sharp thin sheets of clinochlore between growth planes. The habit of the syngenetic inclusions suggest a parallel growth with the emerald host, but few of the inclusions are also found among epigenetic inclusions. Epigenetic inclusions are small zircon grains on a prismatic face, rutile and magnesite in late fractures, clinochlore sheets as overplating and talc sheets from the matrix.

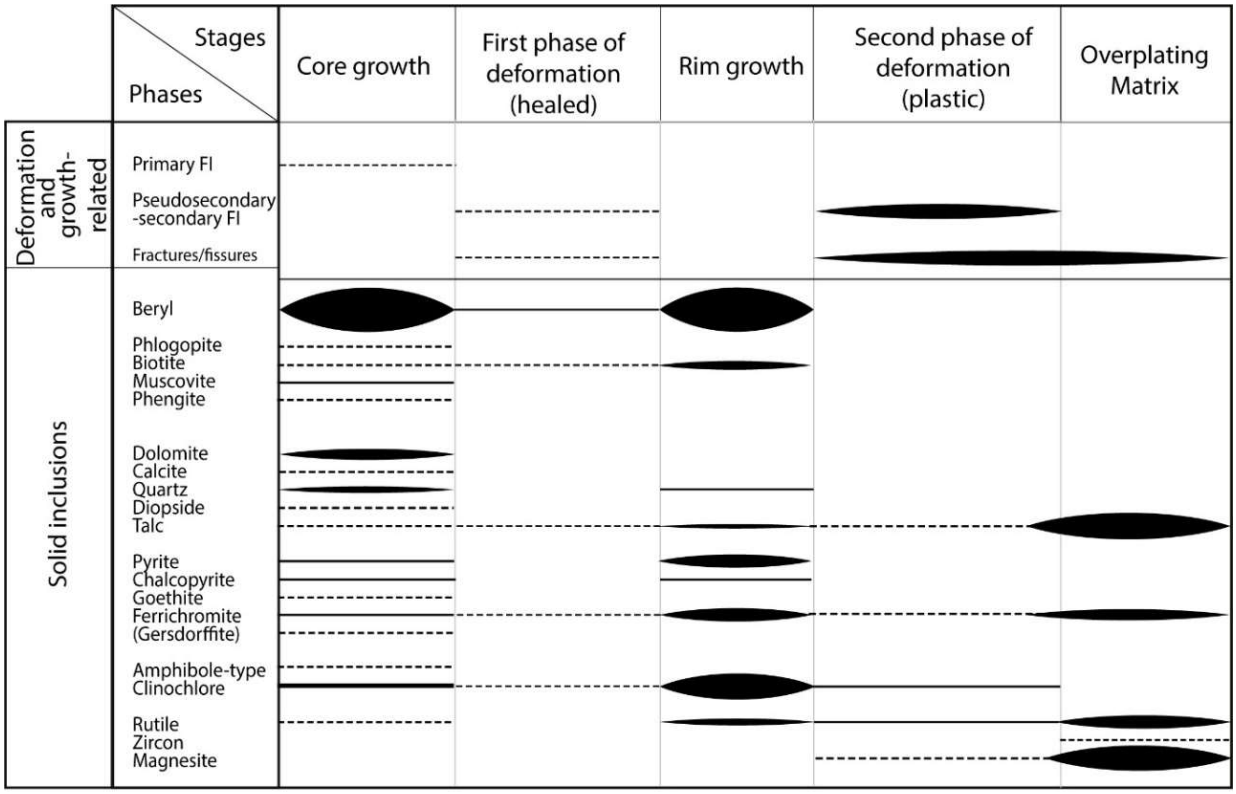

Figure 26: Paragenetic diagram. This diagram is the result of the merging of the paragenetic diagrams for each sample and is based on the distribution of the inclusions observed with the different methods.

The chemical variations of the emerald matrix need to be set aside to see clearly the chemical variations of the inclusions and connections. First, the protogenetic inclusions have formed with Al, K (forming Ms-Phg micas), Si (quartz), Ca, Mg (dolomite, amphibole), (Cu, Fe, S) (sulfurs). Then, inside syngenetic-epigenetic inclusions the present elements are Fe, Mg, Cr, V (forming Bt-Phl micas, clinochlore, ferrichromite, talc), Ca (magnesite), (Ti, Zr) (rutile, zircons). Regarding the emeralds' matrix for both considered samples, the cores hold more Mg, Na, while the rims contain more Cr, Fe. The elements composing the emerald matrix and the similar elements constituting the inclusions reflect the same availability or the same supplying source. The concentration differs between the matrix and certain inclusions: higher Fe or Cr concentration in inclusions than in the matrix, or the contrary. This can be explained by thermodynamic rules forcing elements to occupy preferential sites in the lattice of certain minerals or substitute others in the matrix of the beryl host (Schwarz et al., 1988).

Geological context and supplied elements

The supplying sources for each element forming the Mingora emeralds and their inclusions are listed below. As seen in the first chapters, the host rock in Mingora is the transformed assemblage of a magnesite-tlc-qtz-(magnetite-chromite) ± dolomite schist, with variability in the proportions across the Mingora deposit. The mineralization is either disseminated or hosted in tur ± ms ± em-qtz veins forming stockworks. For the ultramafic protolith of the Mingora ophiolite mélange to appear as it does today, it first had to endure a hydration (metamorphism) stage, before a structurally controlled carbonation stage (possibly amplified by CO_2 released during metamorphism (Arif et al., 1996). This was followed by multiple episodes of hydrothermalism creating tur, Cr-ms, em in qtz veins forming a stockwork.

The chemical elements forming the inclusions in the emeralds have either a proximal origin (in the protolith) or have been brought by the episodes of metamorphism and hydrothermalism. Cr is present in the chromite of the carbonated host rock as clusters/nodules; they may be pseudomorph of Cr-rich spinels present in the UM protolith (Arif et al., 2011). Cr-poor hydrothermal fluids confirm this origin (Kazmi and Snee, 1990). Mg, Mn, Cu could be inherited from the protolith and Ni from olivine specifically (Trommsdorff and Evans, 1974). Al-B-K-bearing hydrothermal mineralizing solutions brought Be(-B) and other scarce elements (As, Pb, Zr, Rb, Ba, W, Sn, Sr, Y). During the late stages of hydrothermalism, epigenetic sulfurs may have crystallized, due to the interaction between the altered host rock and the incoming fluids (low fO_2 needed). The Zn-enrichment of ferrichromite may have been introduced by hydrothermal alteration and "recrystallization under amphibolite facies conditions." (Arif et al., 2011).

The elements found in the emerald crystals in this study are well correlated with those described across the Mingora deposit. Minerals found in the tur ± ms ± em-qtz veins (Cr-rich muscovite-phengite, quartz), in the host rock (Ni-talc, magnesite, gersdorffite, (V-Zn)-ferrichromite, pyrite-chalcopyrite, dolomite, Mn-diopside) and those linked to hydrothermalism (Sc-halite, epigenetic zircons) are all found as inclusions, thus confirming the same interactions. However, the Bt-Phl micas were maybe formed before carbonatation: the large amount of chlorite could be the result of the alteration of micas because of their close composition. Ti (rutile, Ti-biotite, Ti-phlogopite) could have been brought by the same late hydrothermal solutions forming epigenetic zircons. The one small grain of goethite found in sulfurs could indicate fO_2 changes during growth. The zoning of the emerald matrix and the inclusions bring more information about chemical changes, temperatures variations (crystal growth, DUG session) occurring during the crystallization; moreover it may indicate several episodes of crystallization and deformation at the same time. This mirrors the composition and features observed in the host rock (Arif et al., 2011).

Chlorite thermometer

Microprobe data on clinochlore gives some information about the ion occupation for each site, which is related to the crystallization temperature. The chlorite group inclusions (Annex XXI), called clinochlore in this study (Deer et al., 2013), are more precisely described as pycnochlore (12 inclusions), clinochlore

(4 inclusions) or diabantite (1 inclusion) (Hey, 1954). The ion occupation for the considered inclusions leads, depending on the calculation, to an average temperature of 270,63°C (Cathelineau, 1988) or 274,75°C (Jowett, 1991). Both calculations assume 28 oxygens and consider full site occupancy with Fe^{2+}/Fe^{3+} and OH. The range of temperatures matches with some of the temperatures described at the end of the *Mingora deposit and genetic model* chapter. Furthermore, analyses are carried out on chlorites inclusions inside the core and on the rims, no obvious disparity between the values are revealed. Nevertheless, a second type of thermometry would be useful to better constrain the temperatures, for example microthermometry on multiphase fluid inclusions.

Conclusion and outlook on future analyses

To conclude, the Mingora emeralds and their inclusions reflect multiple episodes of crystallization through their growth structure; the regional geological context is embodied by their chemical variations. The relative proximity of the different supplying tectonic units, the movement of the transporting fluids (compression, permeability with thrust faulting, temperatures gradient) are common in a suture zone context. This tectonic context provides the necessary elements for the crystallization of emeralds and certainly still holds various gem deposits (Groat, 2007). The present study brings a partial description of the inclusions and their distribution. It confirms the chemical variations already observed (Arif et al., 2011; Kazmi and Snee, 1990) and brings some new insights. However, the chemical variations depending on the exact distribution inside the host rock are missing; chemical variations in the inclusions at deposit-scale could be useful.

The data presented in this study need to be completed and with other analyses. Systematic microprobe analyses on emerald crystals and their inclusions are crucial to better characterize the compositional changes of the hydrothermal solutions. Some specific trace elements found in inclusions or in the matrix are interesting for emerald identification. Another interesting analysis would be the dating of zircons on the surface or of the Cr-rich muscovite inclusions (provided that exchanges with the matrix are limited); such analyses could be correlated with the ages found by Dilles et al. (1994). Other analyses like thermometry on the sulfurs or on multi-phase inclusions would help to constrain the temperature of crystallization. All the observations carried out bring some valuable knowledge about the complexity of the Mingora deposit and hints about features of the Mingora emeralds.

References

Anderson, J.J., 2013. Bedrock Geology of Antarctica: A Summary of Exploration, 1831-1962, in: Hadley, J.B. (Ed.), Antarctic Research Series. American Geophysical Union, Washington, D. C., pp. 1–70. https://doi.org/10.1029/AR006p0001

Andrianjakavah, P.R., Salvi, S., Béziat, D., Rakotondrazafy, M., Giuliani, G., 2009. Proximal and distal styles of pegmatite-related metasomatic emerald mineralization at Ianapera, southern Madagascar. Mineralium Deposita 44, 817–835. https://doi.org/10.1007/s00126-009-0243-5

Arif, M., 2003. Sulphides and sulpharsenides in the emerald-hosting rocks from the Indus suture zone in Swat, NW Pakistan. Swiss Bulletin of Mineralogy and Petrology 83, 261-271(11).

Arif, M., 2000. Zincian, manganiferous chrome spinel from the Swat valley ophiolite, NW Pakistan. Geol. Bull. Univ. Peshawar 33, 103–110.

Arif, M., 1999. The emerald-hosting magnesite-rich rocks from Swat valley ophiolite, NW Pakistan. Geol. Bull. Univ. Peshawar 32, 63–70.

Arif, M., Fallick, A.E., Moon, C.J., 1996. The genesis of emeralds and their host rocks from Swat, northwestern Pakistan: a stable-isotope investigation 14.

Arif, M., Henry, D.J., Moon, C.J., 2011. Host rock characteristics and source of chromium and beryllium for emerald mineralization in the ophiolitic rocks of the Indus Suture Zone in Swat,

NW Pakistan. Ore Geology Reviews 39, 1–20. https://doi.org/10.1016/j.oregeorev.2010.11.006
Arif, M., Henry, D.J., Moon, C.J., 2010. Cr-bearing tourmaline associated with emerald deposits from Swat, NW Pakistan: Genesis and its exploration significance. American Mineralogist 95, 799–809. https://doi.org/10.2138/am.2010.3349
Arif, M., Moon, C.J., 2007. Nickel-rich chromian muscovite from the Indus suture ophiolite, NW Pakistan: Implications for emerald genesis and exploration. GEOCHEMICAL JOURNAL 41, 475–482. https://doi.org/10.2343/geochemj.41.475
Aurisicchio, C., Grubessi, O., Zecchini, P., 1994. Infrared spectroscopy and crystal chemistry of the beryl group. The Canadian Mineralogist 32, 55–68.
Behmenburg, C. (Ed.), 2001. Smaragd: der kostbarste Beryll, der teuerste Edelstein. Weise, München.
Bersani, D., Azzi, G., Lambruschi, E., Barone, G., Mazzoleni, P., Raneri, S., Longobardo, U., Lottici, P.P., 2014. Characterization of emeralds by micro-Raman spectroscopy: Characterization of emeralds. Journal of Raman Spectroscopy 45, 1293–1300. https://doi.org/10.1002/jrs.4524
Cathelineau, M., 1988. Cation site occupancy in chlorites and illites as a function of temperature. Clay Minerals 23, 471–485. https://doi.org/10.1180/claymin.1988.023.4.13
Chen, X.L., Chen, H., Lu, T.J., He, M.Y., 2016. Durability of Fracture-Filled Emeralds with a New Artificial Filler ExCel. Key Engineering Materials 680, 562–566. https://doi.org/10.4028/www.scientific.net/KEM.680.562
Deer, W.A., Howie, R.A., Zussman, J., 2013. An introduction to the rock-forming minerals, 3. edition. ed. The Minerological Society, London.
Di Pietro, J.A., 2008. 23rd Himalaya-Karakoram-Tibet Workshop (Extended Abstract). Himalayan Journal of Science, pp. 45–46.
Dilles, J.H., Snee, L.W., B.M. Laurs, 1994. Geology, Ar-Ar age and stable isotopes geochemistry of suture-related emerald mineralization, Swat, Pakistan, Himalayas, in: Proceedings of the Geological Society of America. Presented at the Annual Meeting, Seattle, WA, USA, p. A-311.
Freud, S., 1948. Vorlesungen zur Einführung in die Psychoanalyse (1916/17). Gesammelte Werke.
Fritsch, E., Rossman, G., 1988. An update on color in gems. Part 3: Colors caused by band gaps and physical phenomena. Gems & Gemology 24, 81–102.
Gemological Institute of America, 2016. Gem Identification Lab Manual.
Gemworld, 2014. World of Color Communication System.
Giuliani, G., 2000. Oxygen Isotopes and Emerald Trade Routes Since Antiquity. Science 287, 631–633. https://doi.org/10.1126/science.287.5453.631
Giuliani, G., Groat, L.A., Marshall, D., Fallick, A.E., Branquet, Y., 2019. Emerald Deposits: A Review and Enhanced Classification. Minerals 9, 105. https://doi.org/10.3390/min9020105
Giuliani, G., Groat, L.A., Marshall, D.D., 2018. Emerald Deposits in the 21st Century. InColor 22–32.
Groat, L.A. (Ed.), 2014. Geology of gem deposits, 2nd ed, Short course series delivered at the Tucson Gem and Mineral Show, Tucson, Arizona / Mineralogical Association of Canada. Mineralogical Assoc. of Canada, Montreal.
Groat, L.A. (Ed.), 2007. Geology of Gem deposits: short course delivered in association with the annual meeting of the Geological Association of Canada and the Mineralogical Association of Canada, Yellowknife, Northwest Territories, 21 - 22 May, 2007, Short course series / Mineralogical Association of Canada. Mineralogical Assoc. of Canada, Montreal.
Gübelin, E., Koivula, J.I., 1997. Photoatlas of inclusions in gemstones, Vol. 1. ABC Edition, Zurich.
Gübelin, E.J., 1982. Gemstones of Pakistan: Emerald, Ruby, and Spinel. Gems & Gemology 18, 123–139. https://doi.org/10.5741/GEMS.18.3.123
Gübelin, E.J., Koivula, J.I., 2008. Photoatlas of inclusions in gemstones, Vol. 3. Opinio, Basel.
Hänni, H.A., 1991. The case for blue-green emerald. Jewellery News Asia 88–90.
Henn, U., 1988. Untersuchungen an Smaragden aus dem Swat-Tal, Pakistan. Zeitschrift der Deutschen Gemmologischen Gesellschaft 37, 121–127.
Hey, M.H., 1954. A new review of the chlorites. The mineralogy magazine and journal of the mineralogical society 30, 278–292.

Jowett, E.C., 1991. Fitting iron and magnesium into the hydrothermal chlorite geothermometer. Presented at the GAC/MAC/SEG Joint Annual Meeting, Toronto.
Karampelas, S., Al-Shaybani, B., Mohamed, F., Sangsawong, S., Al-Alawi, A., 2019. Emeralds from the Most Important Occurrences: Chemical and Spectroscopic Data. Minerals 9, 561. https://doi.org/10.3390/min9090561
Kazmi, A.H., Lawrence, R.D., Anwar, J., Snee, L.W., Hussain, S., 1986. Mingora emerald deposits (Pakistan); suture-associated gem mineralization. Economic Geology 81, 2022–2028. https://doi.org/10.2113/gsecongeo.81.8.2022
Kazmi, A.H., Snee, L.W., 1990. Emeralds of Pakistan Geology, Gemology and Genesis. Springer Verlag.
Kievlenko, E.I., 2003. Geology of gems, English ed. ed. Ocean Pictures, Littleton, CO.
Lafuente, B., Downs, R.T., Yang, H., Stone, N., 2015. 1. The power of databases: The RRUFF project, in: Armbruster, T., Danisi, R.M. (Eds.), Highlights in Mineralogical Crystallography. DE GRUYTER, Berlin, München, Boston, pp. 1–30. https://doi.org/10.1515/9783110417104-003
Le Thi Thu, H., 2008. Microscopic, chemical and spectroscopic investigations on emeralds of various origins. Mainz.
Lewis, I.R. (Ed.), 2001. Handbook of Raman spectroscopy: from the research laboratory to the process line, 4. print. ed, Practical spectroscopy. CRC Press, New York.
Maluski, H., Matte, P., 1984. Ages of alpine tectonometamorphic events in the northwestern Himalaya (northern Pakistan) by 39Ar/40Ar method. Tectonophysics 3, 1–18.
Marshall, D., Downes, P., Ellis, S., Greene, R., Loughrey, L., Jones, P., 2016. Pressure–Temperature–Fluid Constraints for the Poona Emerald Deposits, Western Australia: Fluid Inclusion and Stable Isotope Studies. Minerals 6, 130. https://doi.org/10.3390/min6040130
Moroz, I., Roth, M., Boudeulle, M., Panczer, G., 2000. Raman microspectroscopy and fluorescence of emeralds from various deposits. Journal of Raman Spectroscopy 31, 485–490. https://doi.org/10.1002/1097-4555(200006)31:6<485::AID-JRS561>3.0.CO;2-M
O'Donoghue, M., 2008. Gems: their sources, descriptions and identification. N.A.G., London.
Qiao, X., Zhou, Z., Schwarz, D.T., Qi, L., Gao, J., Nong, P., Lai, M., Guo, K., Li, Y., 2019. Study of the Differences in Infrared Spectra of Emerald from Different Mining Areas and the Controlling Factors. The Canadian Mineralogist 57, 65–79. https://doi.org/10.3749/canmin.1800042
Reeves, C., 2014. The position of Madagascar within Gondwana and its movements during Gondwana dispersal. Journal of African Earth Sciences 94, 45–57. https://doi.org/10.1016/j.jafrearsci.2013.07.011
Reshma, B., Sakthivel, R., Mohanty, J., 2017. Characterization of Low Grade Natural Emerald Gemstone. Journal of Geology & Geophysics 06. https://doi.org/10.4172/2381-8719.1000271
Rondeau, B., Notari, F., Giuliani, G., Michelou, J.-C., Martins, S., Fritsch, E., Respinger, A., 2003. La mine de Piteiras, Minas Gerais, nouvelle source d'émeraude de belle qualité au Brésil. Revue de Gemmologie 9–25.
Schmetzer, K., Berdesinski, W., Bank, H., 1984. Über die Mineralart Beryll, ihre Farben und Absorptionsspektren. Gemmologie: Zeitschrift der Deutschen Gemmologischen Gesellschaft 23, 5–39.
Schwarz, D., 1994. Emeralds from the Mananjary Region, Madagascar: Internal Features. Gems & Gemology 30, 88–101. https://doi.org/10.5741/GEMS.30.2.88
Schwarz, D., Hänni, H.A., Martin Jr, F.L., Fischer, M., 1988. The emeralds of Fazenda Boa Esperança, Tauá, Ceará, Brazil: occurrence and properties. The Journal of Gemmology 21, 168–178. https://doi.org/10.15506/JoG.1988.21.3.168
Schwarz, D., Henn, U., 1992. Emeralds from Madagascar. Journal of Gemmology 23, 140–149.
Schwarz, D., Pardieu, V., 2009. Emeralds from the Silk Road Countries – A Comparison with Emeralds from Colombia 7.
Schwarz, D., Schmetzer, K., 2002. The definition of Emerald – the green variety of beryl colored by chromium and/or vanadium. Emeralds of the World 74–78.

Siivola, J., Schmid, R.A., 2007. List of mineral abbreviations. Recommendations by the IUGS Subcommission on the Systematics of Metamorphic Rocks. A systematic nomenclature for metamorphic rocks 1–14.
Smith, C., 2009. Inside emeralds. Rapaport Magazine 32.
Sturm, R., 2010. Microscopy and Microanalysis of Magmatic and Metamorphic Minerals—Part 2: Feldspar. Microscopy Today 18, 18–24. https://doi.org/10.1017/S155192951000026X
Thompson, D.B., Bayens, C.J., Morgan, M.B., Myrick, T.J., Sims, N.E., 2017. Photoluminescence Spectra of Emeralds from Colombia, Afghanistan, and Zambia. Gems & Gemology. https://doi.org/10.5741/GEMS.53.3.296
Trommsdorff, V., Evans, B.W., 1974. Alpine metamorphism of peridotitic rocks. Schweizerische Mineralogische und Petrographische Mitteilungen 333–352.
Vapnik, Ye., Moroz, I., Roth, M., Eliezri, I., 2006. Formation of emeralds at pegmatite-ultramafic contacts based on fluid inclusions in Kianjavato emerald, Mananjary deposits, Madagascar. Mineralogical Magazine 70, 141–158. https://doi.org/10.1180/0026461067020320
Wood, D.L., Nassau, K., 1968. The characterization of beryl and emerald by visible and infrared absorption spectroscopy. American Mineralogist 53, 777–800.
Zwaan, J.C., Seifert, A.V., Vrána, S., Laurs, B.M., Anckar, B., (Skip) Simmons, W.B., Falster, A.U., Lustenhouwer, W.J., Muhlmeister, S., Koivula, J.I., Garcia-Guillerminet, H., 2005. Emeralds from the Kafubu Area, Zambia. Gems & Gemology 41, 116–148. https://doi.org/10.5741/GEMS.41.2.116

Annexes

Annex I: Microscope description of the emerald samples

Sample number	Category	Assemblage
FN12490	Inclusions distribution (minerals, fluid inclusions, fractures)	Crystal 1: A deep fracture crossing the samples with a fuzzy zone around and a strong color zonation 5-6 µm-long on the rim. Crystal 2: Large wavy fractures //C
	Fluid Inclusions	Crystal 1: Numerous FI, preferentially biphase situated in the center of the sample. Distinct planes for the different generation of FI. Crystal 2: Few primary biphase FI.
	Minerals	Crystal 1: Magnesite: As overplating. Crystal 2: Magnesite: Large whitish inclusion included on the rim.
FN12491	Inclusions distribution (minerals, fluid inclusions, fractures)	Growth zonation, visible with stronger color on the rims. Stronger tons are coupled with micas and chlorite. Cloud of minute inclusions (majority of micas), higher density of that cloud at the top and at the bottom of the crystal. Some big euhedral dolomite in the center of the sample. Visible cleavage planes. Brittle fractures //C (wavy) or ⊥C. FI fingerprint on //C (wavy) or ⊥C >>The fingerprints //C seem to be linked with the fractures.
	Paragenesis	dol-(cal)-micas-chl-pinpoints clouds-//C FI growth tube >> rut-chl-⊥C FI >> mag-tlc
	Fluid Inclusions	Rarely blocky, growth tubes or fluid pinpoint FI. The major part are rounded and elongated and undulated //C fingerprints.
	Minerals	Micas: Small platy and stacked columnar micas, often lined on //C. Chromite: Thin film on dolomite grains or as in-filling, //C FI. Chlorite: Numerous fractures around the big chlorite inclusion. Also forming as small deformed elongated flat sheets. Dolomite: Present as small grains in the cloudy area with micas, or as isolated big euhedral crystals, sometimes with twinning. Calcite (?): Small grains, look like dolomite but less transparent. Talc: Lookalike micas grains, or as overplating. Rutile: Small anomorpheous in-filling, or as minute grains in ⊥C fracture planes.
FN12969	Inclusions distribution (minerals, fluid inclusions, fractures)	Fractures with/without FI following cleavage planes. Small platelets of micas, all forms of FI in the center of the sample (cloudy appearance). The FI are "aligned" on the //C planes and ⊥C planes. The larger crystals are also in the core. Rutile crystals+aggregates and platy chlorite situated on the regrowth zone. Higher density of rutile aggregates along deformation planes. Wavy fractures //C.
	Paragenesis	Pinpoints FI+growth tubes-ms-dol-(small granular)-rut >> chl-mag-bt-rut
	Fluid Inclusions	Basal secondary fluid inclusions fingerprint. Cloud of fluid pinpoint cloud and negative crystals. Minute straight growth tubes //C.
	Minerals	Chlorite: Large and elongated darker green translucent on the rim or as in-filling between 2 growth zones. Micas: Quantity of colorless hexagonal platelets, few stacked ones. Rutile: Small orange minerals clusters, mixed with bigger orange-black biterminated and twinning crystals or as white mossy aggregates. Dolomite: Octahedral isolated crystal. Quartz: Occurring as small grains.
FN12970	Inclusions distribution (minerals, fluid inclusions, fractures)	Slight darker green color zonation on the rim of the sample. Dark green chlorite distributed at the base of the crystal, micas forming with dolomite crystals in the center. Clear difference between the regrowth and the core, displaying weakness on the cleavage plane. Secondary fractures with FI. Visible cleavage. Pinpoint FI aligned on cleavage planes.
	Fluid Inclusions	Pinpoint FI either in cloudy area or lined on //C and on secondary planes. Mainly small growth tubes lined on //C.
	Minerals	Chlorite: Green dark platelets, elongated, parallel to the facet, near the crystal face. Micas: Colorless wavy mica and as small platelets. Dolomite: Multiple small isolated colorless euhedral crystals, few twinning. Rutile: Beige aggregates as filling of fractures.

Sample number	Category	Assemblage
FN12971	Inclusions distribution (minerals, fluid inclusions, fractures)	More rutile and dark chlorites near the surface. More micas platelets in the light-colored areas, more FI planes and dolomite in the saturated color areas. Obvious shearing fractures. Majority of FI planes // C. FI //C plane get sheared by late shearing fractures.
	Fluid Inclusions	cloudy pinpoint FI, set of FI on //C.
	Minerals	Rutile: Mossy orange dust or aggregates in the cleavage planes or directly under the surface as a yellow dust. Chlorite: Elongated dark green sheets. Quartz: Big pseudo-euhedral crystal. Micas: Small platelets or longer ones as accordion-type. Talc: As overplating. Metallic inclusions (?): Minute dark opaque inclusions.
FN12972	Inclusions distribution (minerals, fluid inclusions, fractures)	Rutile grains close to the surface. Growth tubes and //C FI are located in the cleanest part of the stone.
	Paragenesis	Blocky 2-phase FI + growth tubes-dol-(small platy) >> mag-chl-(rut-cr)
	Fluid Inclusions	Growth tubes
	Minerals	Rutile: Biterminated and twinning crystals, mossy aggregates as dusting. Micas: Small greenish dark platelets. Chromite: Aggregates into the rim. Magnesite: Whitish intergrowth layer. Talc: Whitish overplating. Chlorite: Outcropping massive chlorite. Metallic inclusions (?): Small dark opaque platy.
FN12973	Inclusions distribution (minerals, fluid inclusions, fractures)	Less FI on //C planes and cleavage planes compared to the other samples. Mossy rutile well developed near the surface with growth tubes, more micas platelets in the center. Net regrowth of lighter colored emerald on a micas-rich core, sharp limit with rutile aggregates.
	Paragenesis	dol+cr-films-pinpoints FI+growth tubes-mica >> cr-films-rut-micas-tlc-mag
	Fluid Inclusions	Growth tubes //C.
	Minerals	Micas: Small platelets from colorless to dark green translucent micas. Chromite: Chromite platelets/films with hole inside the inclusion. Rutile: mossy orangy-yellowish-beige aggregates Chlorite: Massive lamellar dark green mineral outcropping. Dolomite: Sharp euhedral aggregates with developed crystal faces.
FN12974	Inclusions distribution (minerals, fluid inclusions, fractures)	High density (poor clarity) of small micas platelets in the center of the sample. Pinpoint FI are aligned on cleavage planes or on //C plane. Set of wavy vertical fractures without FI, and circular //C. Big crystals stand also in the proximity of the core. Stronger color layers at the surface of the crystal.
	Paragenesis	dol+cr-films-micas+qtz-pinpoints FI >> chl-qtz-mg-rut
	Fluid Inclusions	Numerous pinpoint FI //C straight tubes
	Minerals	Chlorite: Large and elongated and wavy darker green translucent near the surface. Micas: Small columnar platy micas. Chromite: As small hole-platelets or as films on dol-xtl. Dolomite: Near-outcropping central twin whitish crystal and small ones coupled with pinpoint FI. Magnesite: Whitish plating and outcropping. Rutile: Small aggregates forming dust.

Sample number	Category	Assemblage
FN12975	Inclusions distribution (minerals, fluid inclusions, fractures)	Visible cleavage planes, FI following the cleavage planes. FI on //C planes FI on deformation planes Deformation factures, cleavage fractures, wavy fracture //C. Large pyrite grains formed near the surface and are aligned on the cleavage planes.
	Paragenesis	py+cpy+gt-rut >> mag
	Fluid Inclusions	2 cloudy area composed of aligned minute FI.
	Minerals	Micas: Rare, platy. Pyrite: Large aggregates or single dodecahedron grain. Rutile: Rare small orange aggregates. Talc: Whitish plating. Dolomite: Whitish massive fibrous outcropping on the facet.
FN12976	Inclusions distribution (minerals, fluid inclusions, fractures)	Clear growth zonation with chromite layer between the emerald generations. Dolomite-(calcite-magnesite), FI and pyrite in the core. Mica, chromite, whitish in-filling on the rim.
	Fluid Inclusions	Blocky minute 2-phase inclusions on plane, growth tubes.
	Minerals	Chromite: Platelets in the second emerald generation layer. Pyrite: Small central deformed pyritohedral. Micas: Small platelets or accordion-like. Talc: As overplating. Magnesite: Large whitish plating and fracture filling.
FN129777	Inclusions distribution (minerals, fluid inclusions, fractures)	Lighter tone compared to the other samples, majority of cloudy micas zone, along with dolomite crystals. Plating with dark green mineral on the surface and magnesite, clear delimitation, no zoning.
	Fluid Inclusions	Cloud of pinpoint FI
	Minerals	Micas: Platelets at the base of the crystal. Rutile: Small mossy aggregates. Dolomite: Sharp euhedral aggregates. Talc: Small cubic fluffy crystal or as overplating. Chlorite: dark green mineral outcropping and as platelets
FN12978	Inclusions distribution (minerals, fluid inclusions, fractures)	Multiple micas and FI inclusions in the near-colorless core, green rims with color banding.
	Minerals	Chlorite: Dark green mineral as platelets. Micas: As small platelets. Pyrite: Some isolated grains. Chromite: Cr-film filling fractures. Talc: Late plating.
FN12979	Inclusions distribution (minerals, fluid inclusions, fractures)	Majority of the micas and FI stand in the middle of the both crystals. Rutile and color saturation come later. More shearing planes with FI near the fractures on the cleavage planes. Color zonation core-rim.
	Fluid Inclusions	growth tubes //C
	Minerals	Rutile: As aggregates and as mossy dust. Micas: accordion-type

Sample number	Category	Assemblage
FN12980	Inclusions distribution (minerals, fluid inclusions, fractures)	Poor color and no color zonation. First is the micas cloud with FI and dolomite, then rutile come later with chlorite. Fractures without FI.
	Fluid Inclusions	FI plane //C
	Minerals	Micas: Wavy platelets, or as small cloud without preferential orientation. Dolomite: Euhedral transparent crystal. Rutile: Mossy aggregates. Talc: Whitish (sheets) as plating. Chlorite: Green blocky overplating.
FN12981	Inclusions distribution (minerals, fluid inclusions, fractures)	Random fractures with blue flash effect and with no FI.
	Fluid Inclusions	Long growth tubes
	Minerals	Chlorite: Wavy platelets with IF Dolomite: Small euhedral translucent crystals.

Annex II: Supplementary microphotography pictures

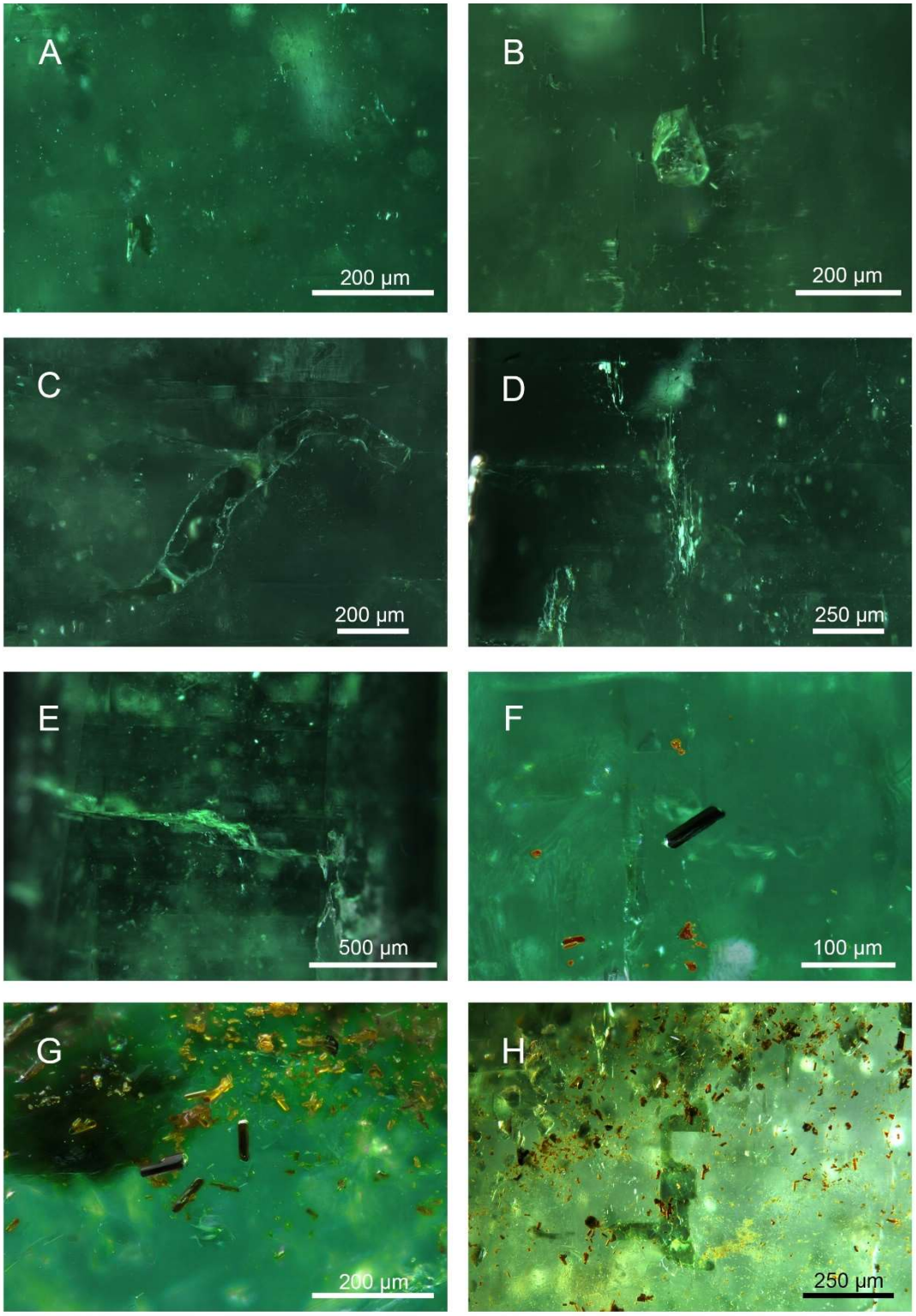

*Figure 27: **A** A cloud of fluid inclusions coupled with few micas sheets (FN12491-3, ethanol, darkfield). **B** A dolomite crystal with elongated fluid inclusions, biphase growth spike and growth-restrictions comb (FN12491-5, ethanol, darkfield). **C** Undulating chlorite sheet, close to the crystal face (FN12491-7, ethanol, darkfield). **D** Jagged primary fluid inclusions plane and visible cleavage plane on the crystal surface (FN12491-8, ethanol, darkfield). **E** Late fracture following the cleavage planes through the sample (FN12491-11, ethanol, darkfield). **F** Black acicular crystal of rutile with smaller grains around (FN12969-2, ethanol, brightfield). **G** Black acicular crystals of rutile with smaller cluster of grains around (FN12969-5, ethanol, brightfield). **H** Orange rutile grains of different size and saturation, and geometrical thin sheet of chlorite following cleavage planes and primary fluid inclusion plane (FN12969-6, ethanol, brightfield).*

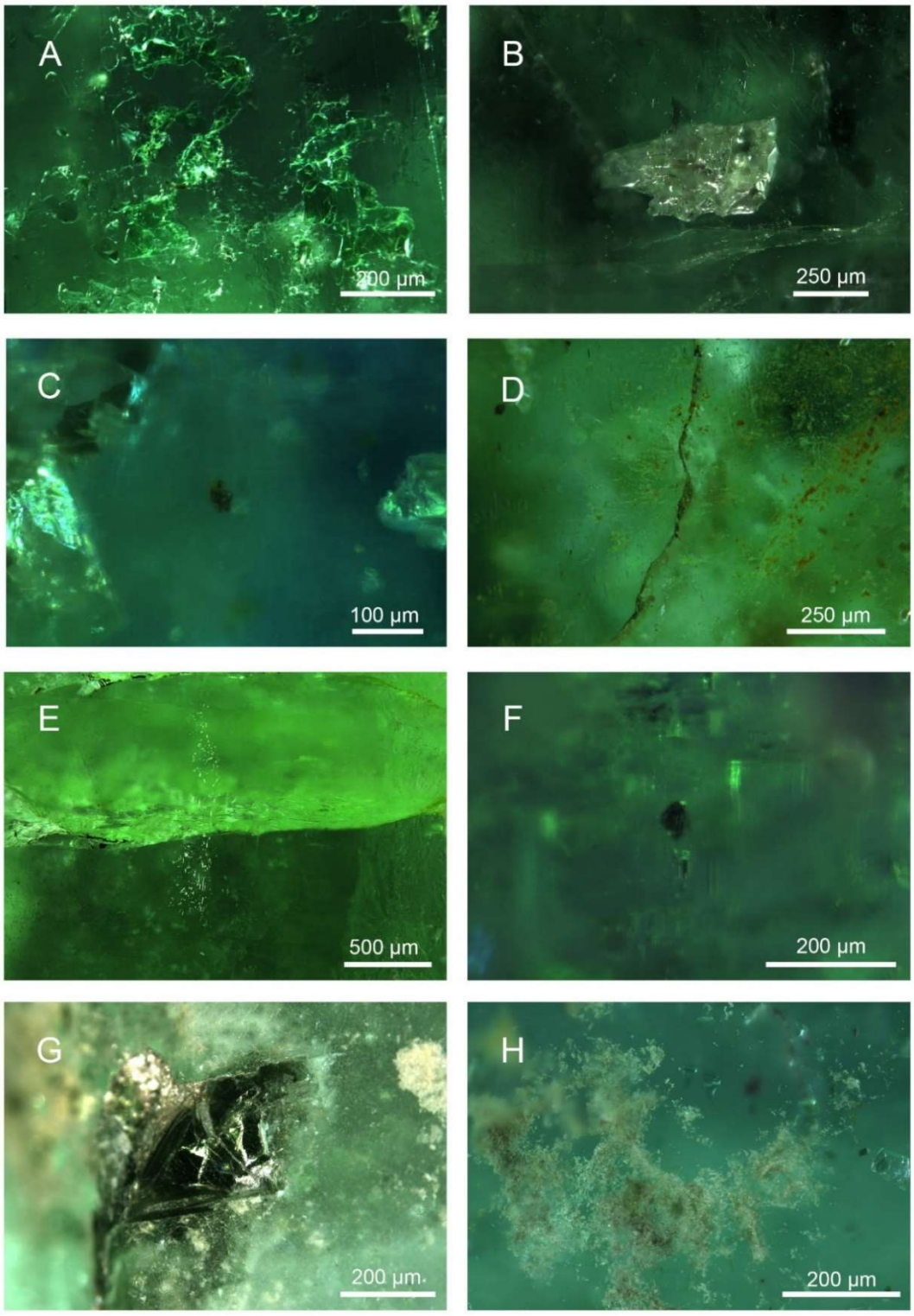

*Figure 28: **A** Rounded or geometrical chlorite sheets (FN12969-7, ethanol, darkfield). **B** An anhedral dolomite crystal (FN12969-8, ethanol, darkfield). **C** Granular brown aggregates (FN12969-9, ethanol, darkfield). **D** A undulating surface-reaching late fracture, parallel to C-axis (FN12969-11, ethanol, darkfield). **E** A late fracture cross-cutting a primary fluid inclusions plane (FN12971-3, ethanol, darkfield). **F** Small unidentified platy dark mineral surrounded by blocky fluid inclusions (FN12972-3, ethanol, darkfield). **G** Overplating chlorite (FN12973-2, air, brightfield). **H** Beige mossy rutile aggregate (FN12973-4, ethanol, brightfield).*

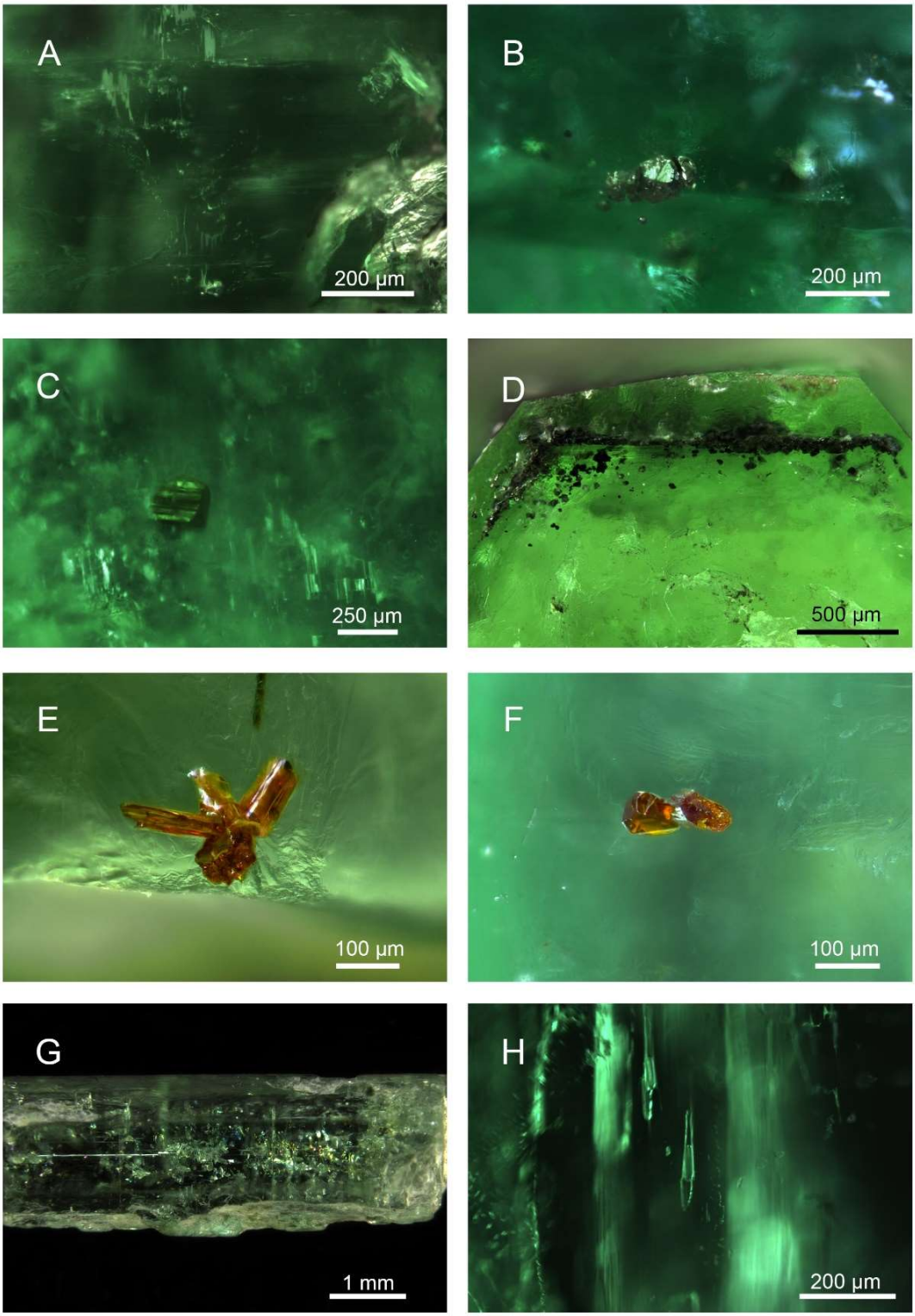

*Figure 29: **A** A jagged primary fluid inclusions plane (FN12975-4, ethanol, darkfield). **B** A pseudo-octahedral pyrite grain in aggregate with smaller ones (FN12975-6, ethanol, darkfield). **C** Striated pseudo-euhedral pyrite grain surrounded by a cloud of minute fluid inclusions and blocky two-phase inclusion //C (FN12976-3, ethanol, darkfield). **D** Layers of «sharp chromites» flakes (Kazmi and Snee, 1990, Gübelin and Koivula, 2008) restricted on a single crystallization plane ⊥C view (FN12976-5, ethanol, darkfield). **E** Twinning of rutile (FN12979-2, ethanol, darkfield). **F** Twinning of rutile (FN12979-3, ethanol, darkfield). **G** Unidentified accordion-like micas in the center of a crystal; the diffraction colors are created by the different micas crystal planes (FN12981-2, ethanol, darkfield). **H** Two elongated biphase fluid inclusions //C (FN12984-4, ethanol, darkfield).*

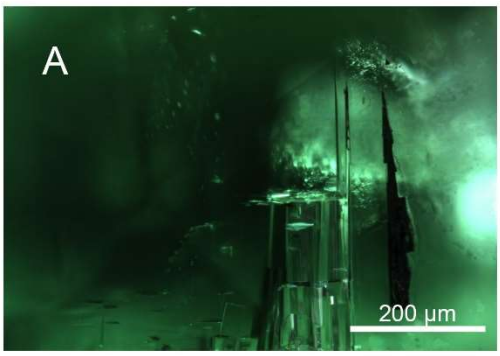

*Figure 30: **A** Flat fluid inclusions and growth restrictions (FN12984-6, ethanol, darkfield).*

Annex III: Pictures of the rock samples collected in Mingora (April 2019)

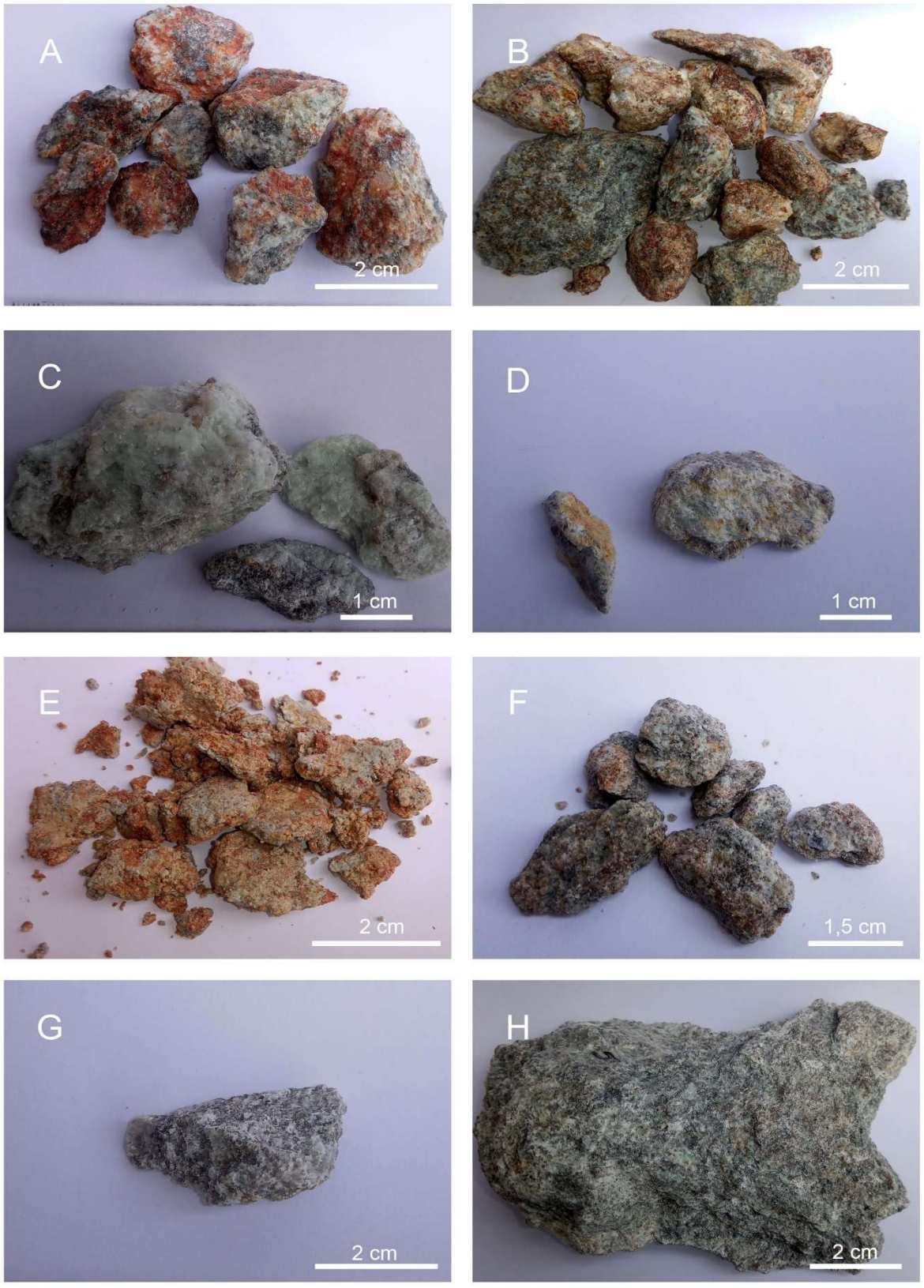

*Figure 31: **A** Alteration near a fault (Wall, LC-center-1). **B** Alteration near a fault (Wall, LC-center-2). **C** Talc near mineralization (Wall, LC-center-3). **D** Talc-magnesite schist without mineralization (Wall, LC-khalid-1). **E** Altered talc schist next to a fault zone, close to the working face (Wall, LC-khalid-2). **F** Altered talc schist next to a fault zone, close to the working face (Wall, LC-khalid-3). **G** Talc schist at the working face (Wall, LC-khalid-4). H Mineralized section (Wall, LC-khalid-5).*

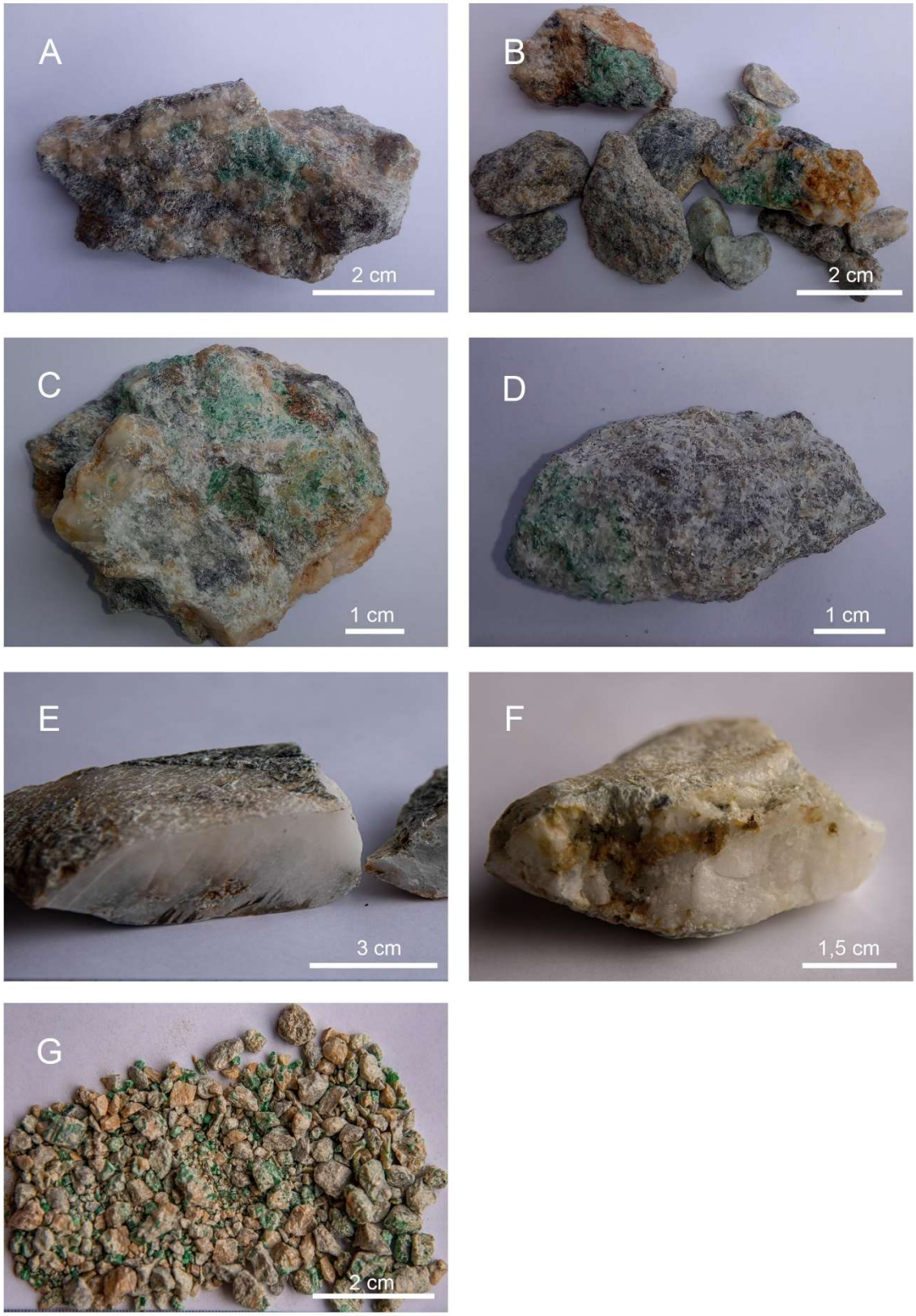

*Figure 32: **A** Mineralized section (Wall, LC-khalid-6). **B** Mineralized section (Wall, LC-khalid-7). **C** Mineralized section (Wall, LC-khalid-8). **D** Mineralized section (Wall, LC-khalid-9). **E** Quartz vein as rock waste (Floor, LC-khalid-10). **F** Quartz vein as rock waste (Floor, LC-khalid-11). **G** Mine-run after screening (LC-khalid-12)*

Annex IV: Field pictures of the sampling in Khalid and Center Tunnel in Mingora (April 2019)

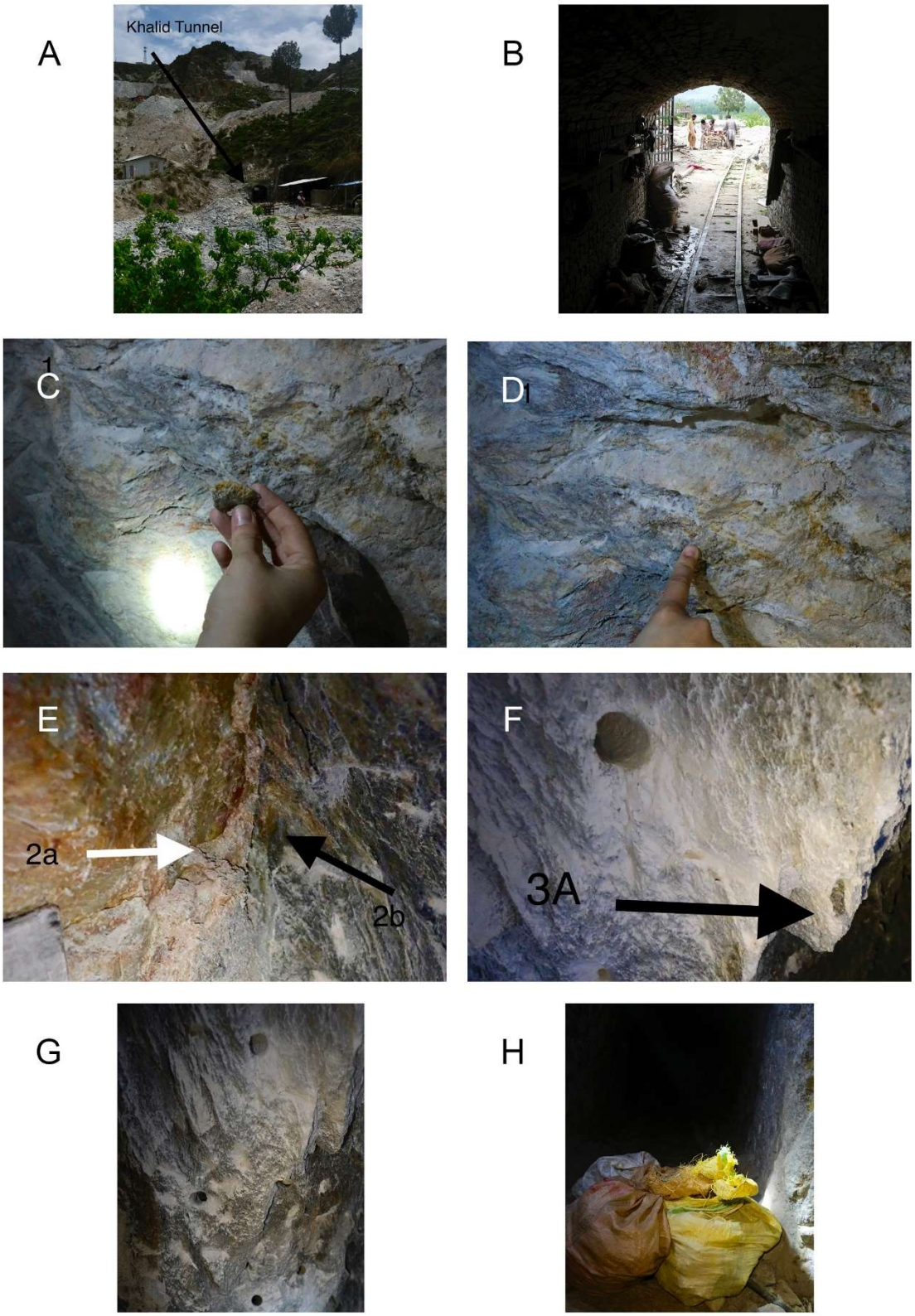

*Figure 33: Pictures and description by Jean-Claude Michelou (Imperial Colors Co., Ltd.). **A** Outside view of the Khalid Tunnel. **B** The direct entrance of the Khalid Tunnel. C Talc-schist without mineralization (LC-khalid-1). **D** Other view of talc-schist without mineralization (LC-khalid-1). **E** Fault zone with mineralization, close to the production zone (LC-khalid-2, 3). **F** Wall of the working zone (LC-khalid-4). **G** Wall of the working zone of the Khalid Tunnel. Ore is packed in bags before taking out in Khalid Tunnel.*

Figure 34: Pictures and description by Jean-Claude Michelou (Imperial Colors Co., Ltd.). ***A*** *Ore production of the day (LC-khalid-5, 10, 11, 12).* ***B*** *Washing and sorting of the ore production of the day at Khalid Tunnel.* ***C*** *Washing and sorting of the ore production of the day at Khalid Tunnel.* ***D*** *View from a pulling machine, helping to take the ore out of the Center Tunnel mine.* ***E*** *Entrance of the Center Tunnel.* ***F*** *A Miner with a pick at Center Tunnel.* ***G*** *Miner with jackhammer at Center Tunnel.* ***H*** *In the front of the working face in Center Tunnel, not producing for the last 9 months.*

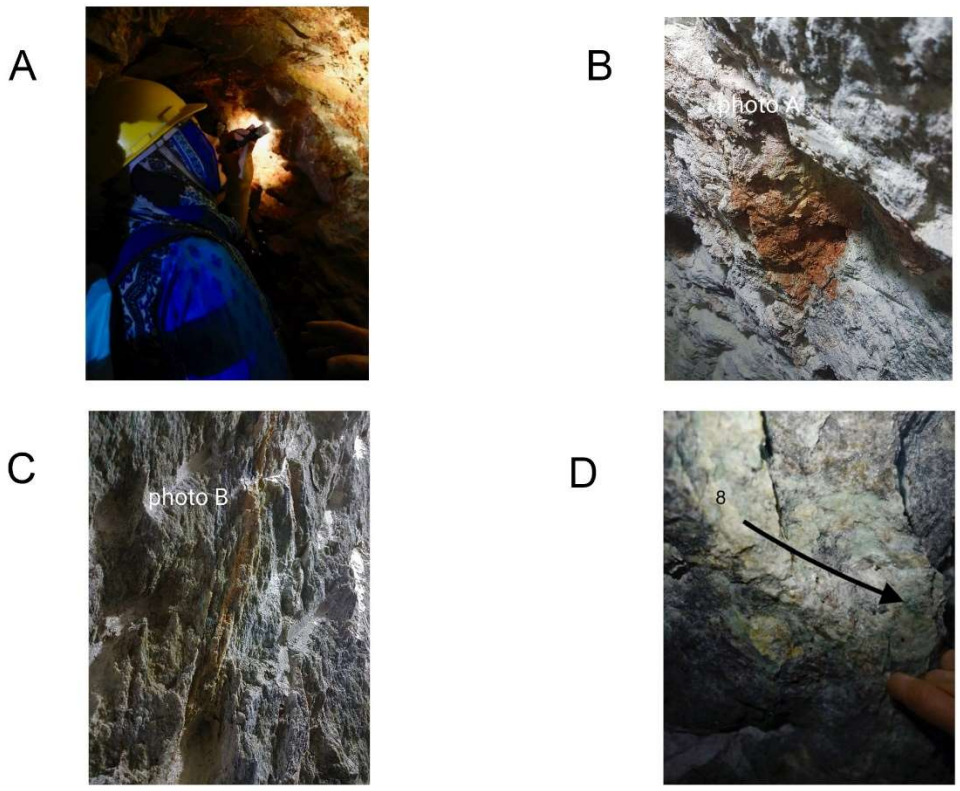

*Figure 35: Pictures and description by Jean-Claude Michelou (Imperial Colors Co., Ltd.). **A** View in the Center tunnel. **B** Sample from a fault near the working face (LC-center-1). **C** Sample from a fault near the working face (LC-center-2). **D** Mineralization zone in the tunnel (LC-center-3).*

Annex V: Supplementary UV-Vis-Nir Spectrometry analyses

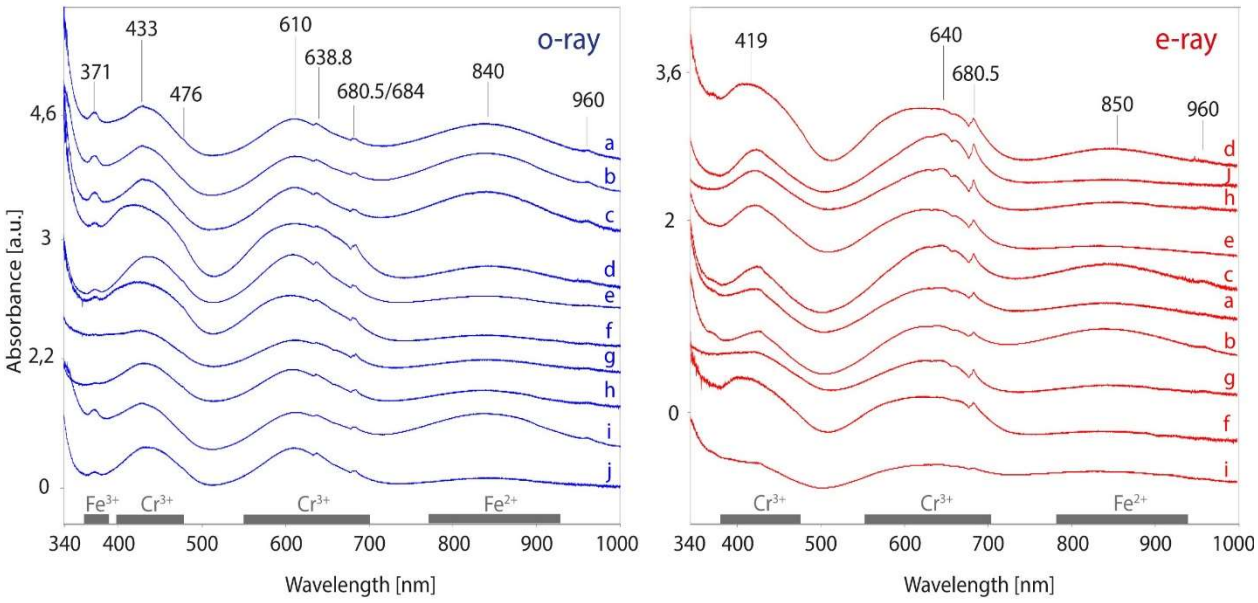

Samples: a (FN12980), b (FN12969), c (FN12977), d (FN12976), e (FN12968), f (FN13156), g (FN12981), h (FN12979), i (FN12973), j (FN12984)

Figure 36: 10 supplementary UV-Vis-NIR spectrometry analyses on the emerald samples.

Annex VI: IR Spectroscopy analysis

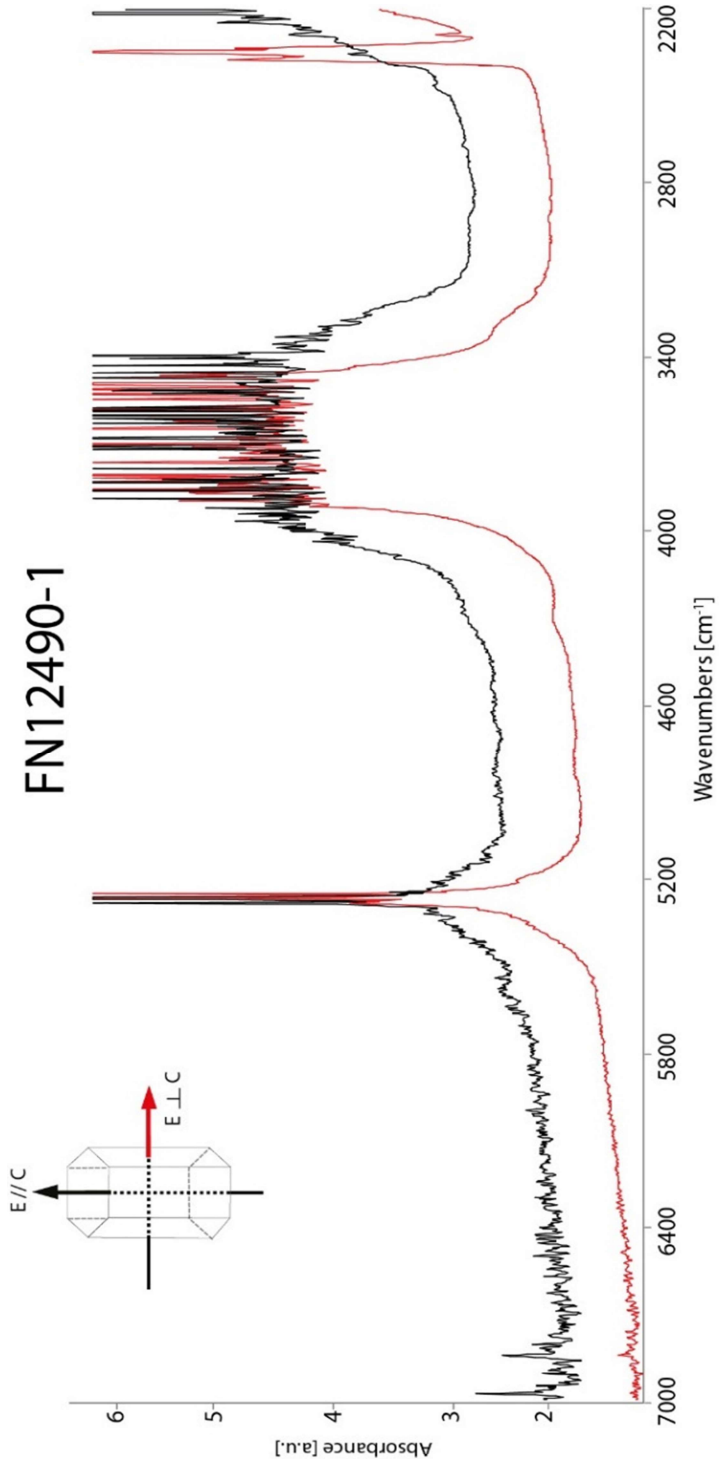

Figure 37: Absorbance IR spectrum for FN12490-1 sample.

Annex VII: Selection of Raman Microspectrometry spectra on emerald samples

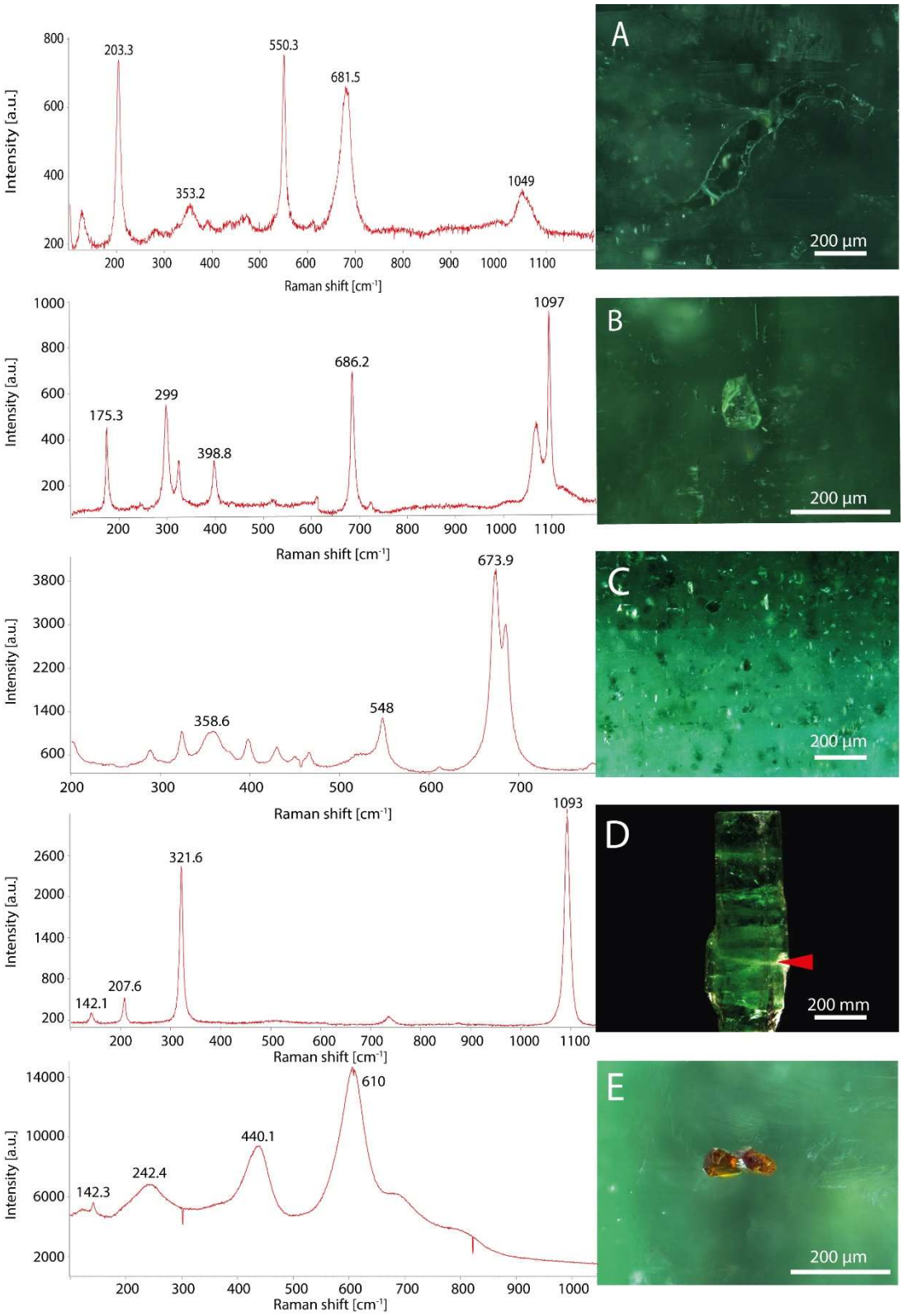

Figure 38: All the spectra are unprocessed or unmodified by any kind of smoothing techniques. ***A*** *Difficult spectral signature of this thin clinochlore sheet (FN12491, polished).* ***B*** *Spectral signature of a dolomite grain deep inside the crystal (FN12491, polished).* ***C*** *Phlogopite cloud also detected by Raman signature (FN12970, polished).* ***D*** *Magnesite filling spectrum on that rough crystal face (FN12972, rough).* ***E*** *Rutile twins near the surface producing a clear spectrum (FN12979, rough).*

Annex VIII: All Raman Microspectrometry spectra

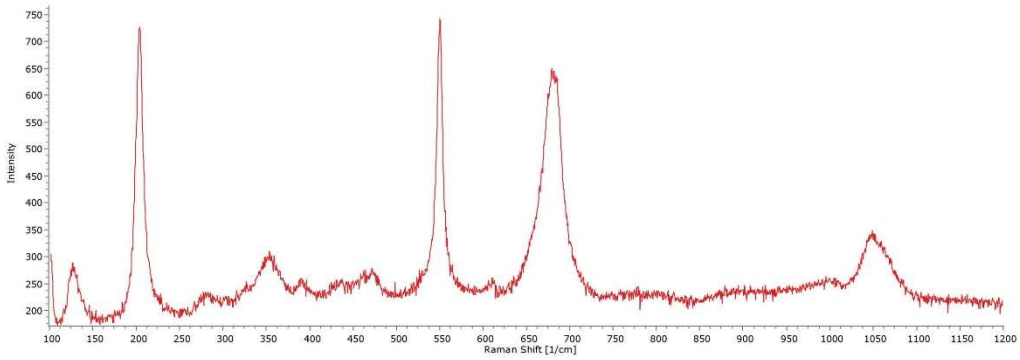

FN12491-clinochlore

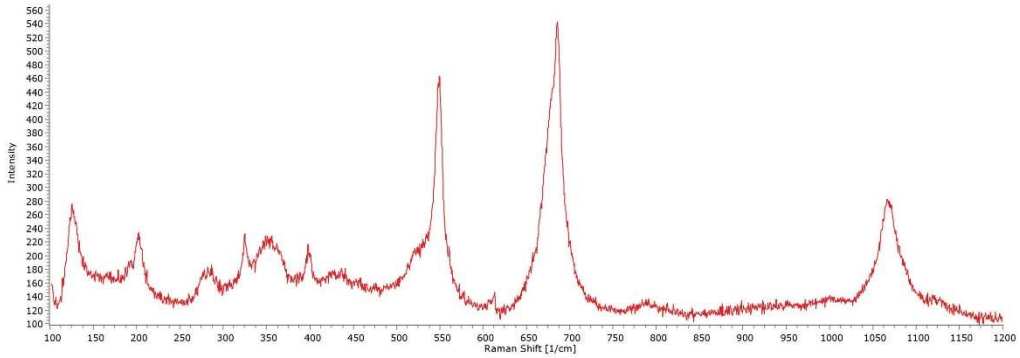

FN12491-clinochlore-2

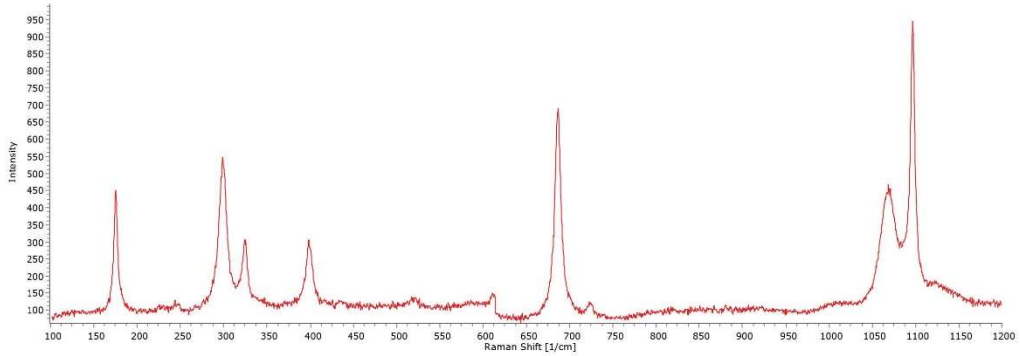

FN12491-dolomite

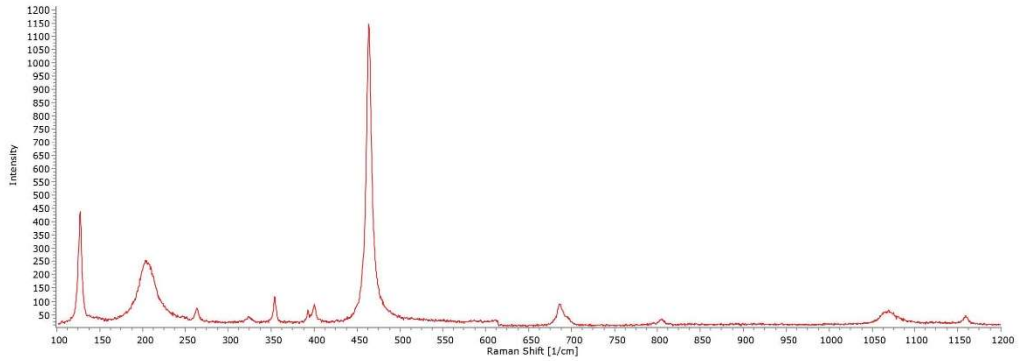

FN12491-quartz

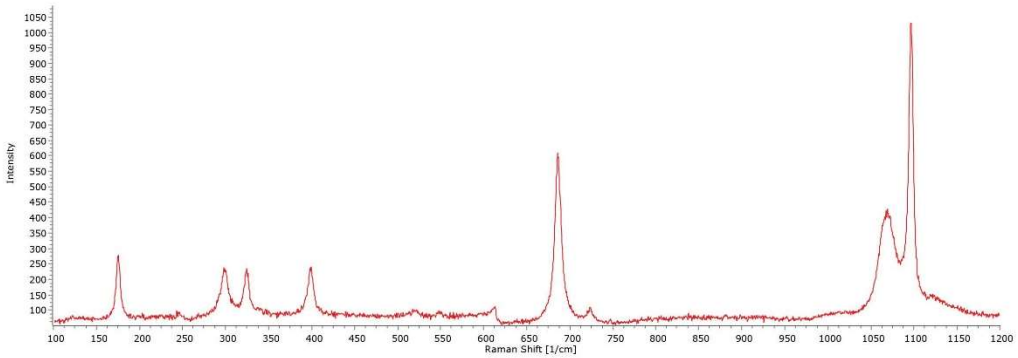

FN12969-dolomite

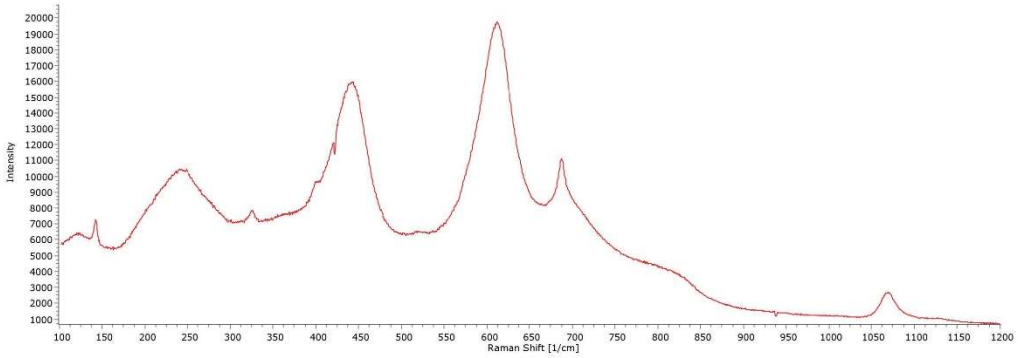

FN12969-rutile

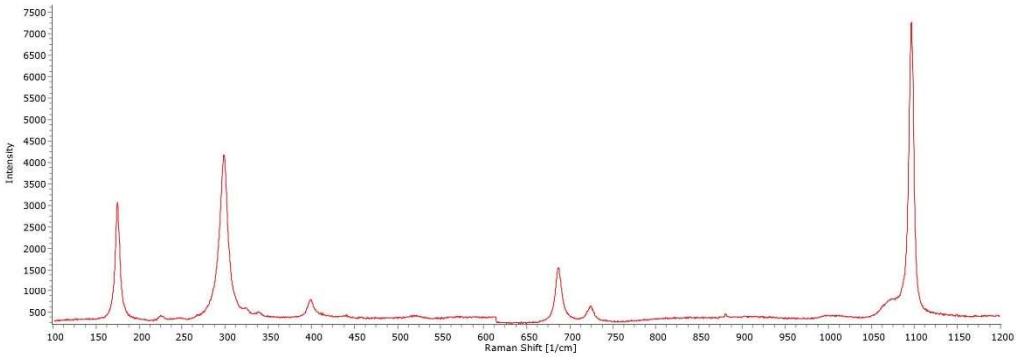

FN12970-dolomite

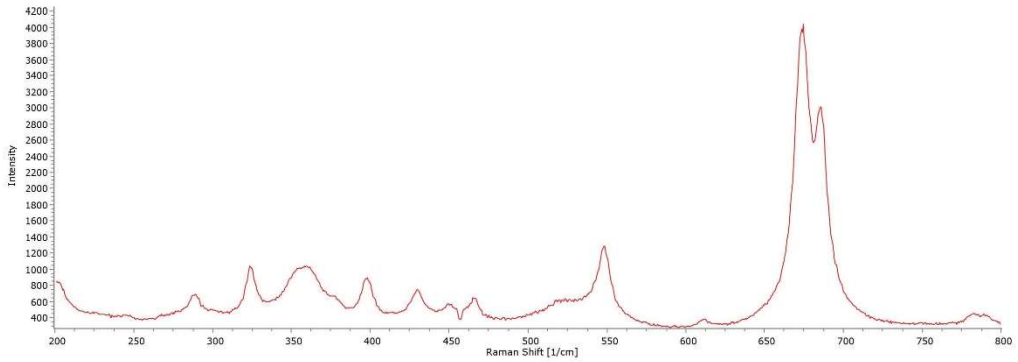

FN12970-phlogopite

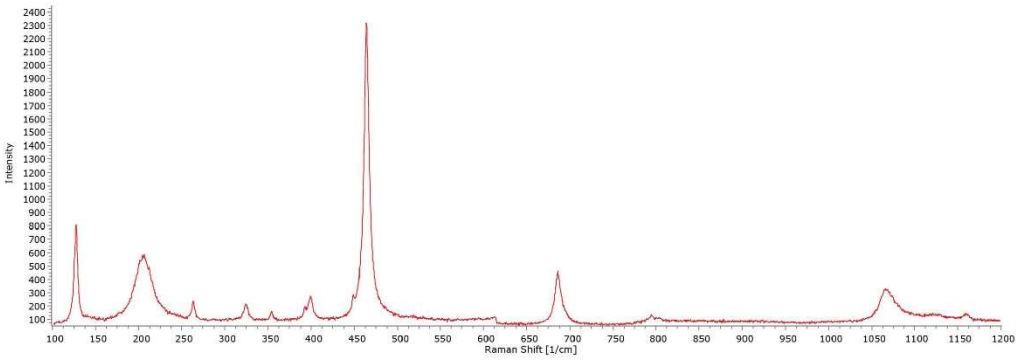

FN12971-quartz

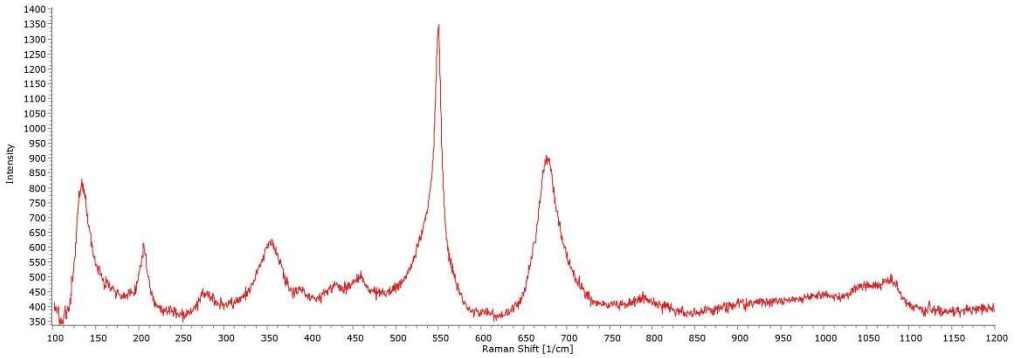

FN12972-Clinochlore

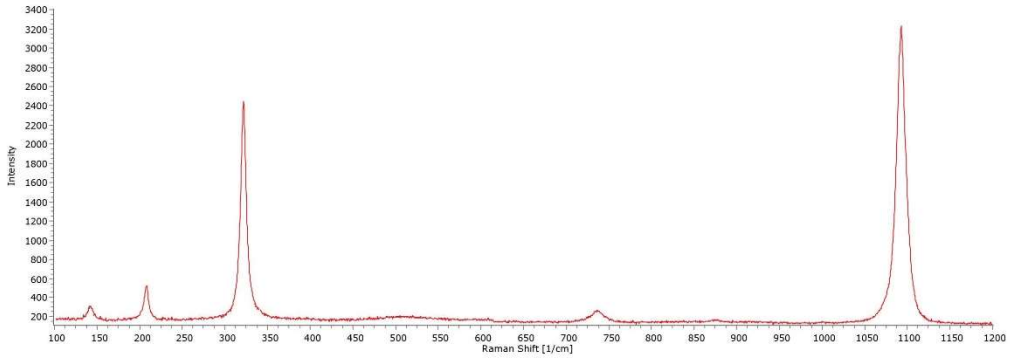

FN12972-magnesite

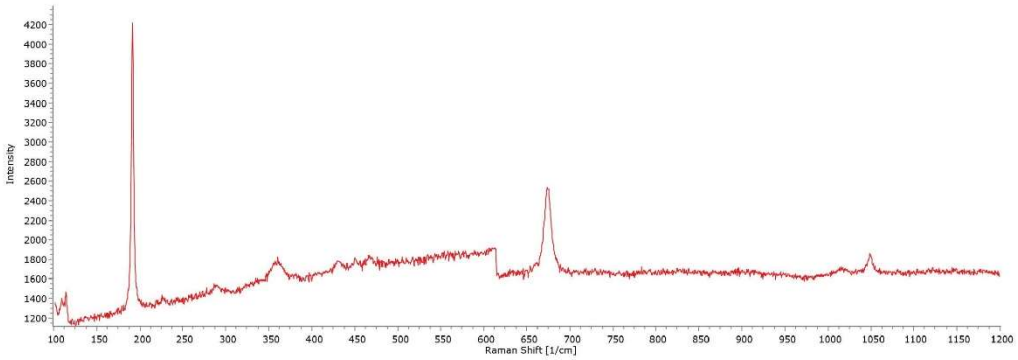

FN12972-talc

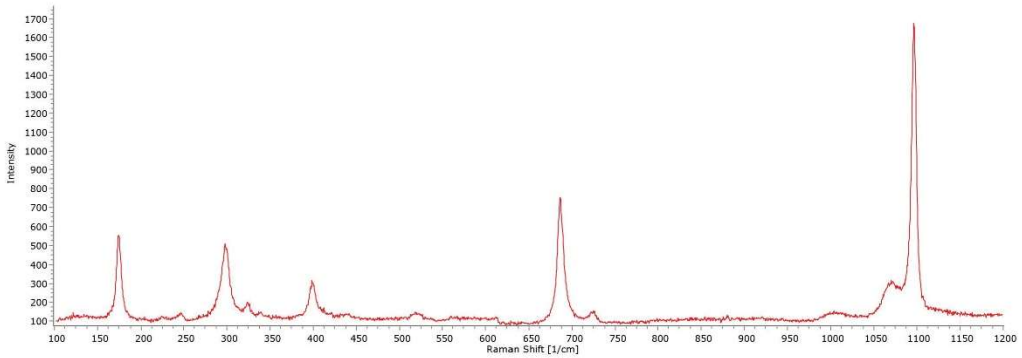

FN12973-dolomite

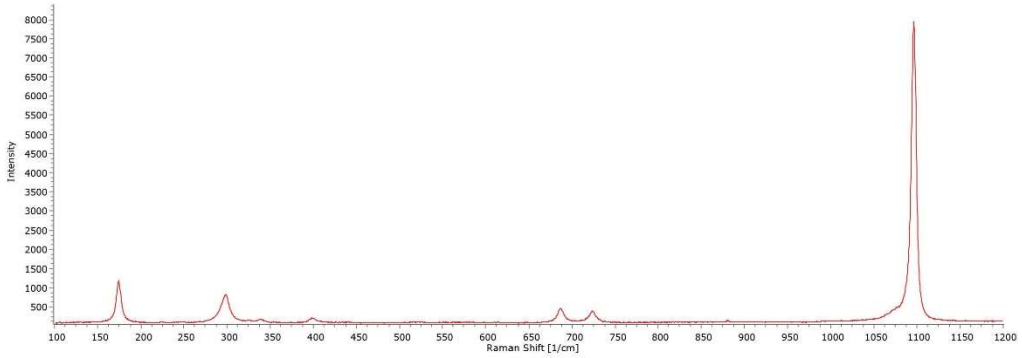

FN12973-dolomite-2

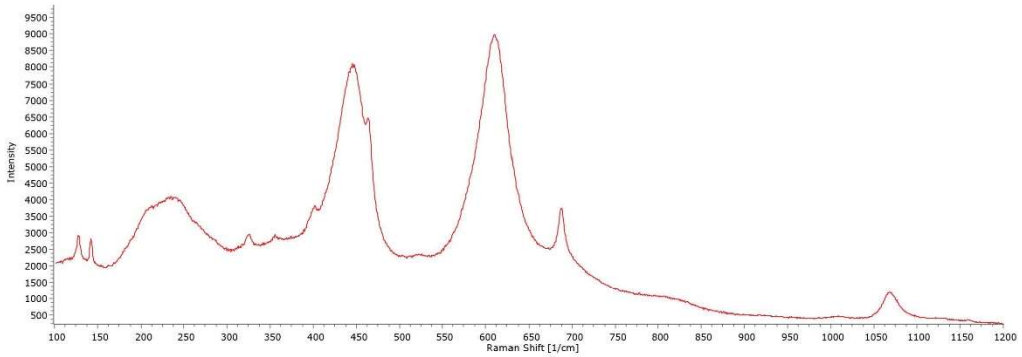

FN12973-rutile

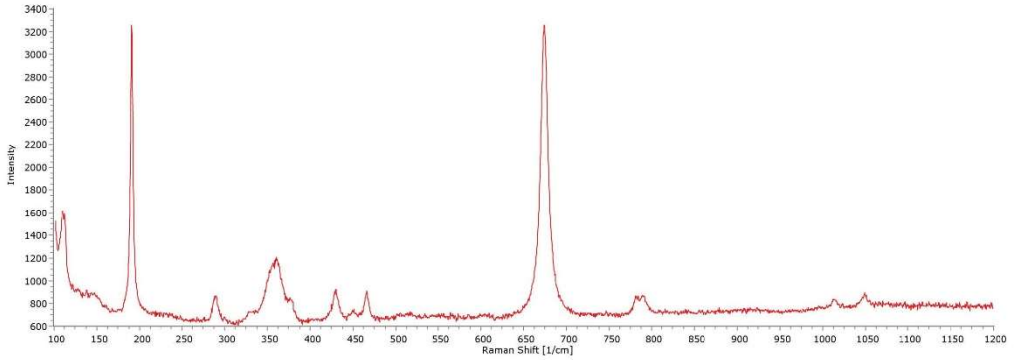

FN12973-talc

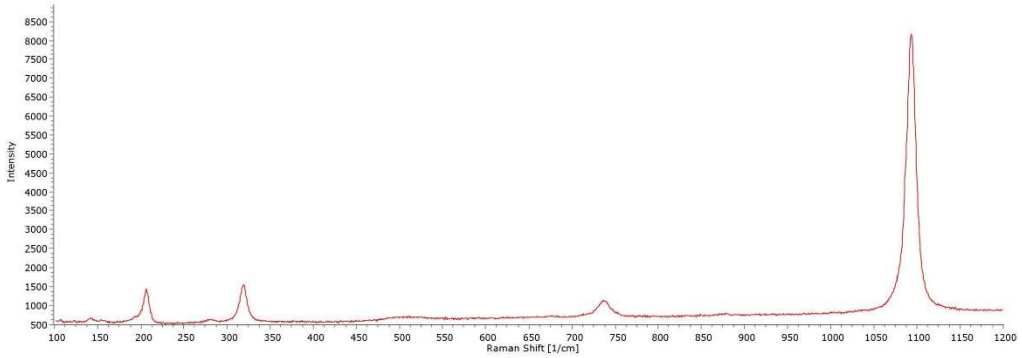

FN12974-magnesite

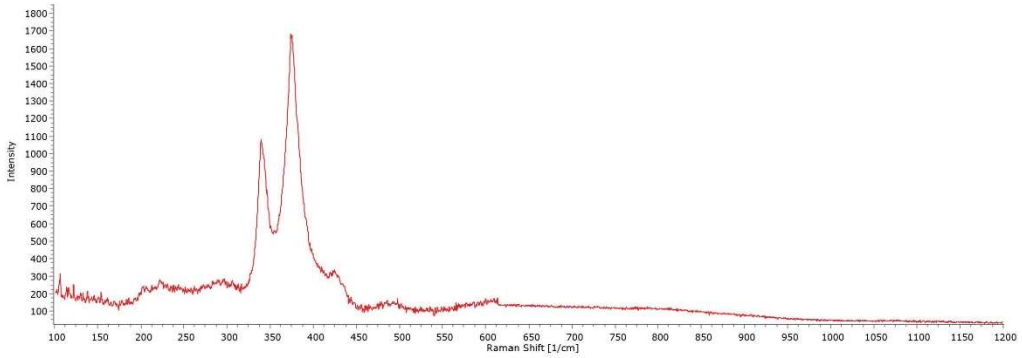

FN12975-(pyrrhotite)

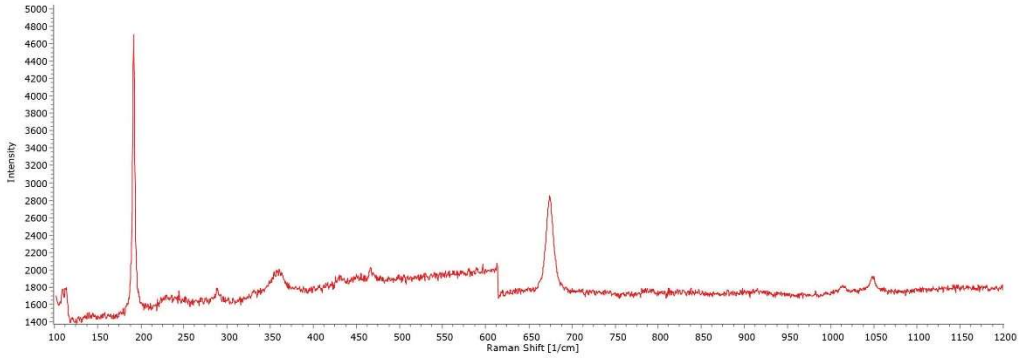

FN12976-talc

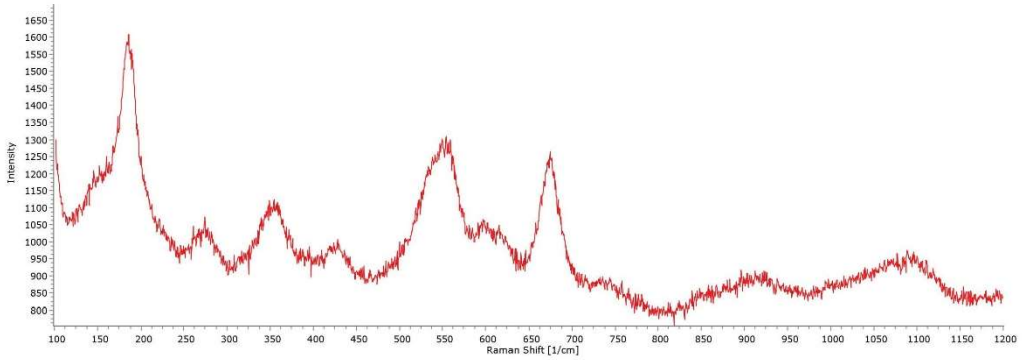

FN12977-vermiculite

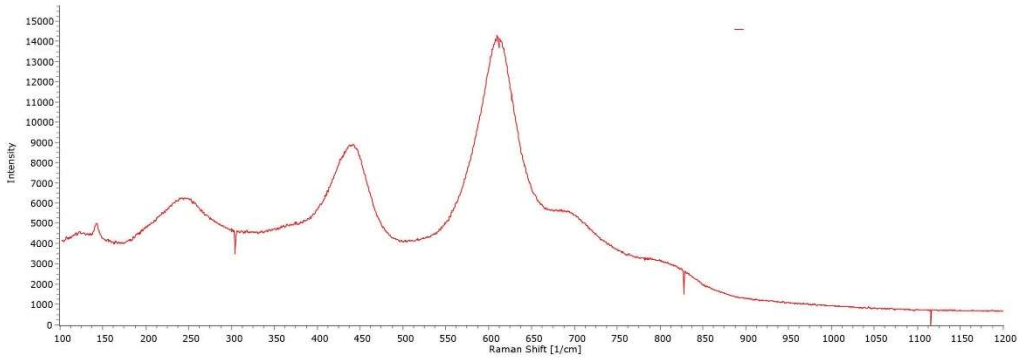

FN12979-rutile

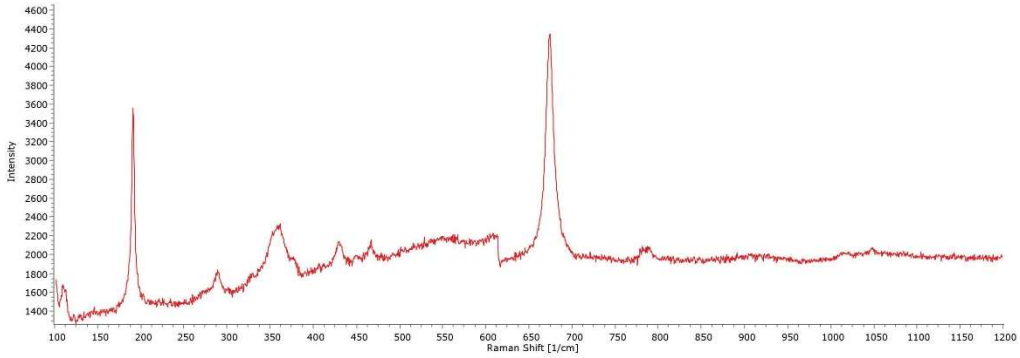

FN12980-talc

Annex IX: Supplementary pictures of the thin-sections

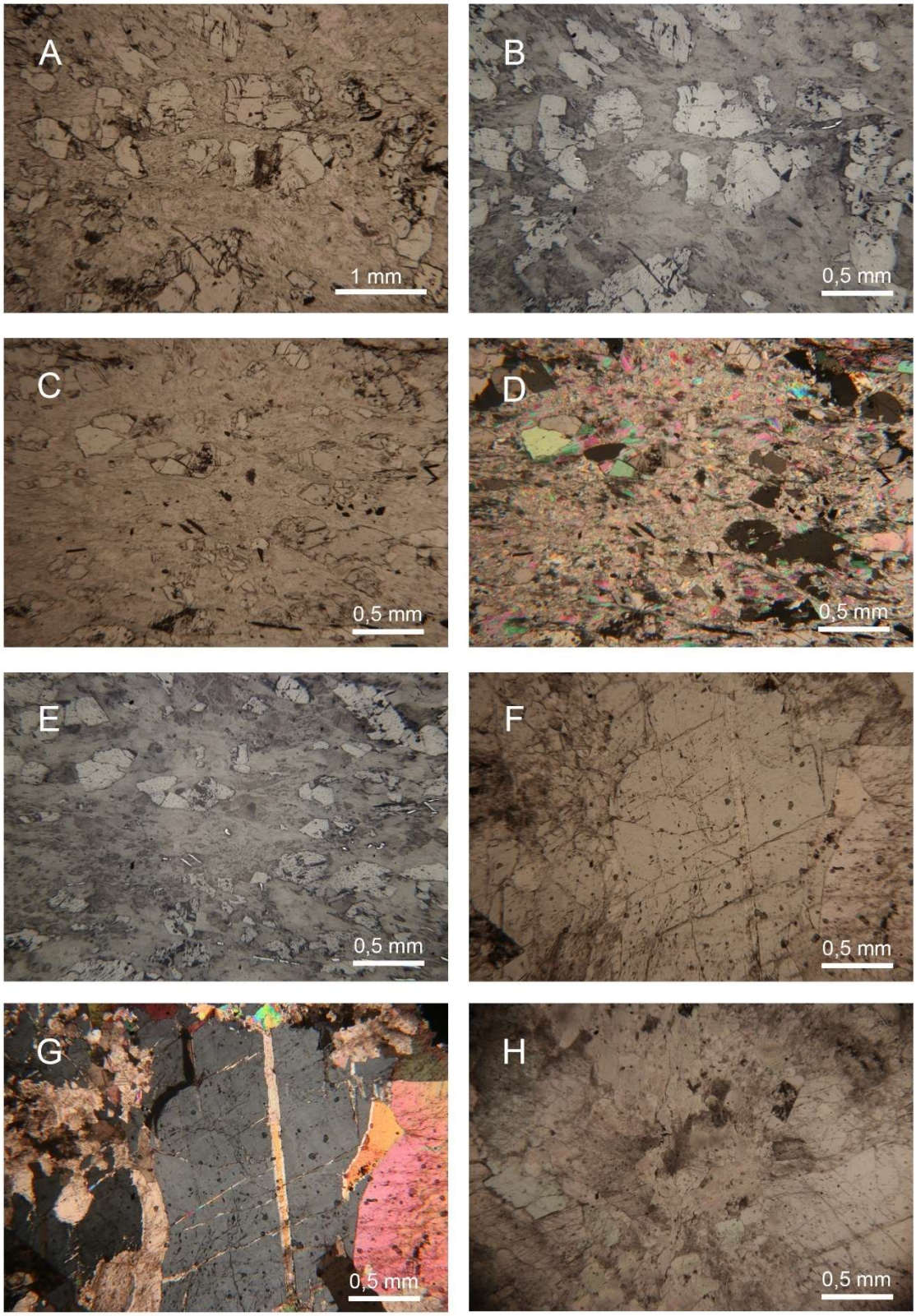

*Figure 39: **A** Unmineralized section of host rock; microboudin or isolated dolomite grains occur along schistosity planes in a fine interbedded magnesite-talc-muscovite matrix (LC-khalid-5, PPL). **B** Same section in reflected light (LC-khalid-5, RL). **C** Another view of the unmineralized section of host rock (LC-khalid-5, PPL). **D** Same view (LC-khalid-5, XPL). **E** Same view, note some elongated light-grey grains of chromites (following foliation S-planes?) (LC-khalid-5, RL). **F** A fractured emerald crystal (LC-khalid-6, PPL). **G** A fractured emerald crystal with intrusive magnesite along cleavage planes and fractures (LC-khalid-6, XPL). **H** General view (LC-khalid-6, PPL).*

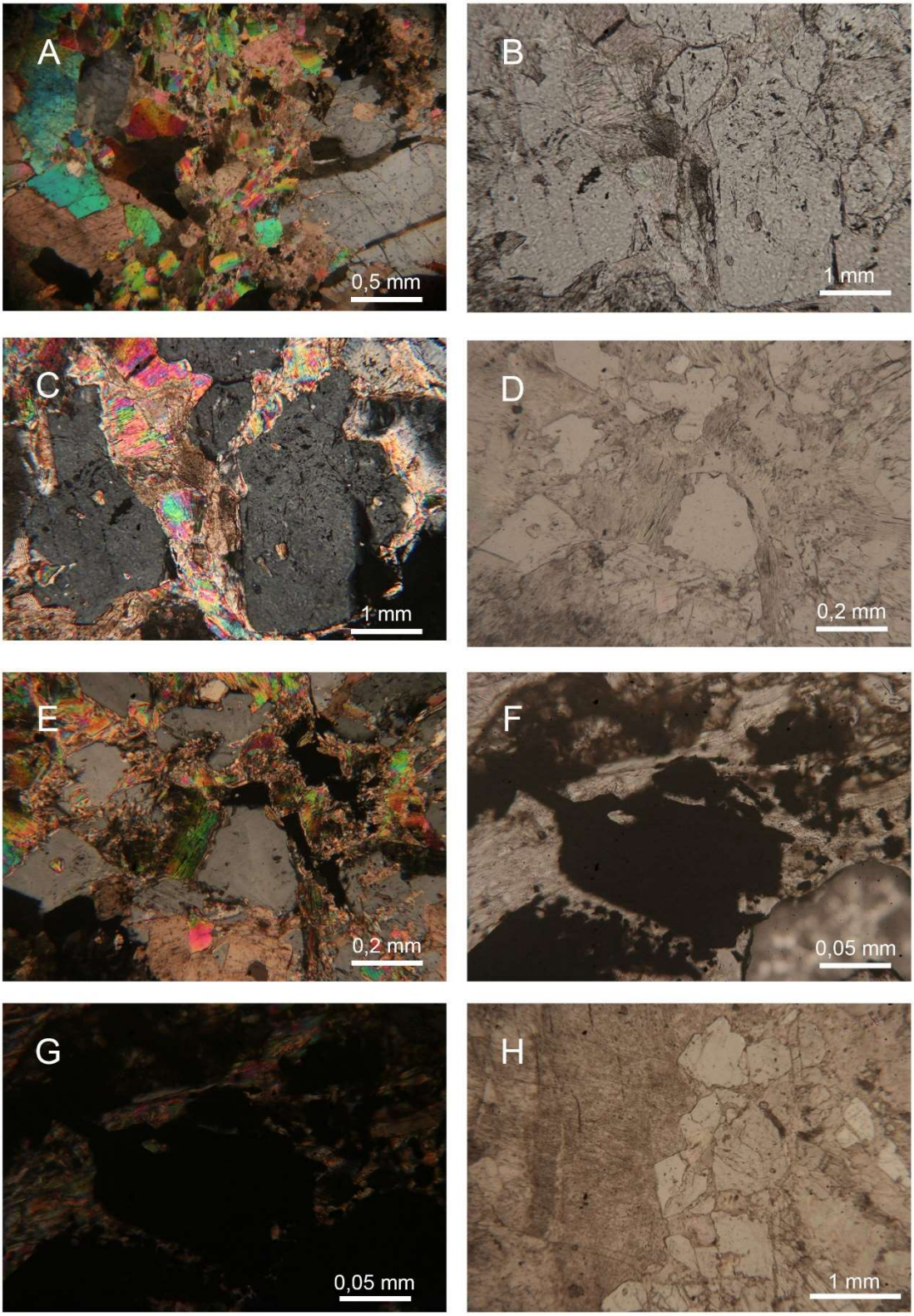

*Figure 40: **A** General view (LC-khalid-6, XPL). **B** Diverse emerald crystals with inclusions in tlc-mag matrix (LC-khalid-6, PPL). **C** Same emerald crystals with some visible micas inclusions (LC-khalid-6, XPL). **D** (Micaceous)-tlc matrix enclosing emerald crystals (LC-khalid-6, PPL). **E** Same view in crossed polar (LC-khalid-6, XPL). **F** A chromite grain disseminated in the magnesite-talc (LC-khalid-6, PPL). **G** Same grain (LC-khalid-6, XPL). **H** The emerald mineralization in a fine magnesite-talc-muscovite matrix, at the interface with the large grained magnesite (LC-khalid-8, PPL).*

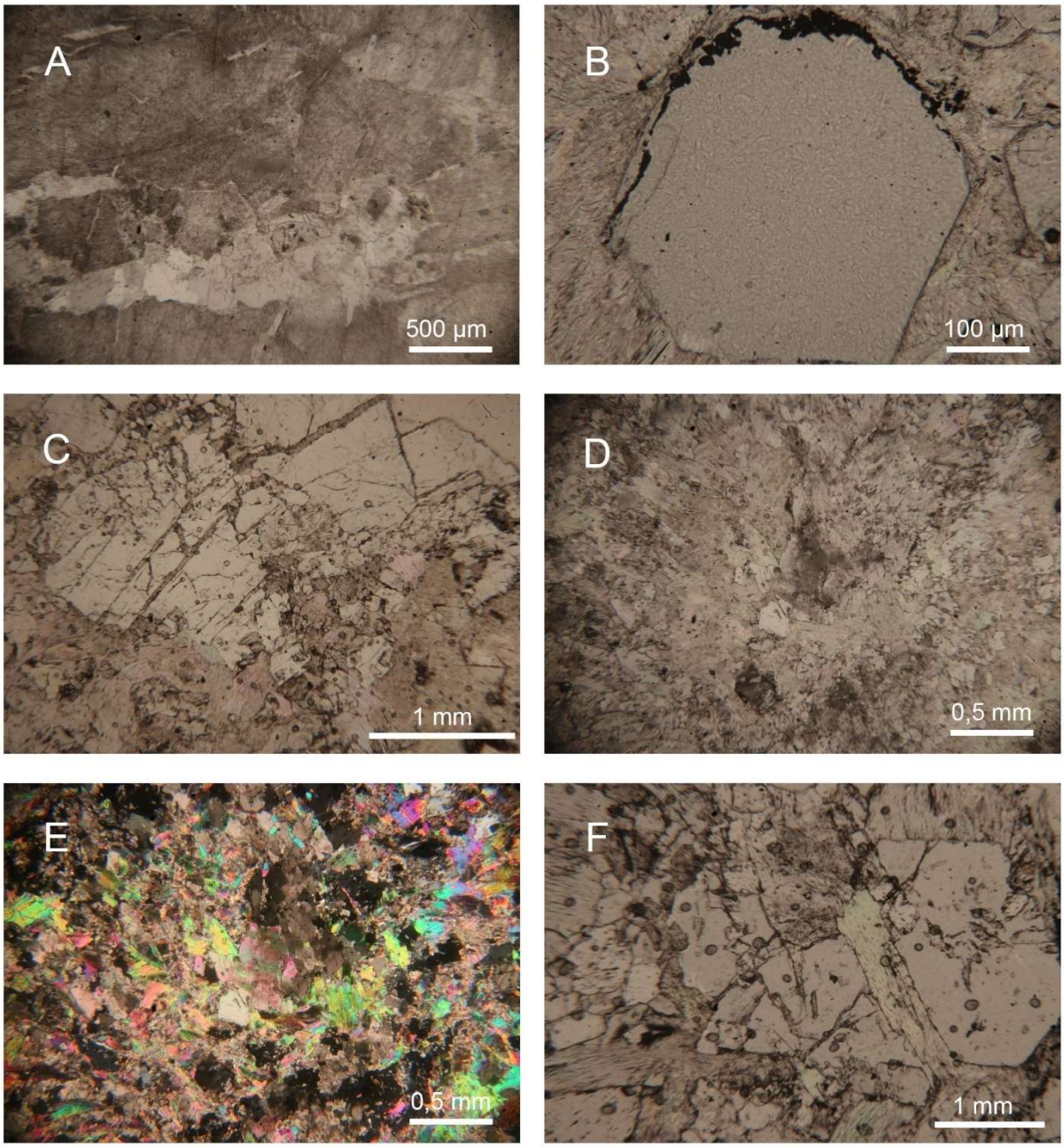

Figure 41: A emerald-quartz-muscovite veinlets cross-cutting the large-grained magnesite domain (LC-khalid-8, PPL). B A basal section of emerald in the fine magnesite-talc matrix. The black pinpoints inclusions on the rims of the emerald are oxides (LC-khalid-8, PPL). C Fractured emeralds along cleavage planes pervaded by fine magnesite, within a magnesite-talc-muscovite-dolomite matrix (LC-khalid-9, PPL). D General view (LC-khalid-9, PPL). E Same general view (LC-khalid-9, XPL). F An emerald crystal replaced by muscovite-magnesite (LC-khalid-9, PPL).

Annex X: ED-XRD analyses on emerald sample

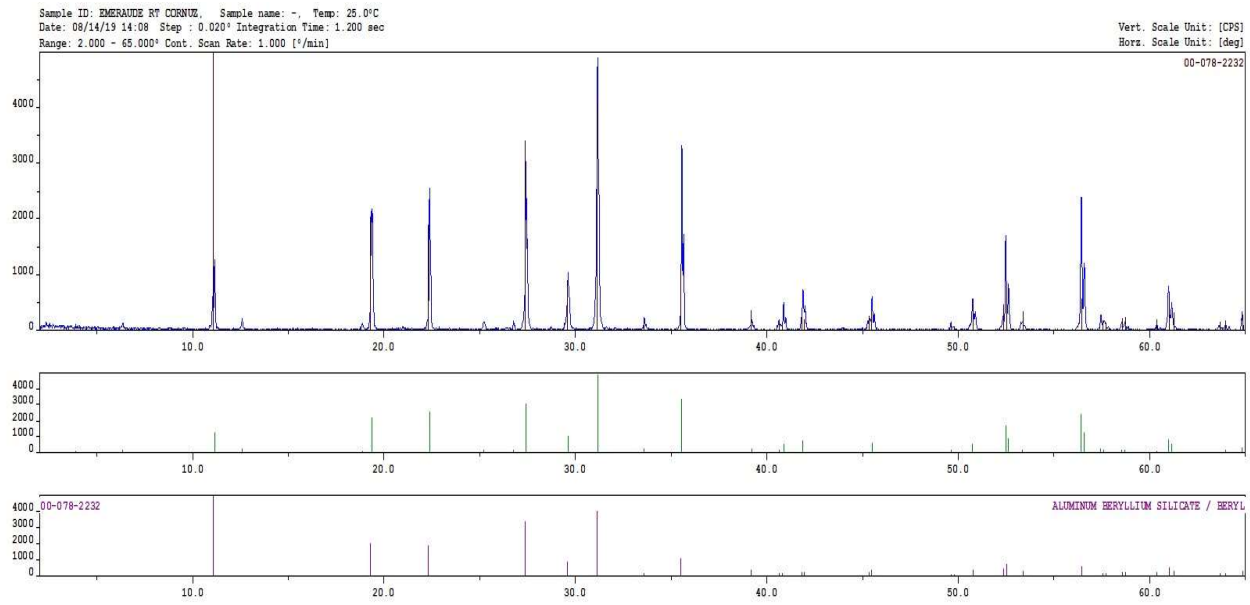

Figure 42: ED-XRD pattern on FN12970 fine-crushed powder. Note the major diffraction peaks of emerald and only few smaller peaks indicate the presence of chlorite group minerals.

Annex XI: ED-XRD analyses on rock sample

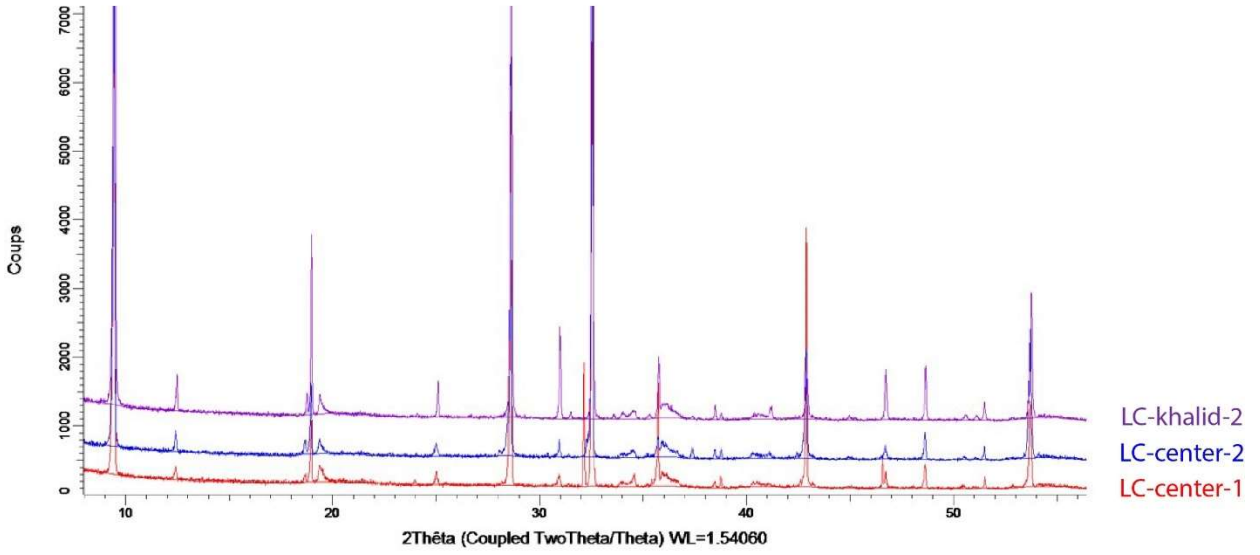

Figure 43: ED-XRD pattern for 3 powders of fault breccias selected out the rock sampling batch.

Annex XII: Selection of representative EDX-SEM analyses on emerald samples

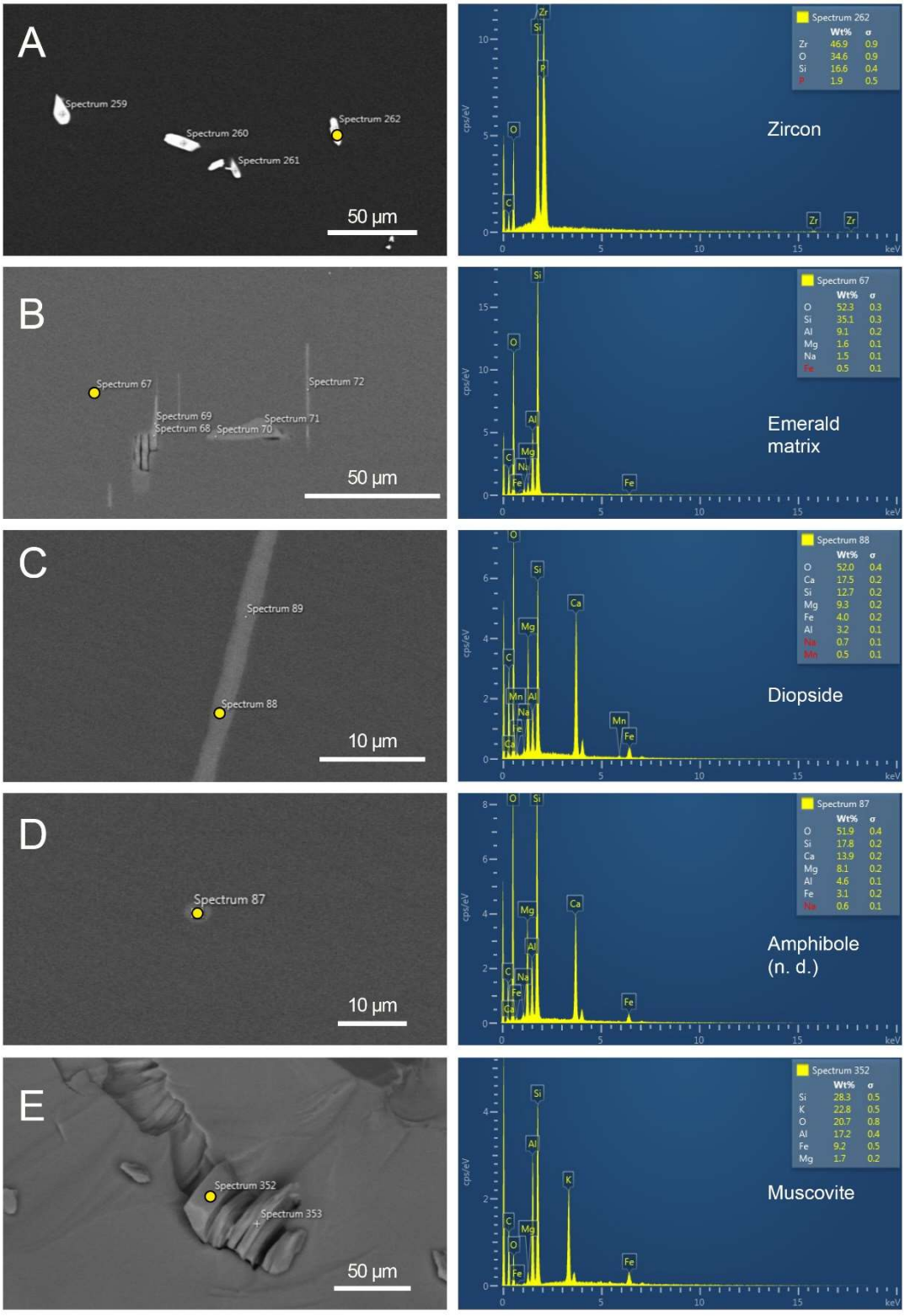

Figure 44: BSE pictures and compositions of inclusions in emerald samples. ***A*** *Zircon grains on a crystal face with minor micro-inclusions of xenotime/apatite, due to minor phosphorus content (FN12969, BSE, polished).* ***B*** *An analysis's point in emerald matrix (FN12974, BSE, polished).* ***C*** *A side-view of flat sheet of diopside (FN12974, BSE, polished).* ***D*** *A perpendicular cut rod of undefined amphibole (omphacite-jadeite, clinopyroxene, tschermakite) (FN12974, BSE, polished).* ***E*** *Muscovite forming as columnar crystals (FN12970, BSE, crushed).*

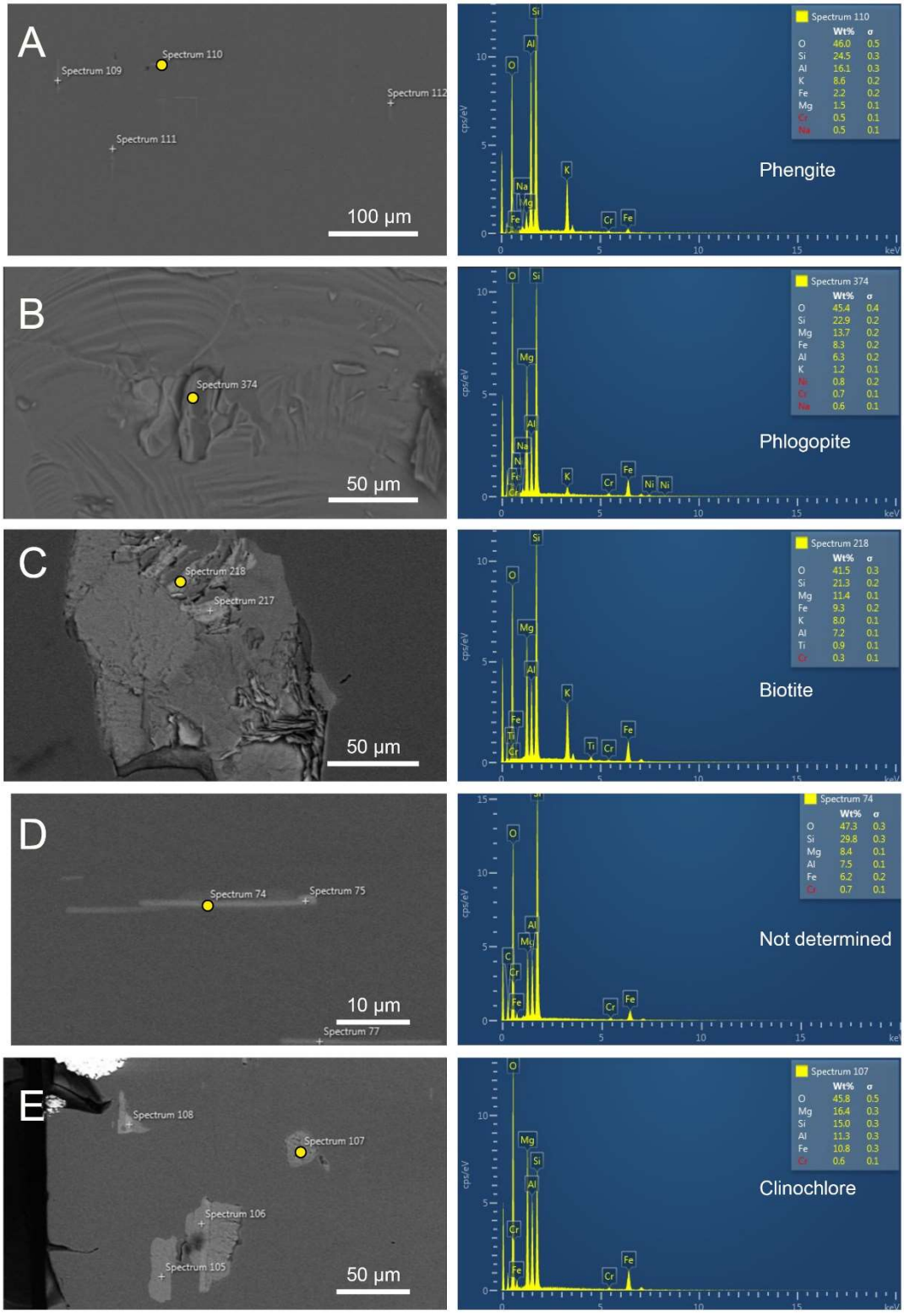

*Figure 45: BSE pictures and compositions of inclusions in emerald samples. **A** Small perpendicular intersecting sheets of phengite (FN12974, BSE, polished). **B** Phlogopite occurring as thin stacked platelets (FN12970, BSE, crushed). **C** Soft biotite piles with titanium traces scratched away during polishing (FN12969, BSE, polished). **D** Undefined thin sheets of a mineral in composition between phyllosilicates and amphiboles (FN12974, BSE, polished). **E** Near the crystal face, (Cr-)clinochlore inclusions occurring with phlogopite (FN12974, BSE, polished).*

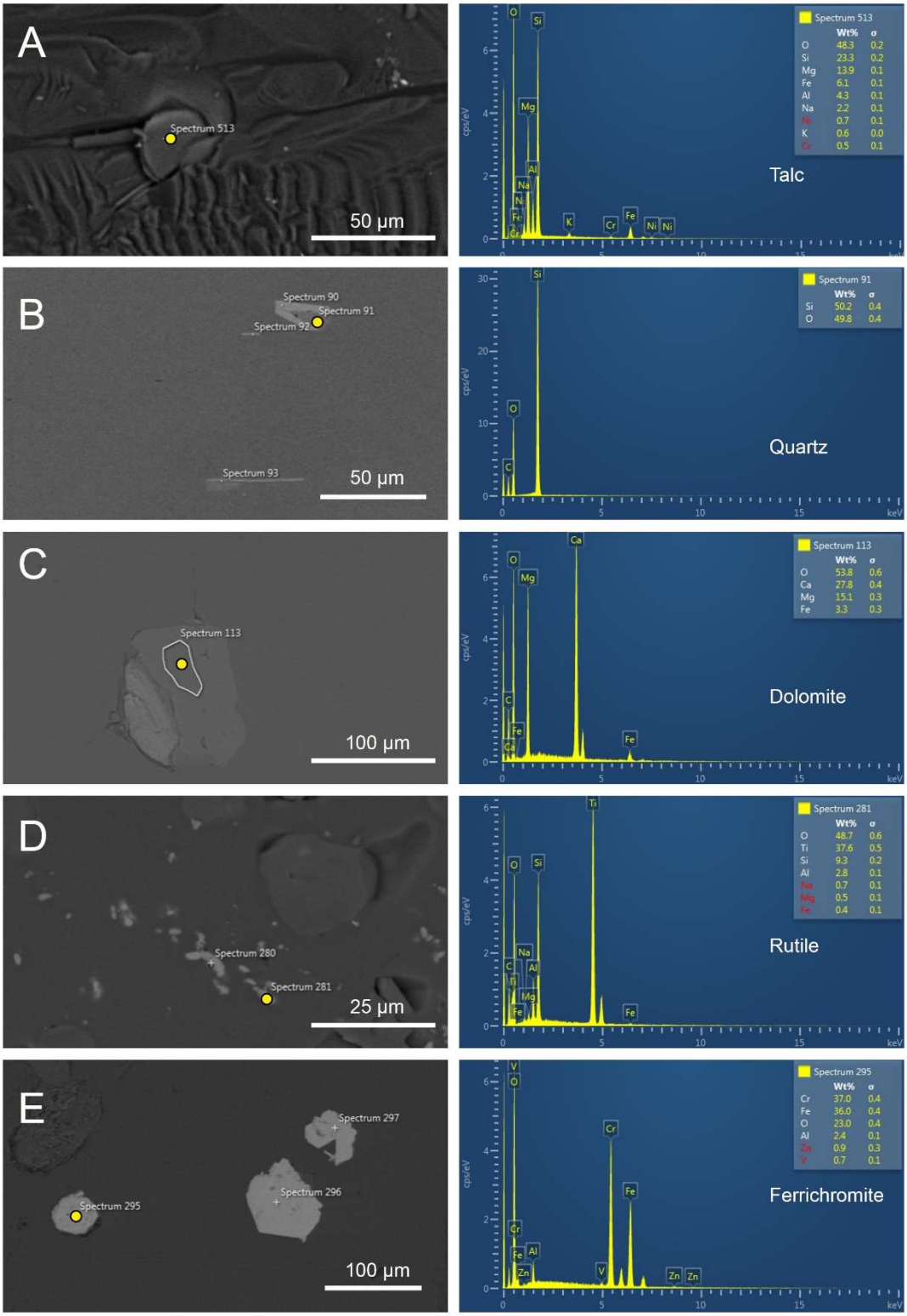

*Figure 46: BSE pictures and compositions of inclusions in emerald samples. **A** Grain of talc as inclusion, with nickel traces (FN12970, BSE, crushed). **B** A quartz intergrowth with two muscovite platelets (FN12974, BSE, polished). **C** Dolomite crystal with minor siderite content (FN12974, BSE, polished). **D** Rutile grains on a crystal face (FN12973, BSE, polished). **E** (V-Zn)-ferrichromite flakes (FN12976, BSE, polished).*

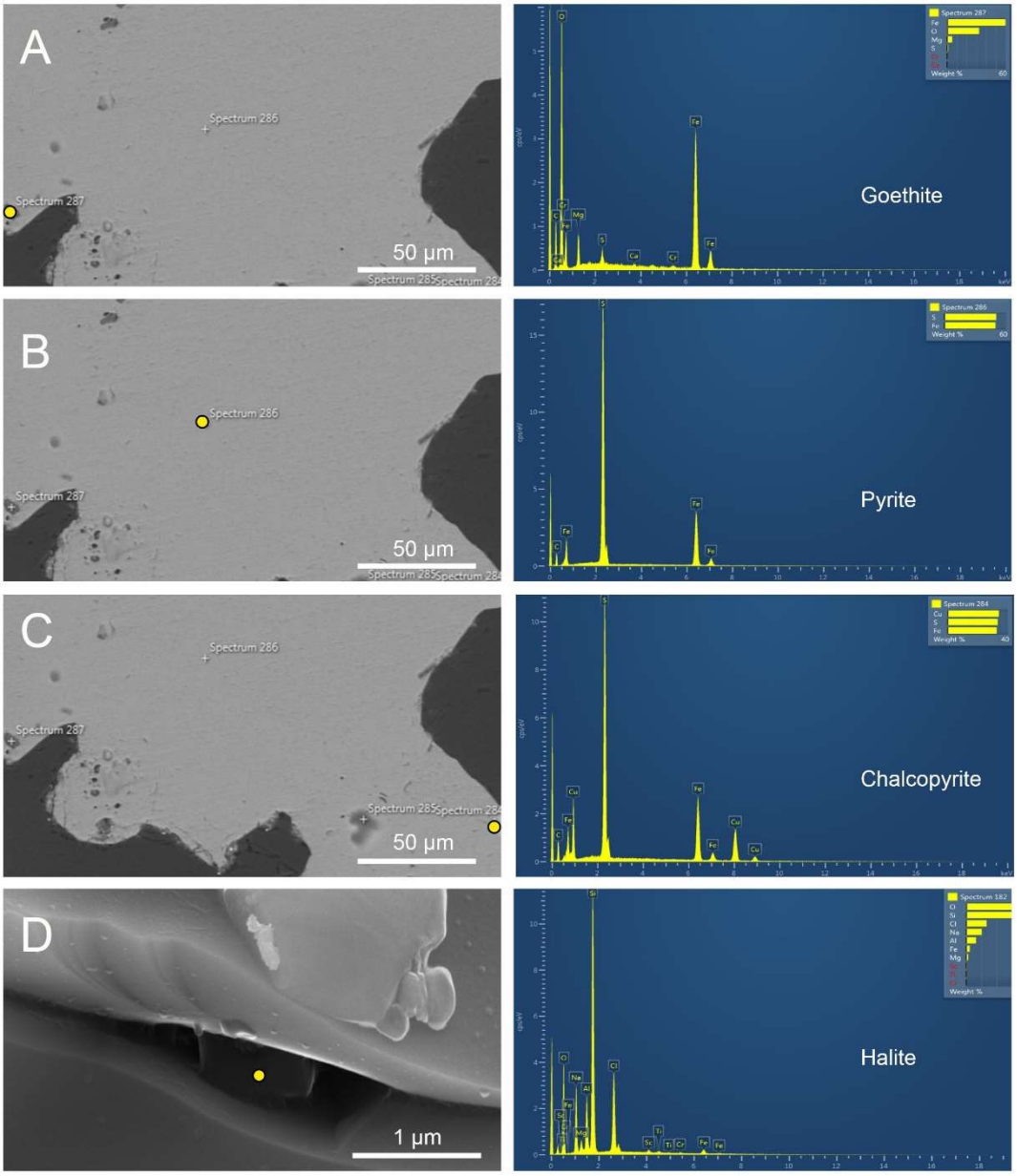

Figure 47: BSE pictures and compositions of inclusions in emerald samples. ***A*** *A grain of goethite trapped in the middle of a large pyrite grain (FN12975, BSE, polished).* ***B*** *A large pyrite grain (FN12975, BSE, polished).* ***C*** *Chalcopyrite replacing the pyrite grain (FN12975, BSE, polished).* ***D*** *Cubic halite crystal still trapped in an empty multi-phase fluid inclusion (FN12970, SE, crushed).*

Annex XIII: BSE pictures of the EDX-SEM analyses for the emeralds samples

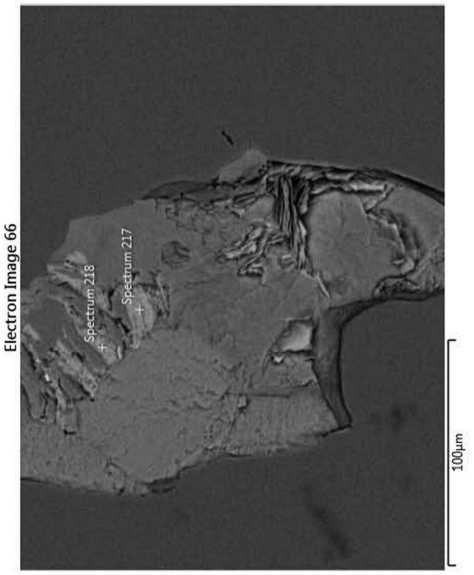

FN12969-2

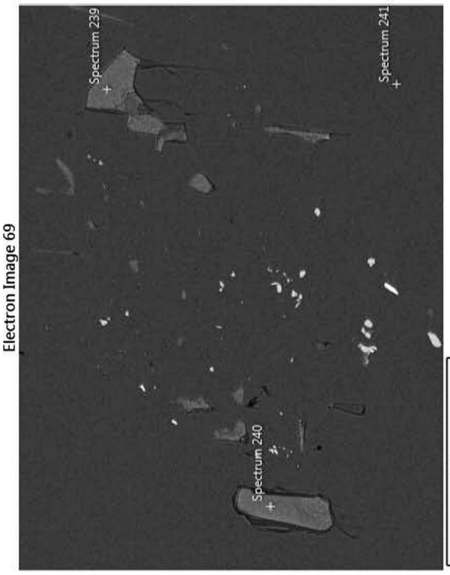

FN12969-4

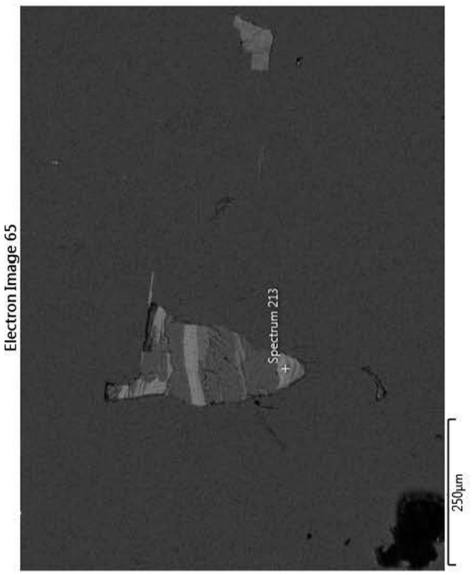

FN12969-1

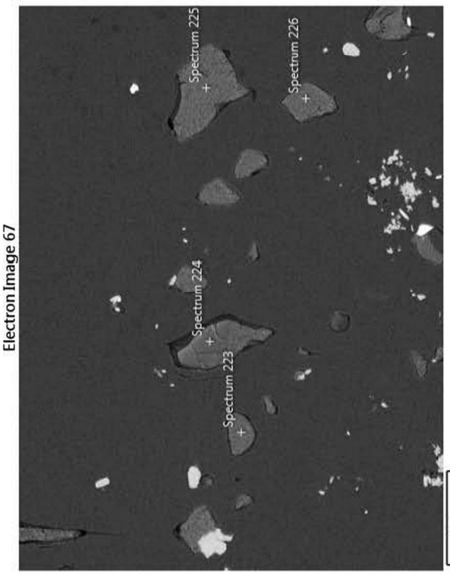

FN12969-3

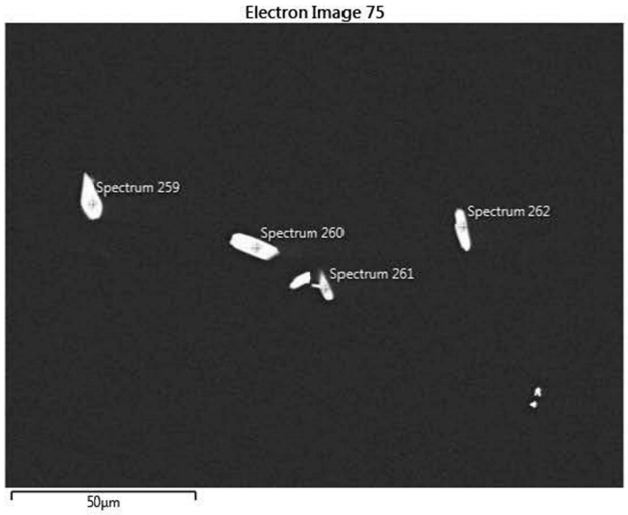

FN12969-6

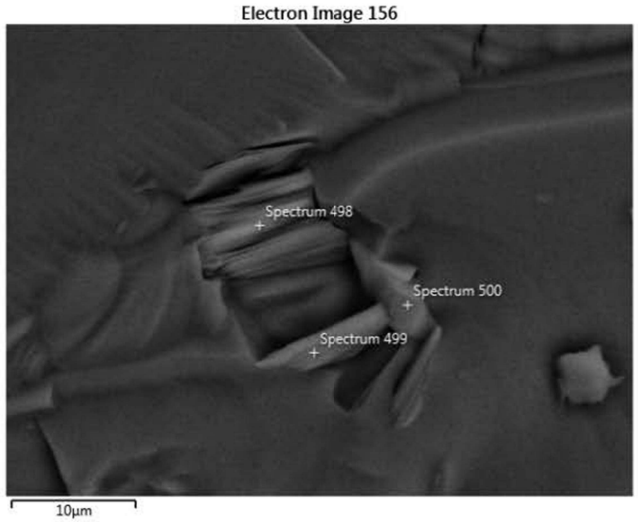

FN12970-1bis

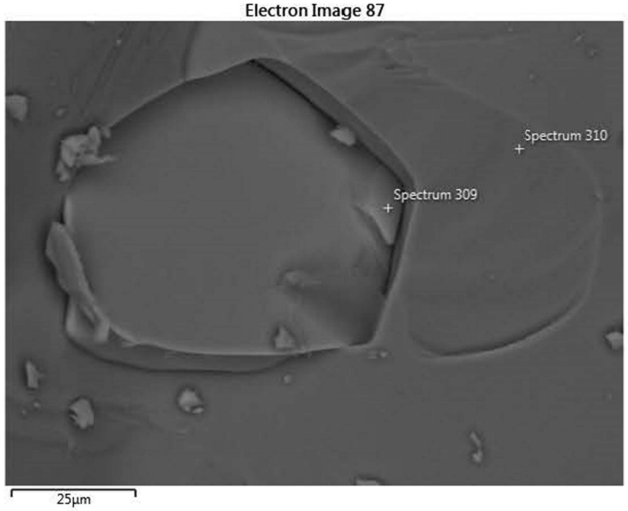

FN12970-2

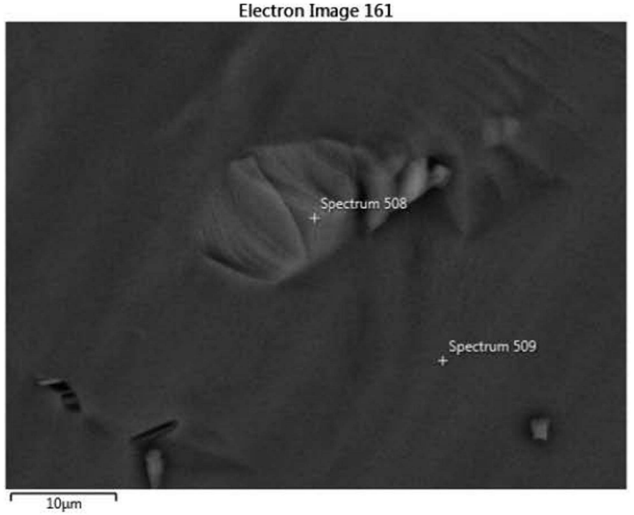

FN12970-2bis

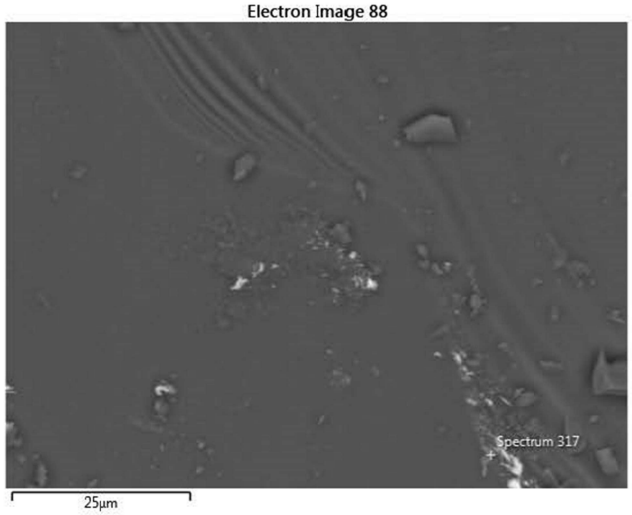

FN12970-3

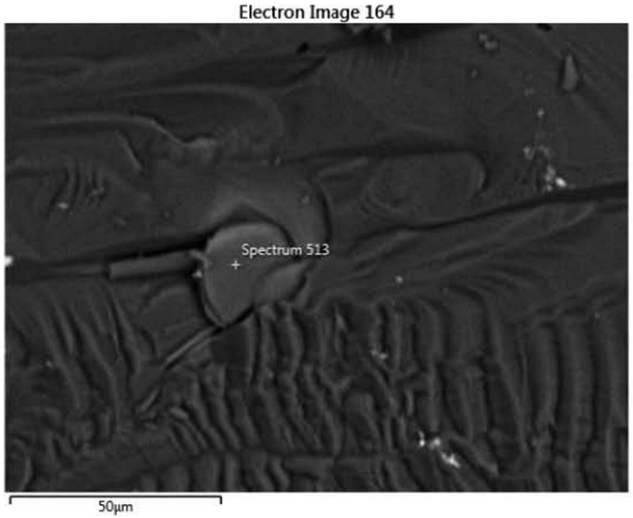

FN12970-3bis

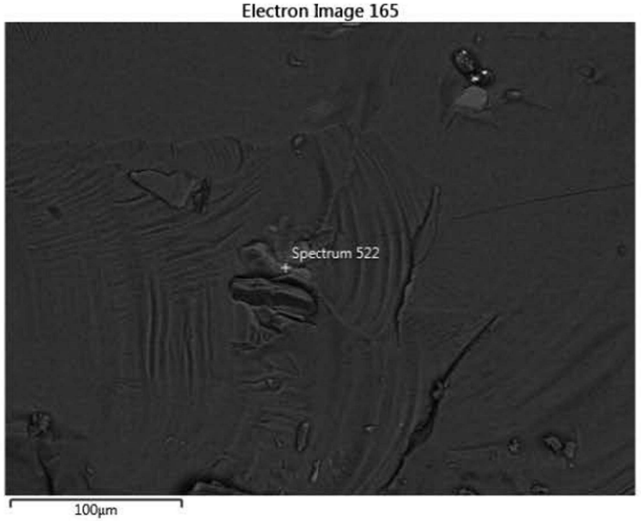

FN12970-4bis

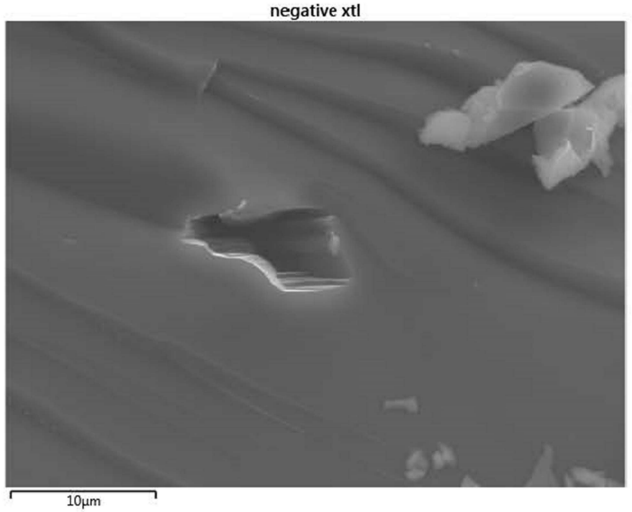

FN12970-5

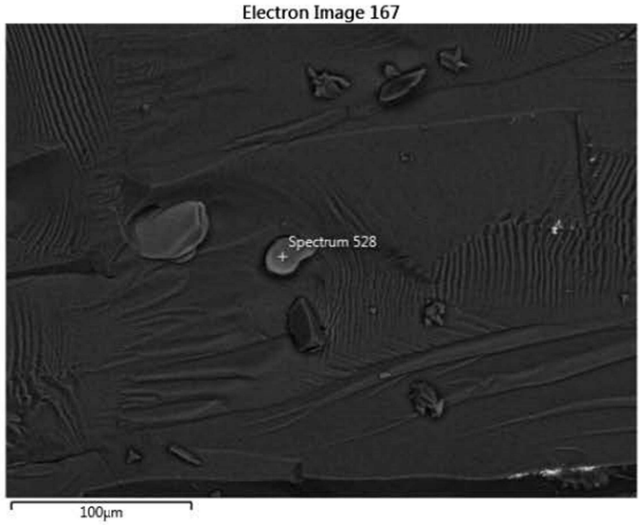

FN12970-5bis

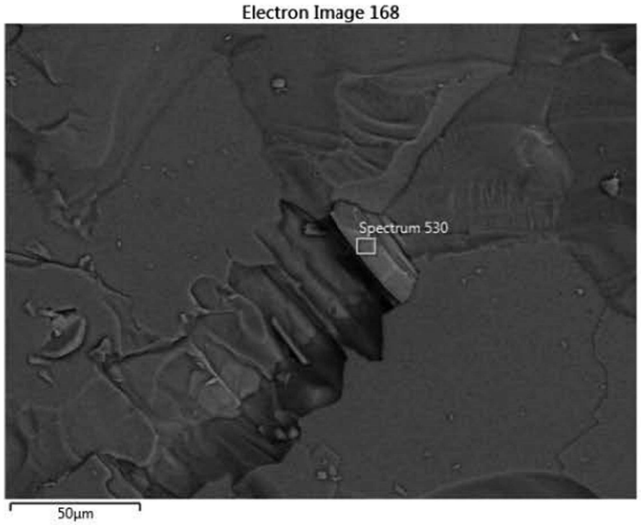

FN12970-6bis

FN12970-7bis

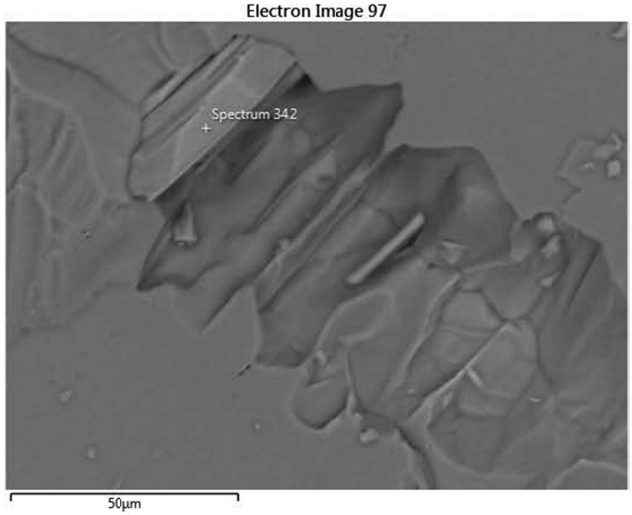

FN12970-8

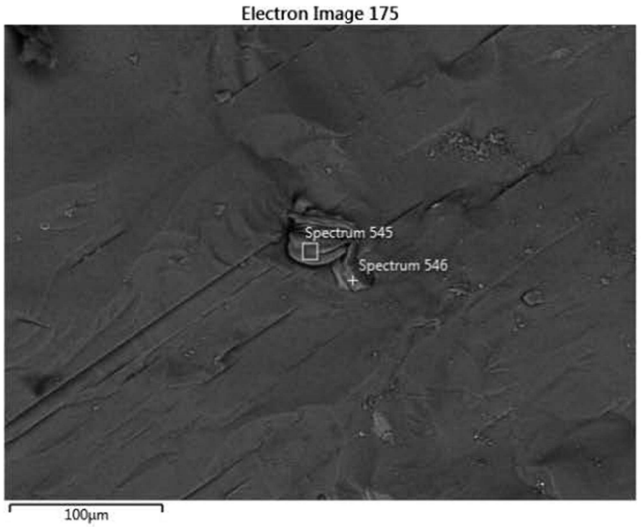

FN12970-8bis

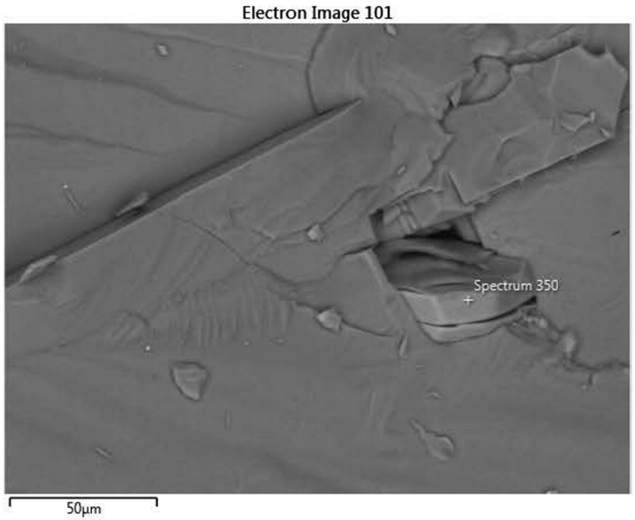

FN12970-9

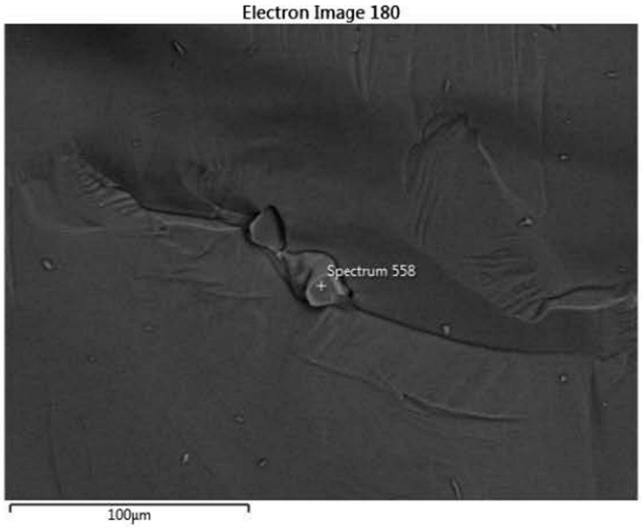

FN12970-9bis

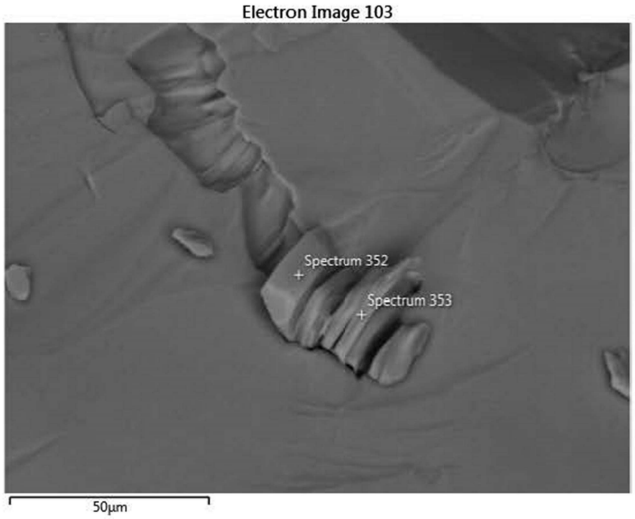

FN12970-10

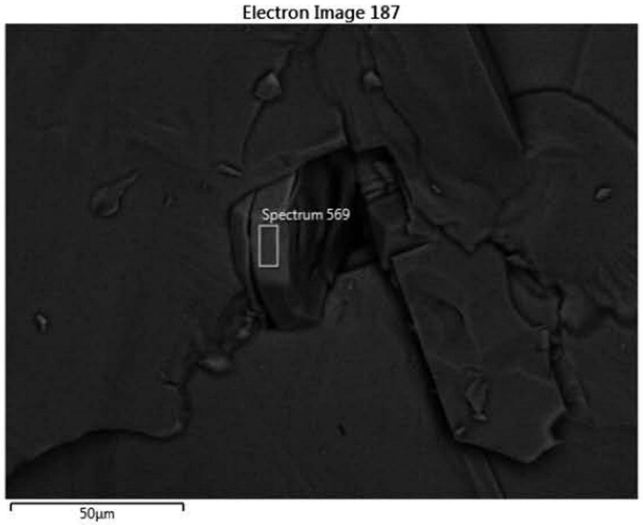

FN12970-10bis

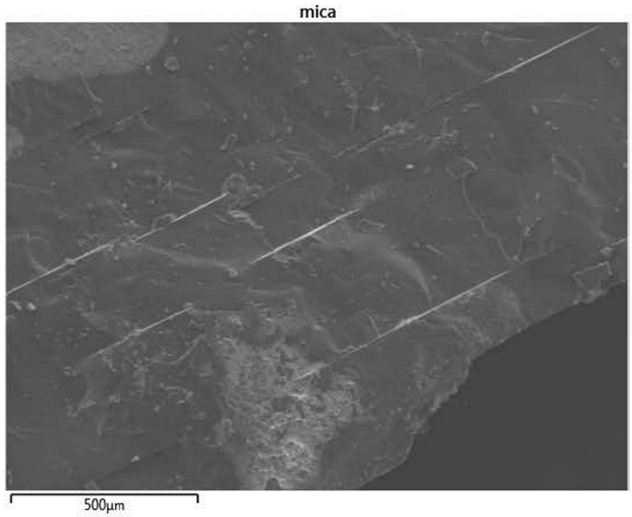

FN12970-11

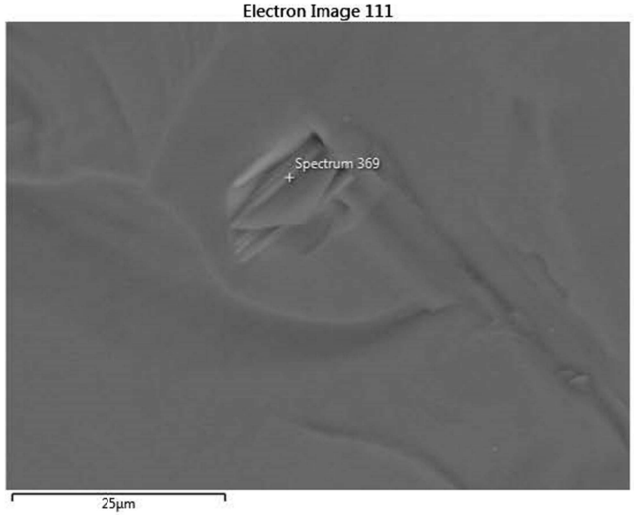

FN12970-13

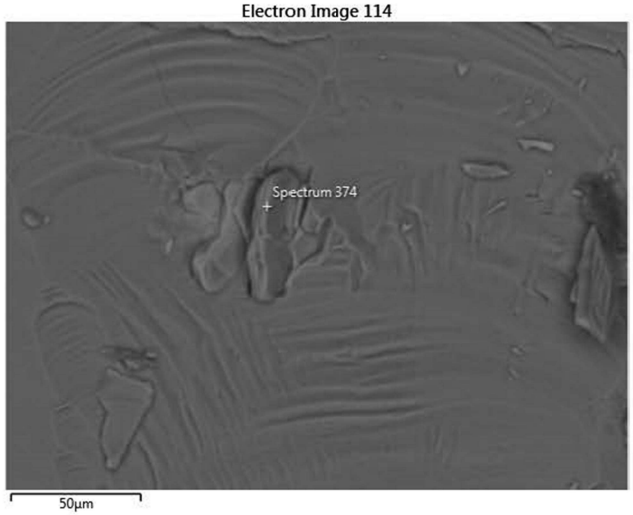

FN12970-14

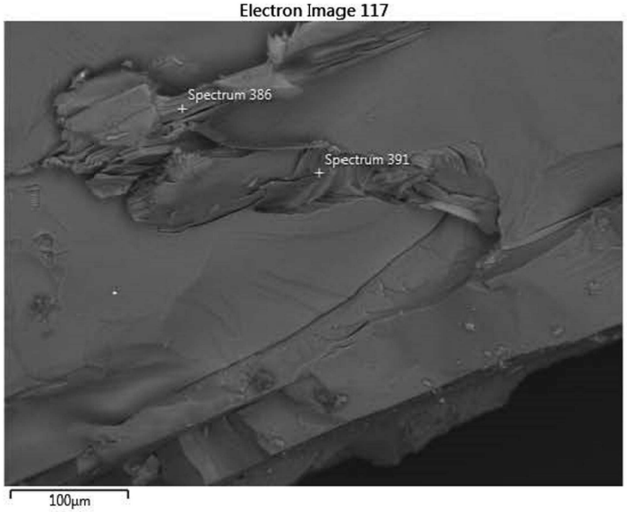

FN12970-16

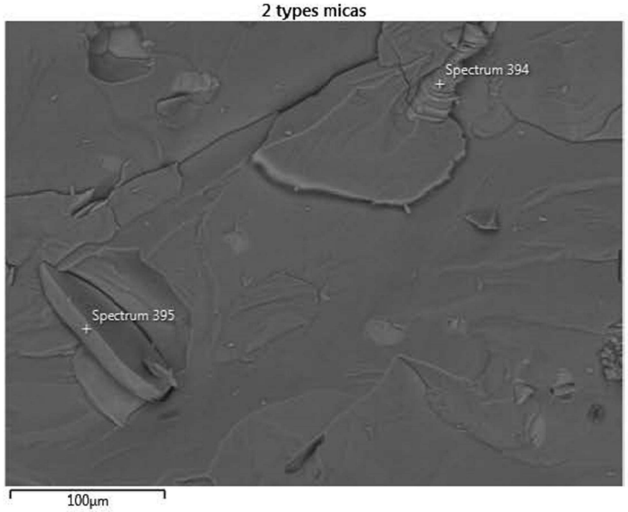

FN12970-17

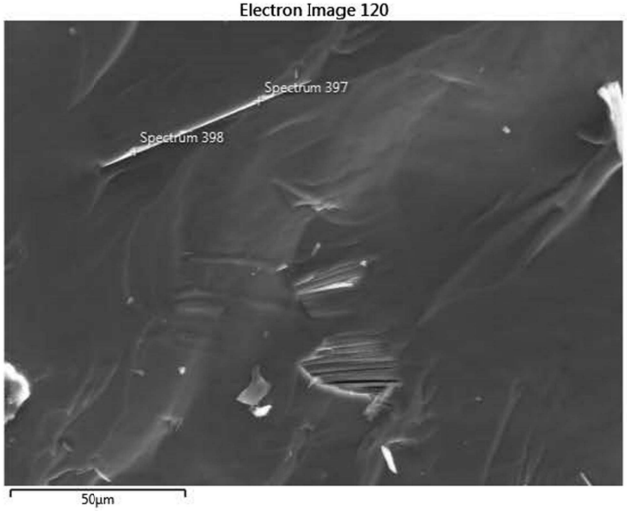

FN12970-18

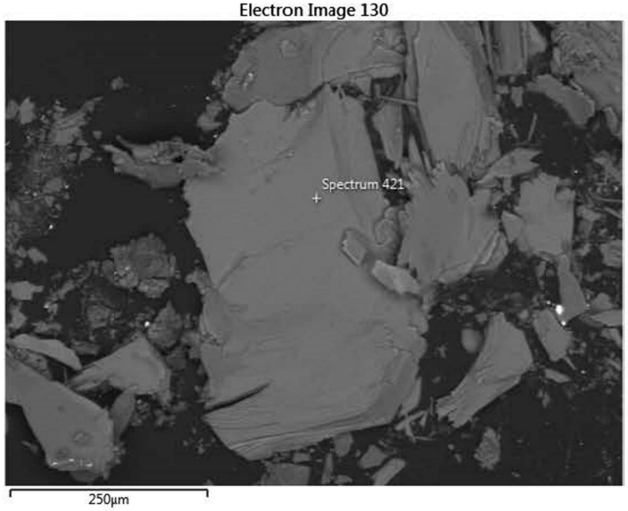

FN12970-19

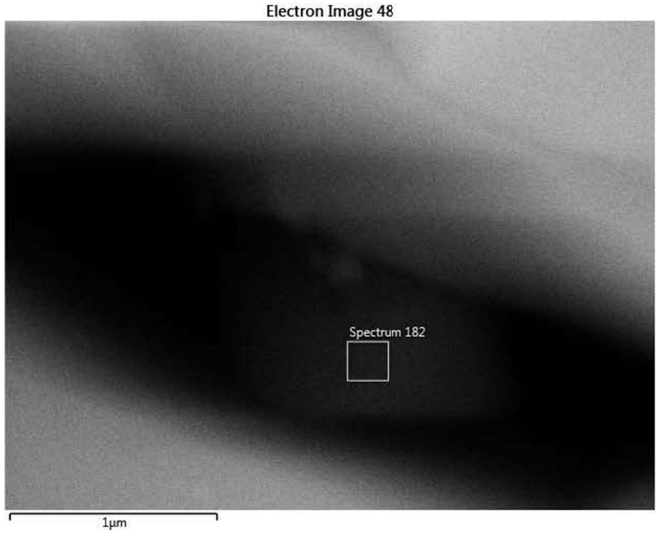

FN12970-20

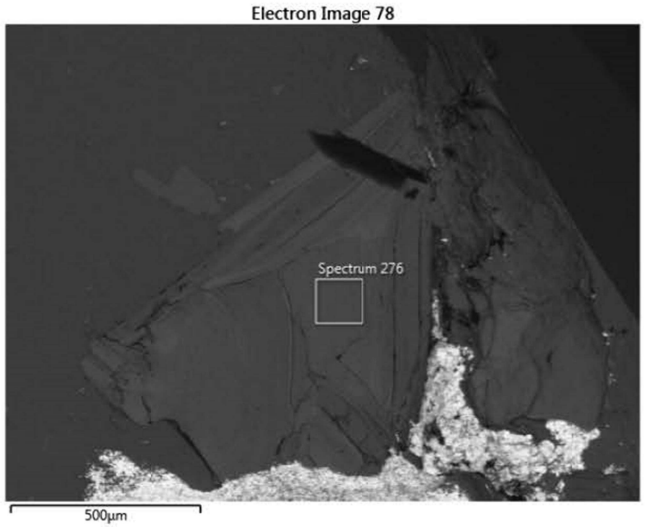

FN12973-1

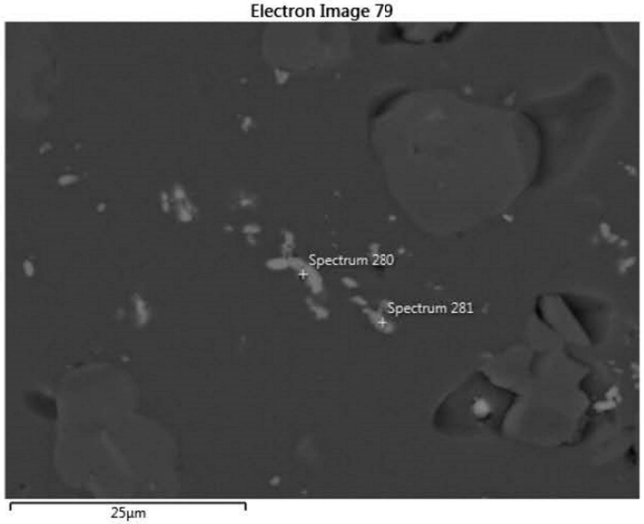

FN12973-2

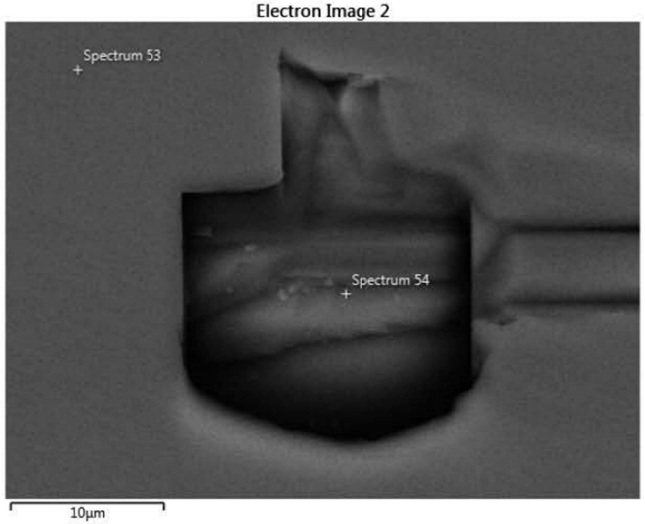

FN12974-1

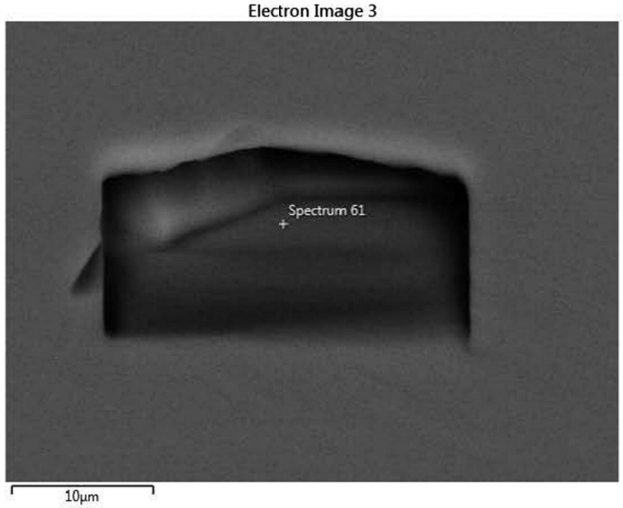

FN12974-2

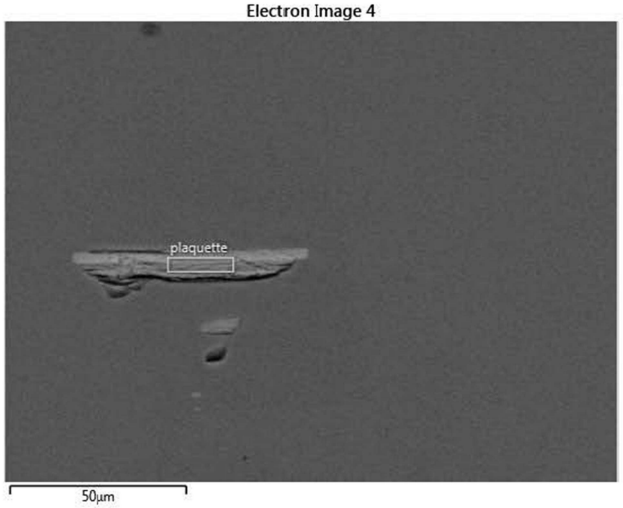

FN12974-3

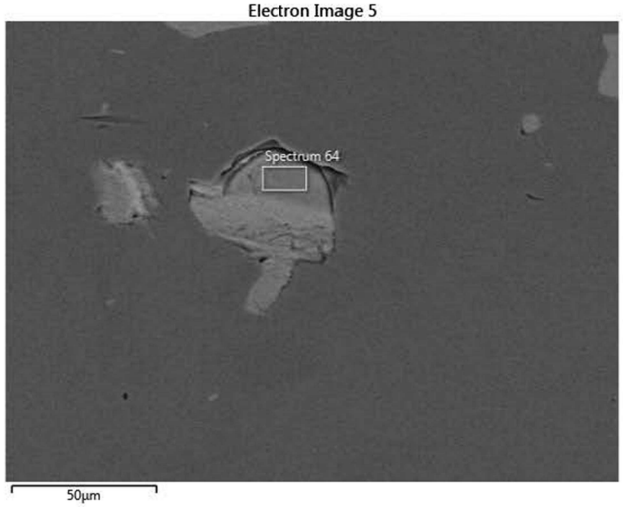

FN12974-4

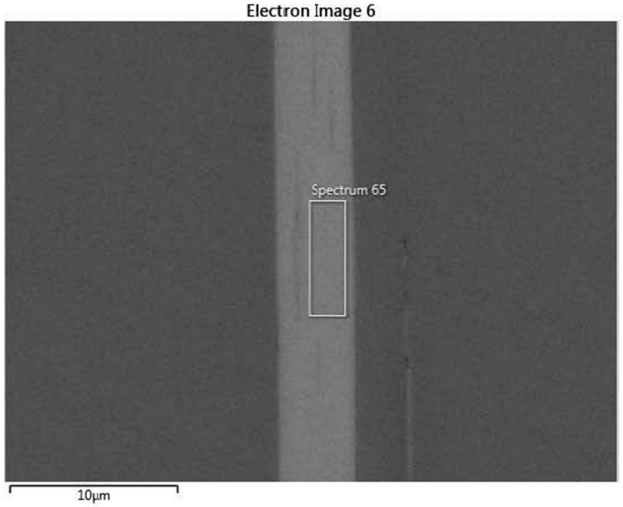

FN12974-5

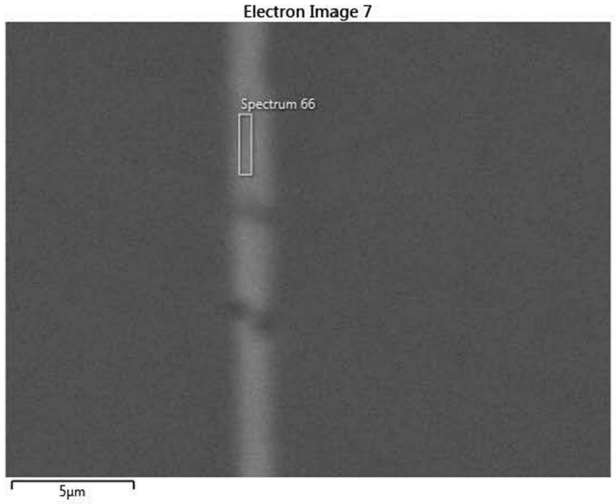

FN12974-6

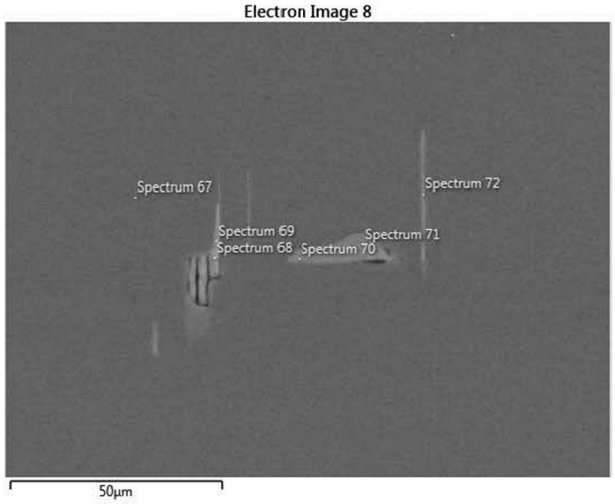

FN12974-7

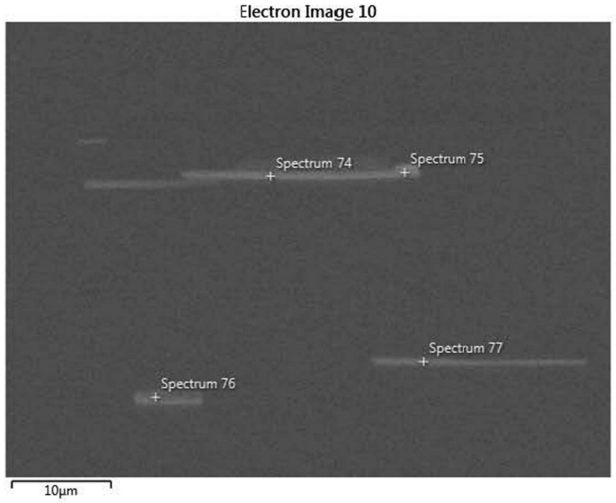

FN12974-9

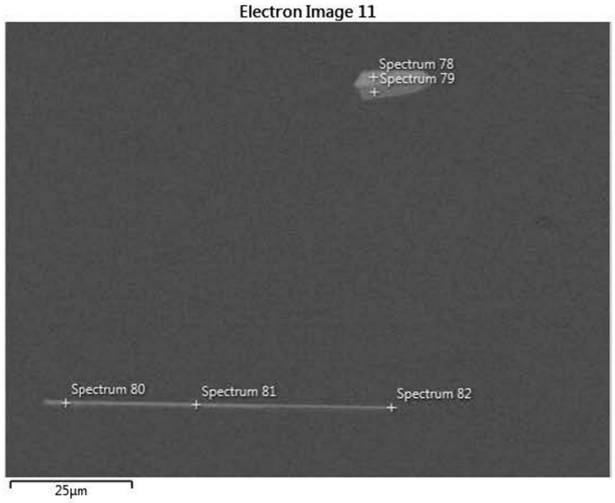

FN12974-10

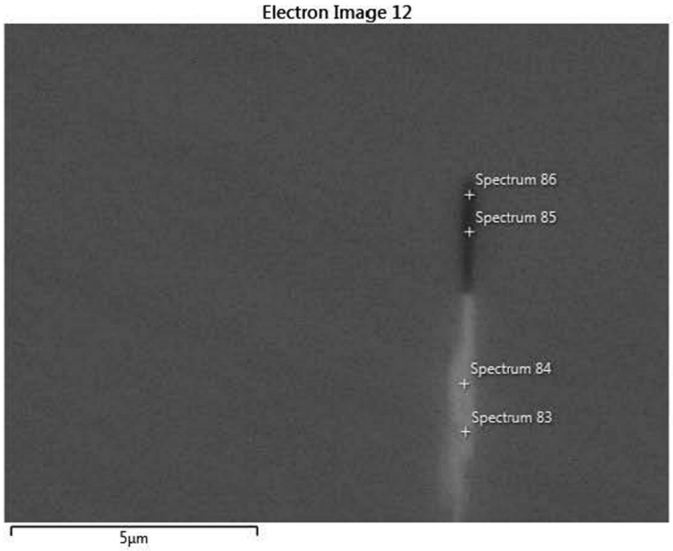

FN12974-11

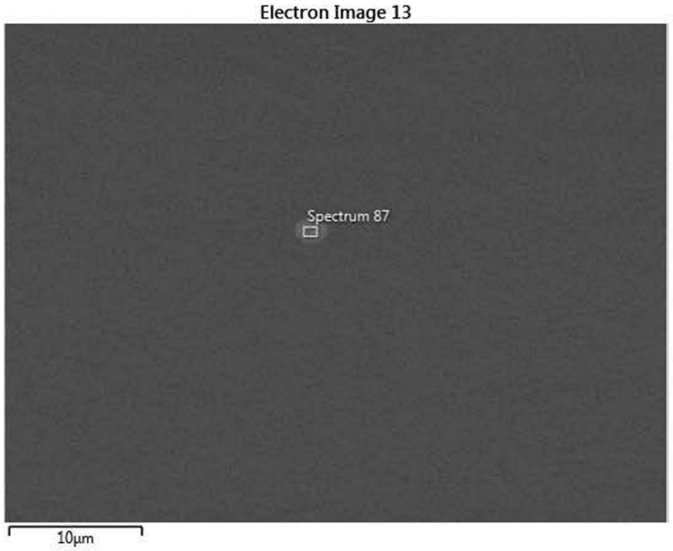

FN12974-12

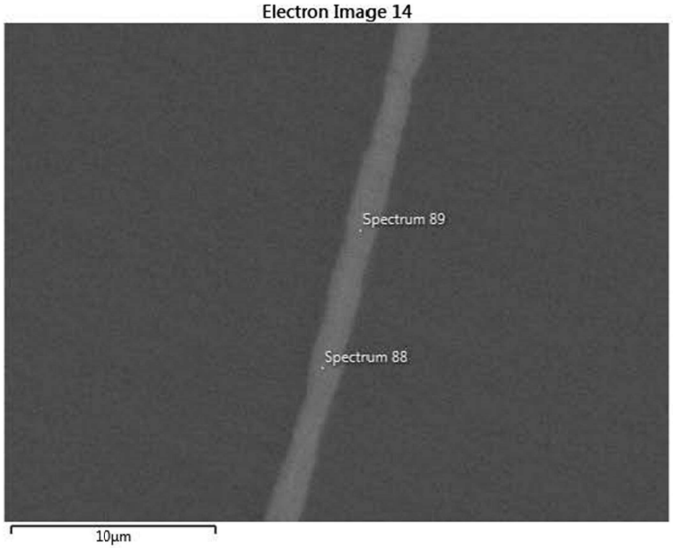

FN12974-13

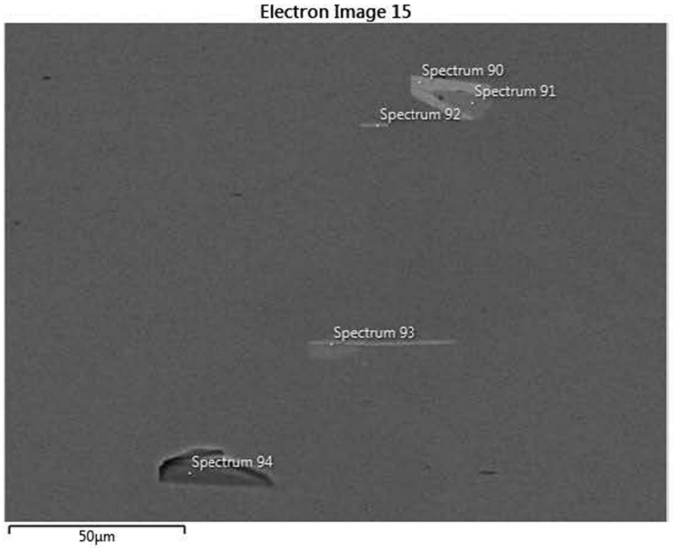

FN12974-14

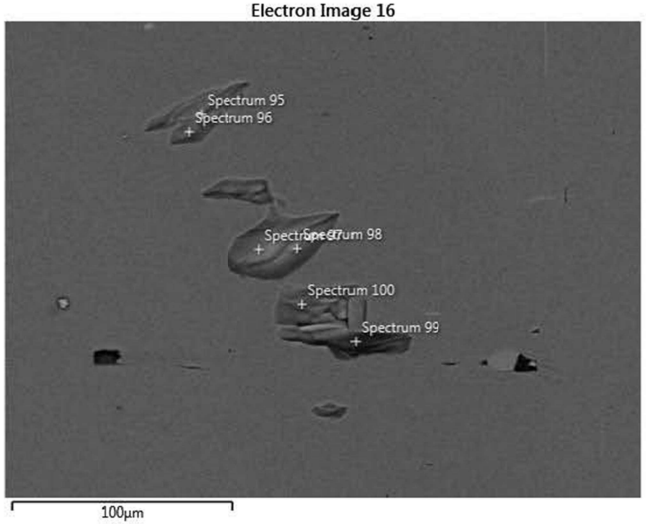

FN12974-15

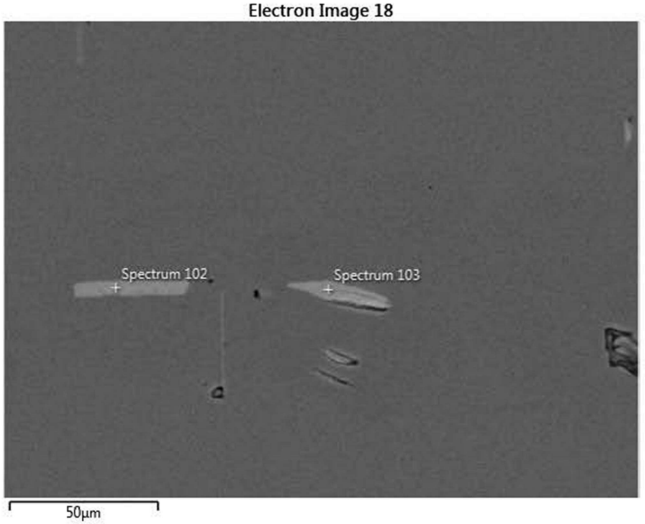

FN12974-17

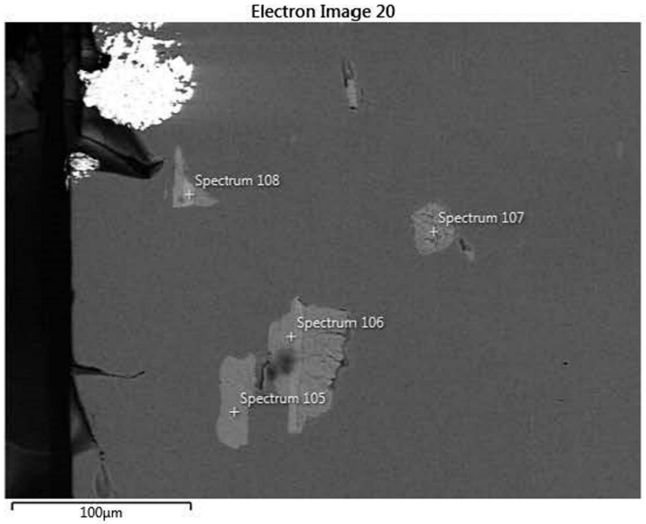

FN12974-19

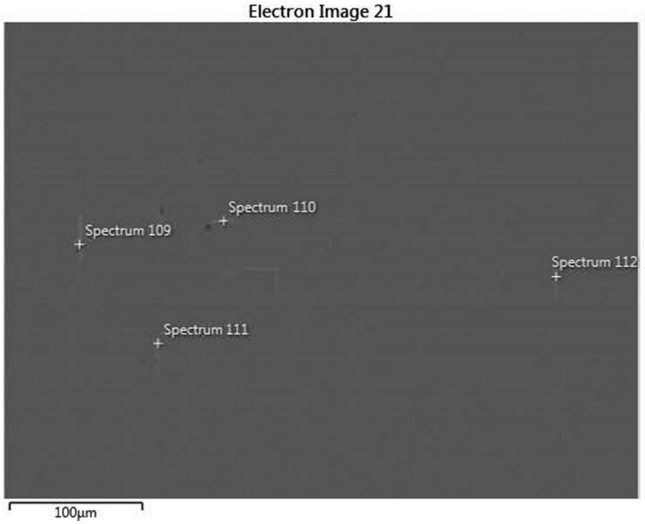

FN12974-20

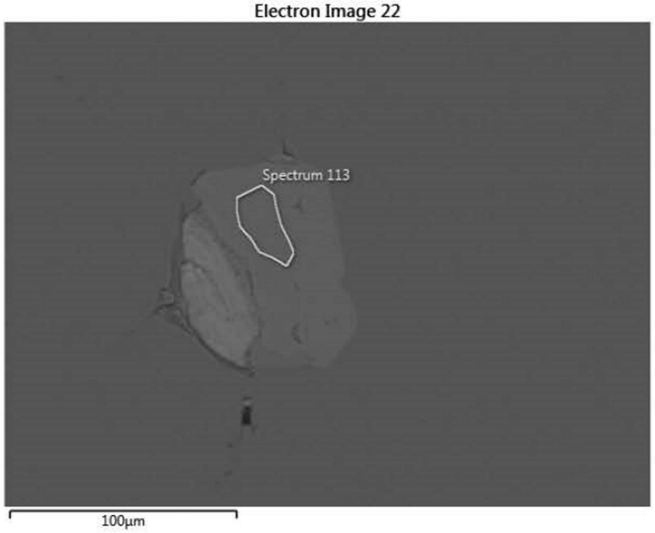

FN12974-21

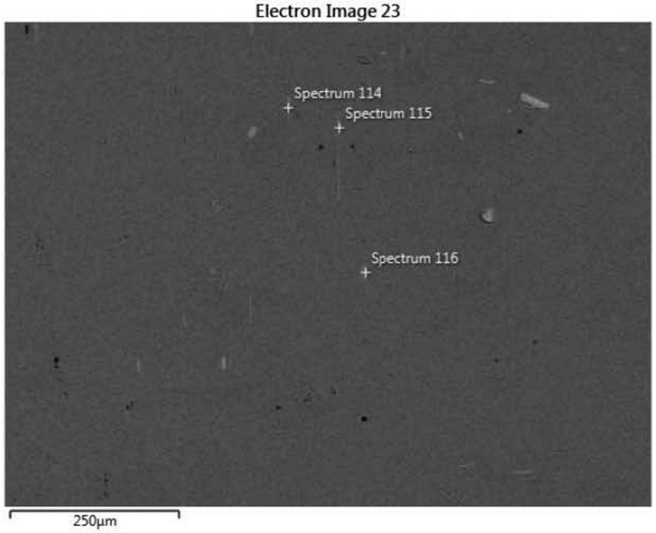

FN12974-22

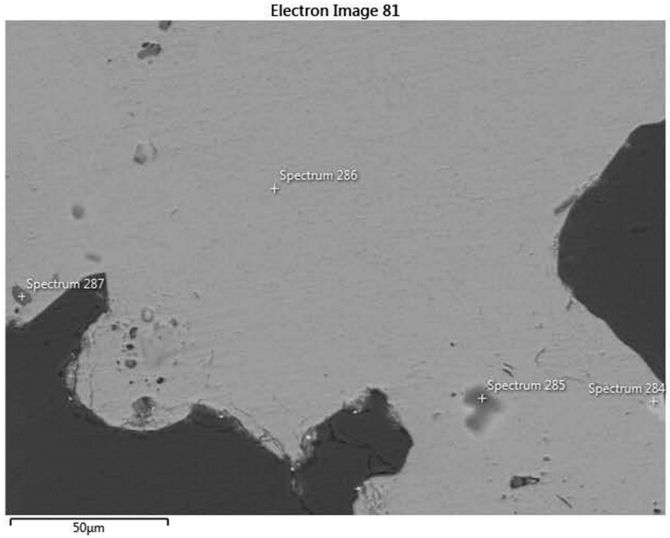

FN12975-1

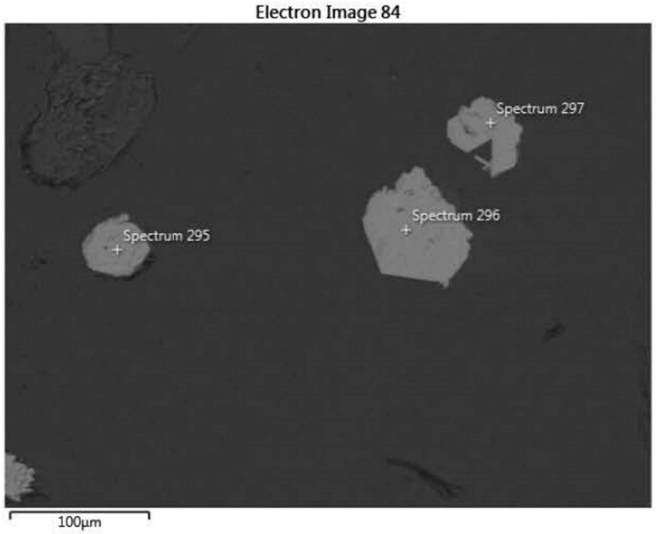

FN12976-1

Annex XIV: XRF analyses

Sample	FN12490	FN12968	FN12971	FN12973		FN12976		FN12977
Site	prism	prism	prism	prism	pinacoid	prism	core	prism
SiO_2	64,33	63,63	64,87	62,34	66,07	61,05	61,29	65,13
Al_2O_3	15,04	13,73	14,99	15,68	13,70	12,68	14,74	15,58
Fe_2O_3	1,50	2,58	1,11	2,08	1,98	2,34	2,84	1,33
MgO	3,07	3,26	2,96	3,23	3,24	7,51	4,69	2,82
CaO	0,07	0,04	0,03	1,33	0,07	0,04	0,09	0,00
Na_2O	1,16	0,95	1,22	1,23	0,83	0,55	0,91	1,07
MnO	0,02	0,03	0,02	0,04	0,01	0,03	0,04	0,01
Cr_2O_3	0,74	2,11	0,81	0,34	0,24	1,93	1,46	0,28
V_2O_5	0,20	0,03	0,21	0,14	0,17	0,13	0,18	0,08
Sc_2O_3	0,34	0,13	0,20	0,05	0,13	0,21	0,19	0,18
Rb_2O	0,00	0,00	0,00	0,00	0,00	0,00	0,01	0,00
Cs_2O	0,03	0,02	0,07	0,04	0,06	0,03	0,06	0,01
BeO (fixed)	13,50	13,50	13,50	13,50	13,50	13,50	13,50	13,50
Total	100,00	100,00	100,00	100,00	100,00	100,00	99,99	99,99

Sample	FN12978		FN12979		FN12980		FN12984
Site	prism	core	prism	pinacoid	prism	pinacoid	prism
SiO_2	61,10	65,18	65,92	61,50	61,58	61,40	65,73
Al_2O_3	17,47	13,06	13,22	20,19	14,17	16,45	13,23
Fe_2O_3	2,10	2,28	1,07	0,83	1,88	2,46	0,43
MgO	3,42	3,17	3,35	2,33	3,65	4,80	2,66
CaO	0,07	0,27	0,13	0,08	2,39	0,08	0,04
Na_2O	0,93	1,71	1,41	0,91	1,94	0,51	0,98
MnO	0,02	0,01	0,02	0,01	0,01	0,01	0,03
Cr_2O_3	0,89	0,33	1,12	0,44	0,58	0,50	2,69
V_2O_5	0,13	0,08	0,12	0,08	0,11	0,12	0,11
Sc_2O_3	0,35	0,39	0,11	0,06	0,08	0,13	0,61
Rb_2O	0,00	0,00	0,00	0,00	0,00	0,00	0,00
Cs_2O	0,03	0,02	0,03	0,07	0,11	0,03	0,01
BeO (fixed)	13,50	13,50	13,50	13,50	13,50	13,50	13,50
Total	100,01	100,00	100,00	100,01	100,00	99,99	100,00

Annex XV: EDX-SEM analyses on the emeralds samples (silicates)

Sample	FN12974	FN12974	FN12974	FN12974	FN12974	FN12974	FN12974	FN12974	FN12974
Site	1	3	4	5	7	7	7	7	7
Spectrum	53	plaquette	64	65	67	68	69	70	71
Mineral	emerald only	biotite	muscovite	muscovite-phengite	emerald only	biotite-phlogopite	biotite-phlogopite	dolomite	dolomite
SiO_2	76,87	52,67	49,63	50,97	77,14	52,11	53,79	6,2	
Al_2O_3	16,44	18,33	28,66	31,04	17,5	11,36	13,87		
FeO	1,35	6,76	3,91	3,53	0,6	9,57	9,25	9,37	8,7
MgO	3,09	15,7	2,74	2,7	2,67	21,24	16,48	31,69	34,68
CaO								51,02	56,62
Na_2O	2,24	1,36		0,92	2,09		0,67		
K_2O		5,18	13,02	10,84		5,72	5,94		
TiO_2									
MnO									
Cr_2O_3			2,04						
NiO									
ZrO_2									
P_2O_5									
SUM	99,99	100	100	100	100	100	100	98,28	100

Sample	FN12974	FN12974	FN12974	FN12974	FN12974	FN12974	FN12974	FN12974	FN12974
Site	7	9	9	10	10	10	10	10	11
Spectrum	72	74	75	78	79	80	81	82	83
Mineral	?	?	biotite	phlogopite	clinochlore	?	?	?	?
SiO_2	61,68	63,09	55,06	44,18	35,59	60,22	61,9	63,13	61,24
Al_2O_3	12,19	14,08	18,82	16,04	22,98	20,94	20,89	17,05	15,32
FeO	6,59	7,92	8,47	10,72	13,53	4,59	4,59	5,51	6,24
MgO	15,41	13,85	14,62	18	26,44	7,03	7,17	8,72	12,01
CaO									
Na_2O	1,38		1,02			1,01		1,45	1,28
K_2O	2,75		1,26	9,57	0,54	5,71	5,44	4,14	3,92
TiO_2				0,88					
MnO									
Cr_2O_3		1,05	0,76	0,61	0,91	0,5			
NiO									
ZrO_2									
P_2O_5									
SUM	100	99,99	100,01	100	99,99	100	99,99	100	100,01

Sample	FN12974	FN12974	FN12974	FN12974	FN12974	FN12974	FN12974	FN12974	FN12974
Site	11	12	13	13	14	14	17	17	19
Spectrum	84	87	88	89	90	91	102	103	105
Mineral	?	amphibole	diopside	diopside	muscovite	quartz	muscovite	phengite	clinochlore
SiO_2	61,7	45,37	34,37	28,32	51,48	100	51,49	51,56	34,17
Al_2O_3	15,31	10,22	7,67	6,78	30,07		29,69	29,4	23,13
FeO	6,26	4,8	6,43	7,57	3,33		2,82	3,23	13,87
MgO	11,57	15,55	18,77	20,31	3,29		2,87	3,46	28,83
CaO		23,2	30,81	35,36					
Na_2O	1,29	0,86	1,18	0,78	0,62		0,59		
K_2O	3,88				11,22		11,43	10,89	
TiO_2									
MnO			0,79	0,87					
Cr_2O_3							1,13	1,45	
NiO									
ZrO_2									
P_2O_5									
SUM	100,01	100	100,02	99,99	100,01	100	100,02	99,99	100

Sample	FN12974	FN12974	FN12974	FN12974	FN12974	FN12974	FN12974	FN12974	FN12974
Site	19	19	19	20	20	20	20	21	22
Spectrum	106	107	108	109	110	111	112	113	114
Mineral	clinochlore	clinochlore	phlogopite	muscovite	phengite	phengite	?	dolomite	?
SiO_2	34,99	33,91	42,26	56,2	52,36	53,31	61,22		66,64
Al_2O_3	23,88	22,34	17,04	29,22	30,49	29,6	24,34		21,28
FeO	13,51	14,52	10,86	2,32	2,82	2,81	2,56	6,31	1,83
MgO	26,98	28,29	18,84	2,2	2,51	2,67	2,32	35,89	1,75
CaO								57,8	
Na_2O					0,67	0,92	0,42		0,79
K_2O	0,64		10,36	10,07	10,42	10,05	9,15		7,7
TiO_2									
MnO									
Cr_2O_3		0,95	0,64		0,73	0,65			
NiO									
ZrO_2									
P_2O_5									
SUM	100	100,01	100	100,01	100	100,01	100,01	100	99,99

Sample	FN12974	FN12969	FN12969	FN12969	FN12969	FN12969	FN12969	FN12969	FN12969
Site	22	1	2	3	3	3	3	4	4
Spectrum	116	213	218	223	224	225	226	239	240
Mineral	phengite	biotite	biotite	clinochlore	clinochlore	clinochlore	clinochlore	clinochlore	clinochlore
SiO_2	53,52	44,97	44,81	33,26	32,91	32,17	33,39	33,36	33,45
Al_2O_3	30,13	13,95	13,41	23,25	22,71	22,8	22,45	23,47	22,75
FeO	2,54	10,89	11,76	14,93	16,35	16,89	15,72	14,76	15,97
MgO	2,43	20,72	18,69	27,37	26,7	26,65	26,97	27,7	26,97
CaO									
Na_2O	0,72								
K_2O	10,65		9,45						
TiO_2			1,44						
MnO									
Cr_2O_3		0,61	0,45	1,18	1,33	1,49	1,47	0,71	0,85
NiO									
ZrO_2									
P_2O_5									
SUM	99,99	91,14	100,01	99,99	100	100	100	100	99,99

Sample	FN12969	FN12969	FN12969	FN12969	FN12969	FN12973	FN12973	FN12970	FN12970
Site	4	6	6	6	6	1	2	2	8
Spectrum	241	259	260	261	262	276	281	310	342
Mineral	emerald only	zircon	zircon	zircon	zircon	clinochlore	rutile	emerald only	clinochlore
SiO_2	76,86	35,51	35,35	36,32	34,47	46,31	22,04	76,04	32,48
Al_2O_3	17,53			1,54		15,99	5,84	17,42	24,88
FeO	0,75					12,04	0,55	0,84	13,8
MgO	2,7					24,24	0,99	3,02	26,91
CaO									
Na_2O	2,16						1,03	2,69	
K_2O	8,86					1,02			
TiO_2							69,56		
MnO									
Cr_2O_3						0,4			1,31
NiO									0,63
ZrO_2		64,49	60,52	62,13	61,38				
P_2O_5			4,14		4,15				
SUM	108,86	100	100,01	99,99	100	100	100,01	100,01	100,01

Sample	FN12970	FN12970	FN12970	FN12970	FN12970	FN12970	FN12970	FN12970	FN12970
Site	10	13	14	16	16	17	17	19	1-bis
Spectrum	352	369	374	386	391	394	395	421	498
Mineral	muscovite	clinochlore	phlogopite	clinochlore	phlogopite	clinochlore	phengite	biotite	clinochlore
SiO_2	44,18	36,01	49,79	38,1	53,53	36,41	53,38	43,07	35,19
Al_2O_3	25,05	20,83	12,03	20,37	13,46	23,79	30,5	14,84	21,06
FeO	8,71	12,95	10,83	11,69	8,1	10,55	3,4	12,34	11,21
MgO	2,25	27,87	22,98	27,76	24,9	29,24		19,61	28,92
CaO									
Na_2O			0,84						
K_2O	19,81		1,44	2,08			12,71	9,72	
TiO_2									
MnO									
Cr_2O_3		1,4	1,04					0,41	2,83
NiO		0,94	1,06						0,79
ZrO_2									
P_2O_5									
SUM	100	100	100,01	100	99,99	99,99	99,99	99,99	100

Sample	FN12970	FN12970	FN12970	FN12970	FN12970	FN12970
Site	1-bis	1-bis	3-bis	5-bis	6-bis	9-bis
Spectrum	499	500	513	528	530	558
Mineral	clinochlore	clinochlore	talc	clinochlore	clinochlore	clinochlore
SiO_2	40,39	35,84	53,03	36,73	33,18	36,09
Al_2O_3	20,33	20,93	8,7	20,25	24,03	22,36
FeO	10,76	10,76	10,76	10,76	10,76	10,76
MgO	25,15	28,08	24,24	26,81	26,44	29,34
CaO						
Na_2O			3,12			
K_2O			0,8			
TiO_2						
MnO						
Cr_2O_3	2,55	2,66	0,72	1,56	1,12	0,81
NiO	0,81	0,88	1,01	0,81	0,53	0,75
ZrO_2						
P_2O_5						
SUM	99,99	99,15	102,38	96,92	96,06	100,11

Annex XVI: EDX-SEM analyses on the emeralds samples (sulfurs & oxides)

Sample	FN12975	FN12975	FN12975	FN12976	FN12976	FN12976	FN12974
Site	1	1	1	1	1	1	21
Spectrum	284	286	287	295	296	297	182
Mineral	chalcopyrite	pyrite	goethite	(V-Zn)-ferritchromite	ferritchromite	ferritchromite	halite
SiO_2							44,25
Al_2O_3				4,2	4,27	4,78	12,5
FeO			85,26	43,07	43,94	45,54	5,375
MgO			9,95				4
CaO			0,5				
Cr_2O_3			0,69	50,58	50,63	48,7	0,625
V_2O_5				1,13	1,16	0,97	
Sc_2O_3							1,125
TiO_2							0,875
ZnO				1,03			
Na_2O							12,75
Cl							18,25
Cu	26,16						
Fe	25,98	34,37					
S	47,86	65,63	3,62				
SUM	100	100	100,02	100,01	100	99,99	99,75

Annex XVII: EDX-SEM analyses on the rock samples collected in Mingora (April 2019)

1

sample	A% (O)	A% (Mg)	A% (Al)	A% (Si)	A% (Fe)	A% (Ni)	A% (W)	Mg/Si	O/Mg	O/Si	Fe/Si	W/Si
1	66.12	15.54	0.39	17.31	0.44	0.12	0.07	0.89774697	4.25482625	3.81975737	0.02541883	0.00404391
2	65.89	15.24	0.31	17.66	0.64	0.12	0.13	0.86296716	4.32349081	3.73103058	0.03624009	0.00736127
3	64.64	15.52	0.14	18.67	0.61	0.15	0.27	0.83128013	4.16494845	3.46223889	0.03267274	0.0144617
4	67.7	14.63	0.29	14.67	0.49	0.11	0.6164	0.99727335	4.62747779	4.61486026	0.0334015	0.04201772
5	62.92	16.09	0.31	19.94	0.53	0.1	0.12	0.80692076	3.91050342	3.1554664	0.02657974	0.00601805
zoom particule	58.81	17.02	0.08	22.37	0.92	0.16	0.64	0.76084041	3.45534665	2.62896737	0.04112651	0.02860975
grain 6	63.7	16.09	0.24	19.27	0.47	0.12	0.12	0.83497665	3.95898073	3.30565646	0.02439024	0.0062273
point 2	63.23	16.48	0.25	19.27	0.5	0.14	0.13	0.85521536	3.83677184	3.28126622	0.02594707	0.00674624
point 3	63.83	15.96	0.25	18.98	0.62	0.14	0.22	0.84088514	3.99937343	3.3630137	0.03266596	0.01159115
point 4_particule	66.05	15.61	0.26	16.11	0.53	0.14	1.29	0.96896338	4.23126201	4.09993793	0.03289882	0.08007449
point5_particule	73.27	10.29	0.47	7.22	0.68	0.25	7.81	1.42520776	7.12050534	10.1481994	0.09418283	1.08171745
zone3 point1	64.32	16.49	0.74	12.09	6.03	0.13	0.21	1.36393714	3.90054579	5.32009926	0.49875931	0.01736973
Zone3 point2	67.12	21.57	0.08	7.16	3.02	0.36	0.7	3.01256983	3.11172925	9.37430168	0.42178771	0.09776536
Zone3 point3	62.94	15.82	0.21	19.14	0.64	0.43	0.83	0.82654127	3.97850822	3.28840125	0.03343783	0.04336468
Zone3 point4	65.59	15.73	0.82	16.88	0.68	0.16	0.14	0.93187204	4.16973935	3.88566351	0.04028436	0.00829384
zone 3 global	67.35	15.51	0.21	14.22	1.65	0.36	0.7	1.0907173	4.34235977	4.73628692	0.11603376	0.04922644

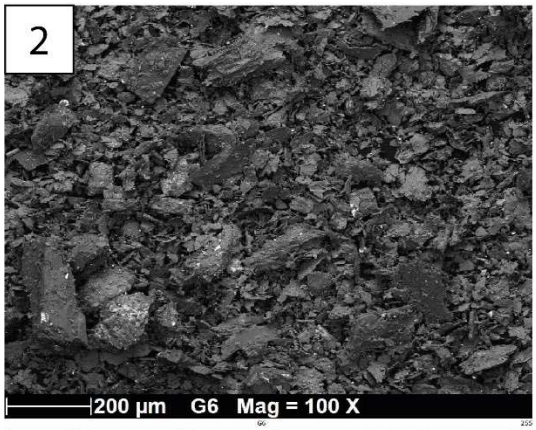

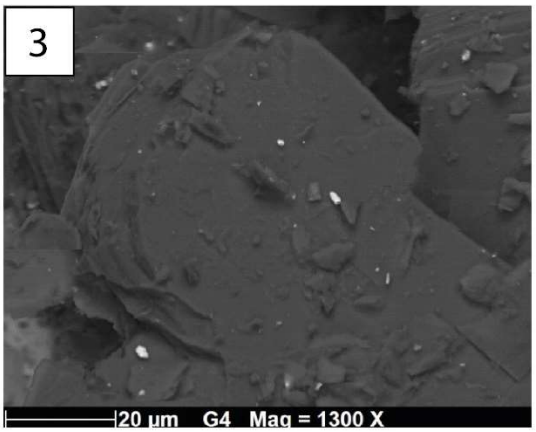

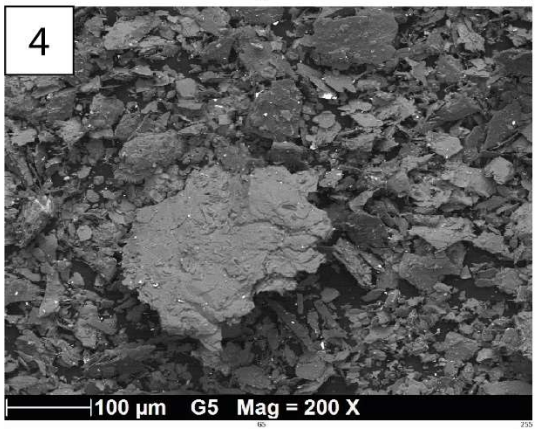

*Figure 48: EDX-SEM results for the analyses on the rock samples. **1**) Table of the completed qualitative analyses with EDX-SEM on the powders of LC-center-1, LC-center-2, LC-khalid-2 rock samples. The Mg-Si-O composition of the grains displays large range of Mg/Si ratio, it could be a mix of derivated pyroxenes (MgSiO3) and talc (Mg4Si3O12) with variable Mg/Si ratio. **2**) Platy shapes of the particles influences the qualitative analyses cited above (sample LC-center-2). **3**) Another view of the sample LC-center-2. **4**) The smaller and denser grains on the platy minerals is potentially a contamination during the sampling (sample LC-center-2).*

Annex XVIII: EPMA analyses on emerald samples

Sample	FN12976	FN12976	FN12976	FN12976	FN12976	FN12491	FN12491	FN12491	FN12491
Site	core	core	core	rim	rim	core	core	rim	rim
Spectrum	1	2	3	1	2	1	2	1	2
Mineral	talc	?	quartz	talc	talc	talc	talc	phlogopite	clinochlore
SiO_2	61,88	56,76	102,11	62,69	62,89	62,69	60,65	51,63	28,96
Al_2O_3	0,3979	0,4149	0,0501	0,2765	0,3148	5,18	8,36	3,42	19,35
FeO	4,09	4,08	0,0693	3,67	3,81	3,08	2,27	3,36	11,6
MgO	27,54	27,55	0,0105	28,23	28,19	19,67	12,23	21,13	24,62
CaO	0,0104	0,0218	0,0033	0	0,0132	0	0,0014	0,0284	0,03
Na_2O	0,0709	0,0807	0,0044	0,0498	0,0464	0,6483	1,2587	0,5613	0,0053
K_2O	0,0138	0,018	0,0007	0,017	0,0181	0,0012	0,004	0,0369	0,0366
TiO_2	0,0298	0	0	0	0,0166	0	0,0054	0,0025	0,0325
MnO	0,0129	0,0117	0	0	0,0191	0,0308	0,0067	0,0146	0,0787
SUM	94,0458	88,9372	102,2483	94,9333	95,3182	91,3003	84,7863	80,1838	84,7131

Sample	FN12978	FN12978	FN12978	FN12978	FN12978	FN12978	FN12978	FN12978	FN12978
Site	core	core	core	core	half	half	rim	rim	rim
Spectrum	1	2	3	4	2	3	1	2	3
Mineral	phlogopite	clinochlore	clinochlore	biotite	clinochlore	clinochlore	clinochlore	biotite	clinochlore
SiO_2	48,05	29,76	27,97	41,81	30,39	30,14	29,68	40,17	30,32
Al_2O_3	15,75	19,24	21,35	17,61	18,72	18,9	19,77	16,07	19,33
FeO	5,87	11,48	11,95	8,37	10,04	10,39	10,36	8,72	9,14
MgO	13,47	25,17	22,98	18,25	25,68	25,35	25,33	19,54	26,63
CaO	0,0341	0,0072	0,0474	0,004	0,008	0,0896	0,0241	0,0389	0,0512
Na_2O	1,0413	0,0002	0,0129	0,6891	0,0011	0,0011	0,0135	0,1592	0,0061
K_2O	0,044	0,0051	0,0412	0,0107	0	0	0,0241	4,93	0,0167
TiO_2	0,0222	0,0152	0,0304	0,0049	0,0176	0,0213	0,0459	0,1482	0,0177
MnO	0,0601	0,0865	0,0945	0,0797	0,1025	0,0937	0,0683	0,0525	0,0669
SUM	84,3418	85,7642	84,4764	86,8284	84,9593	84,9857	85,316	89,8288	85,5787

Sample	FN12491	FN12969	FN12969	FN12969	FN12969	FN12969	FN12969	FN12969	FN12969
Site	rim	core	core	core	core	rim	rim	rim	rim
Spectrum	3	1	2	4	5	1	2	3	4
Mineral	talc	clinochlore	muscovite	clinochlore	quartz	clinochlore	clinochlore	biotite	clinochlore
SiO_2	61,15	29,71	49,24	29,47	95,12	30,17	29,05	38,93	28
Al_2O_3	0,2179	19,51	29,66	19,63	3,16	18,63	19,66	18,94	19,74
FeO	4,23	11,05	2,13	11,05	0,2359	12,39	11,73	9,15	11,68
MgO	27,3	24,72	2,82	24,77	0,5303	24,04	24,11	19,28	22,61
CaO	0,0008	0,0155	0,011	0,0259	0,0142	0,0151	0,0298	0,0058	0,0225
Na_2O	0,041	0,0103	0,5576	0,0107	0,4857	0	0,0195	0,5508	0,0016
K_2O	0,0118	0,0197	10,36	0,0188	0,0179	0,57	0,0258	0,0022	0
TiO_2	0,0133	0,0002	0,0867	0,0265	0,0172	0,0458	0,0325	0,0229	0,0794
MnO	0,0313	0,1063	0,0173	0,0897	0	0,0215	0,0644	0,0615	0,0849
SUM	92,9962	85,1421	94,8827	85,0917	99,5813	85,8824	84,7221	86,9433	82,2184

Sample	FN12974	FN12974	FN12974	FN12974	FN12974	FN12974	FN12974	FN12974
Site	core	core	rim	rim	rim	rim	rim	rim
Spectrum	2	3	1	2	3	4	5	6
Mineral	quartz	muscovite	clinochlore	quartz	clinochlore	clinochlore	clinochlore	clinochlore
SiO_2	102,18	47,38	29,46	99,41	28,36	28,13	28,89	32,22
Al_2O_3	0,0374	30,4	19,73	2,29	20,21	19,58	19,34	16,79
FeO	0,0756	2,16	11,22	0,3444	12,41	12,27	11,28	10,7
MgO	0,0023	2,46	24,91	0,2624	23,39	22,85	24,63	17,36
CaO	0,0064	0,0431	0,0219	0	0,0372	0,0532	0,0214	0,0251
Na_2O	0,0033	0,6115	0,005	0,0304	0,0241	0,0341	0,0036	0,0495
K_2O	0,0065	10,23	0,0034	0,7237	0,0095	0,0513	0,0084	5,32
TiO_2	0,0095	0,1991	0,0304	0,0082	0,0489	0,0375	0,0156	0,1054
MnO	0	0,0017	0,0973	0	0,0944	0,0858	0,0948	0,0824
SUM	102,3209	93,4855	85,4781	103,0691	84,5841	83,092	84,2839	82,6525

Annex XIX: Paragenetic diagrams before merging

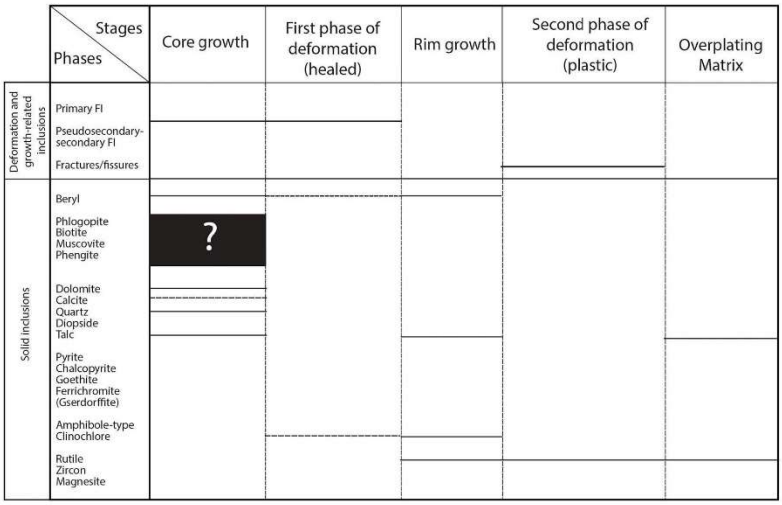

FN12491

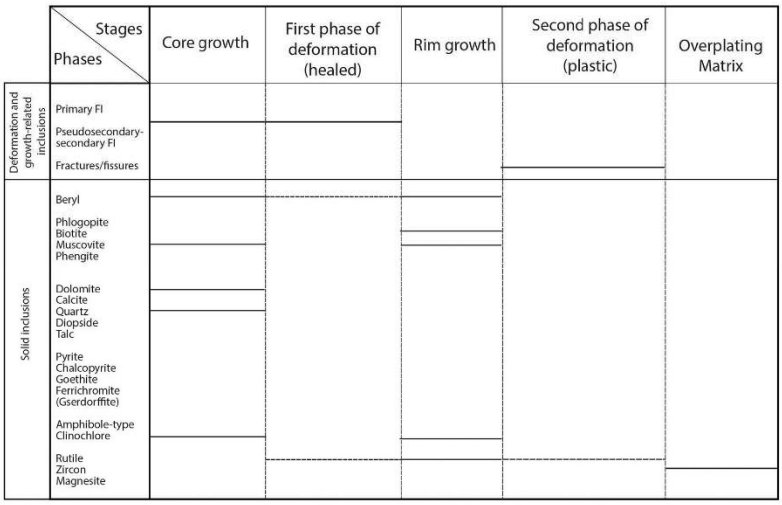

FN12969

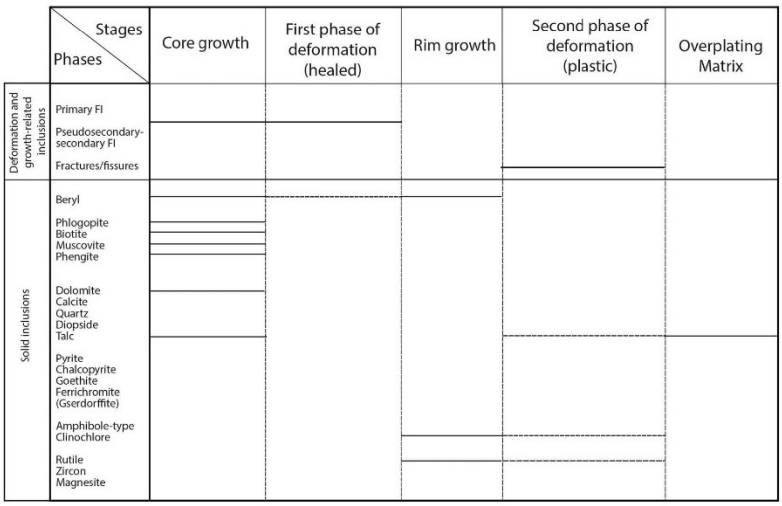

FN12970

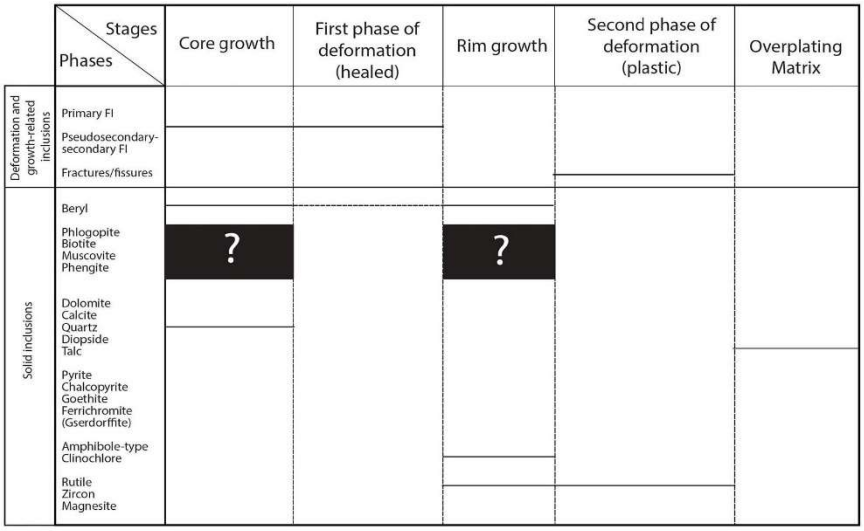

FN12971

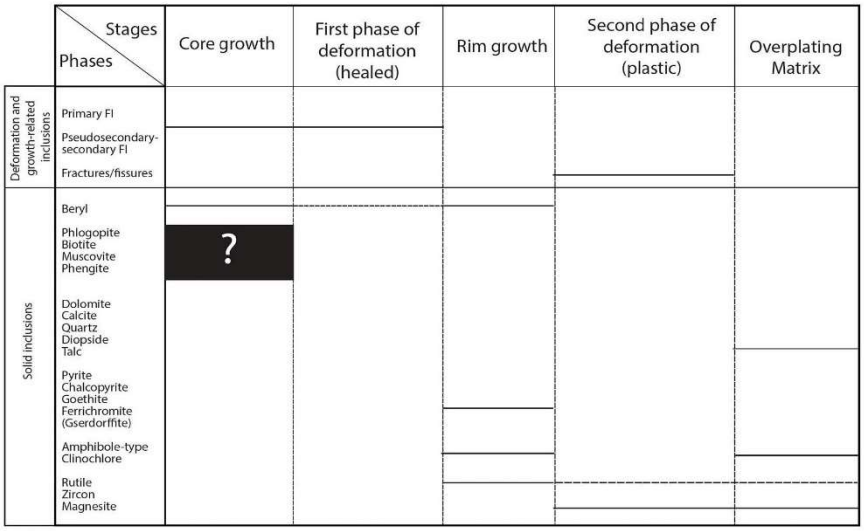

FN12972

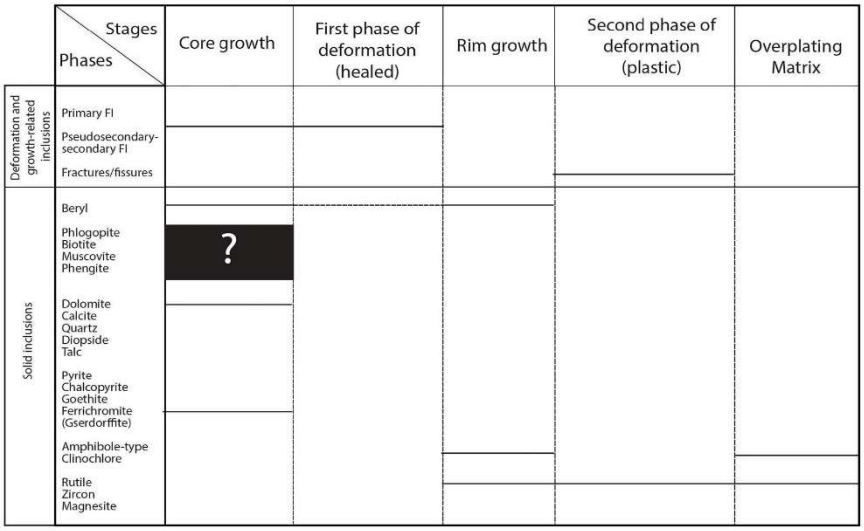

FN12973

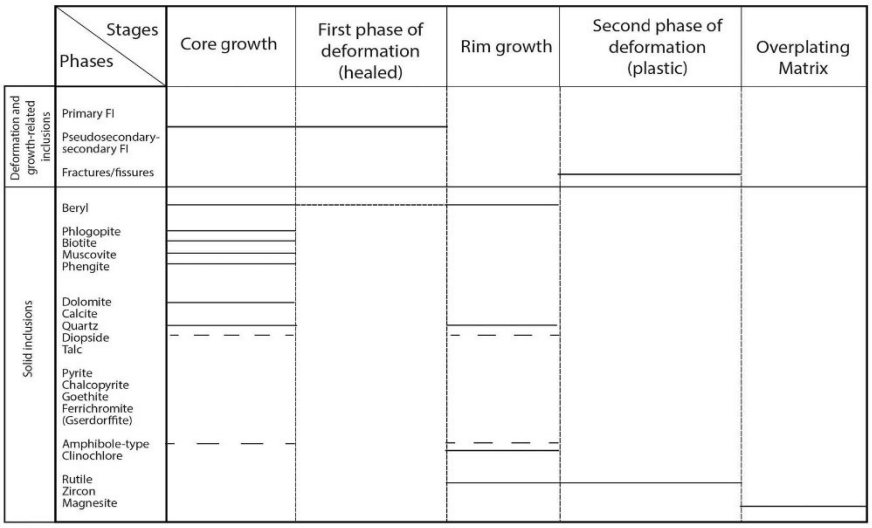

FN12974

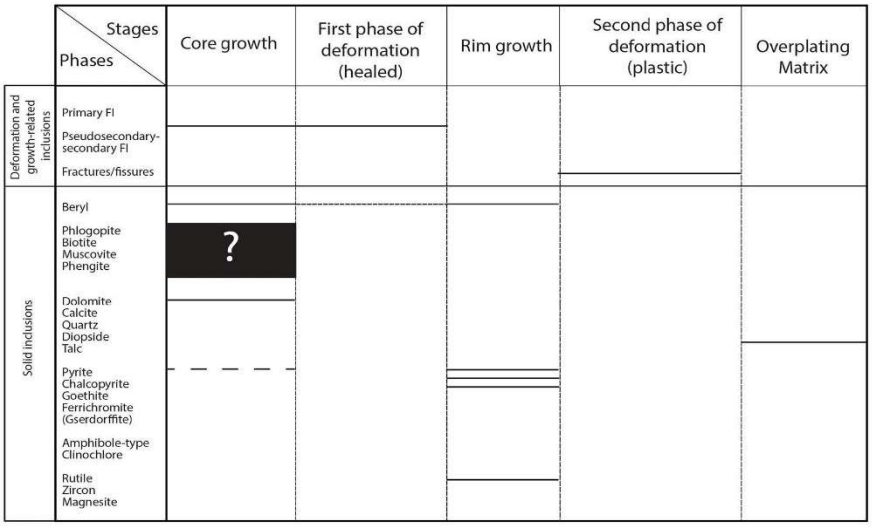

FN12975

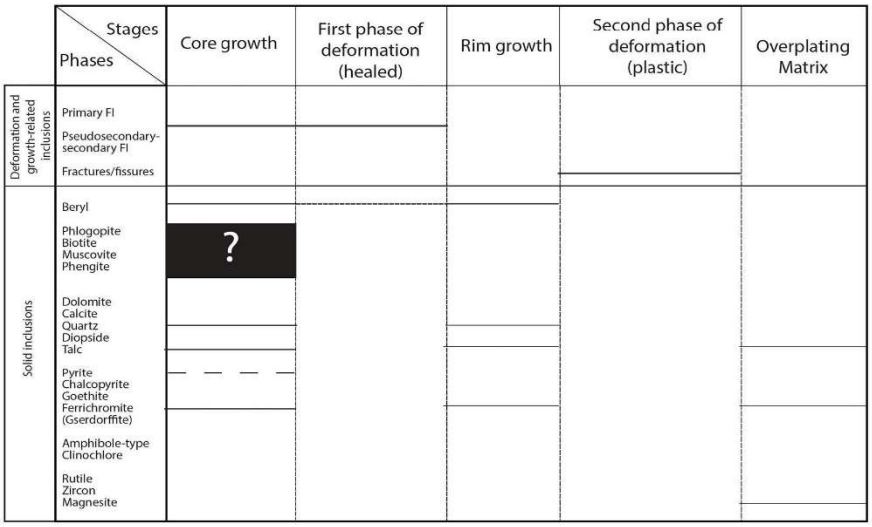

FN12976

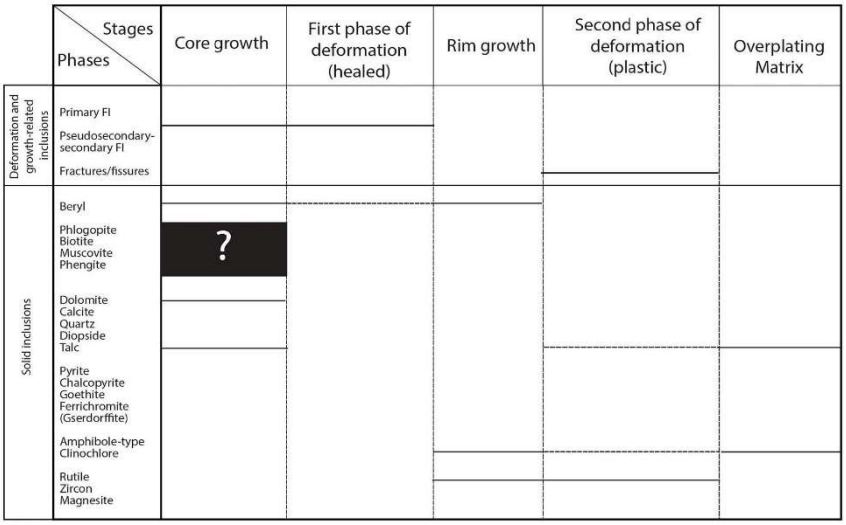

FN12977

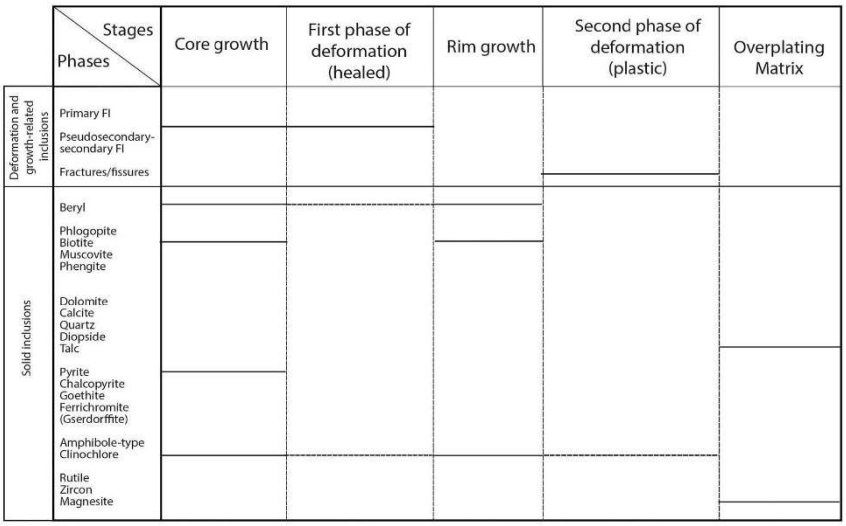

FN12978

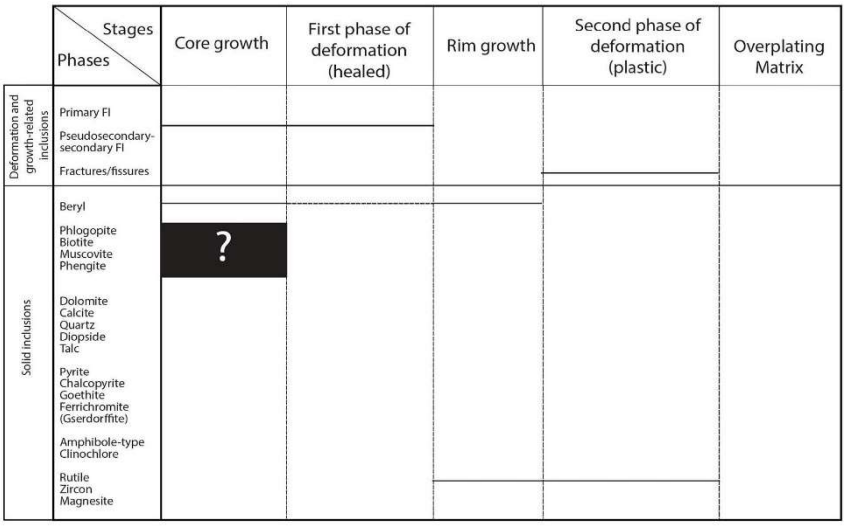

FN12979

Annex XX: Cr-bearing inclusions and concentration by EDX-SEM analyses

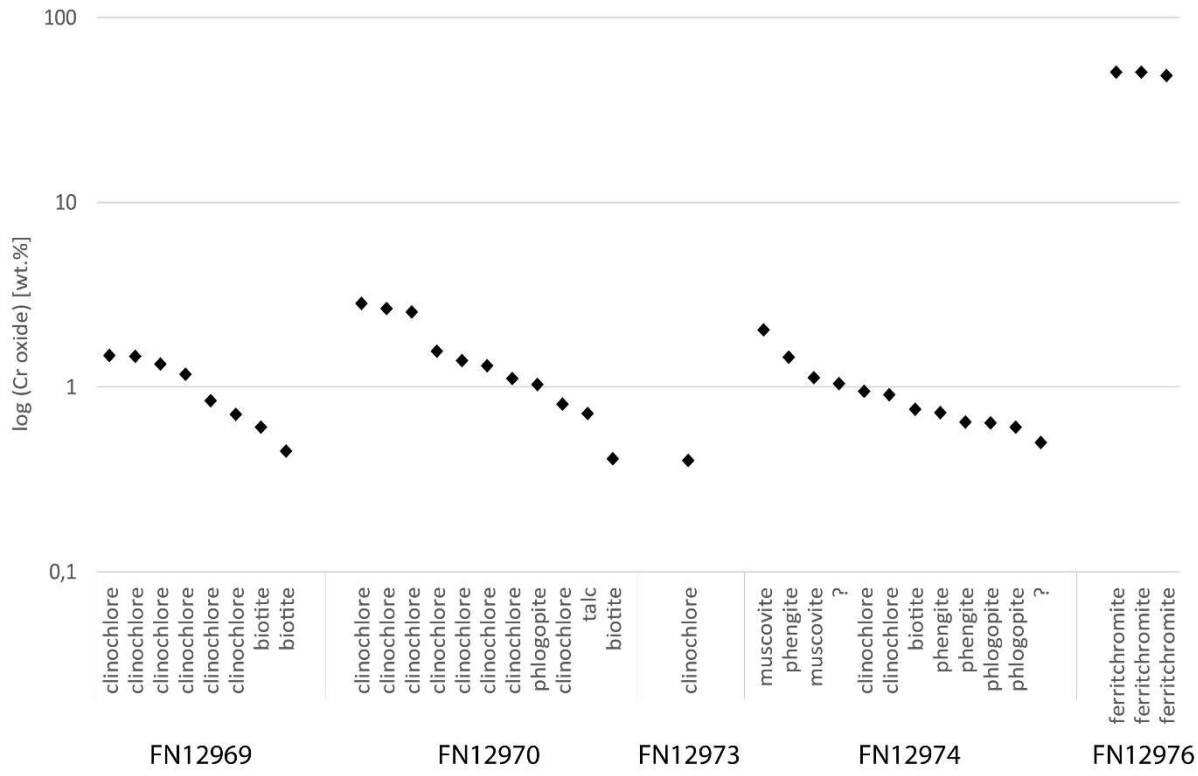

Figure 49: log Cr-oxide concentration in Cr-bearing inclusions, analyzed by EDX-SEM

Annex XXI: Chlorite thermometer

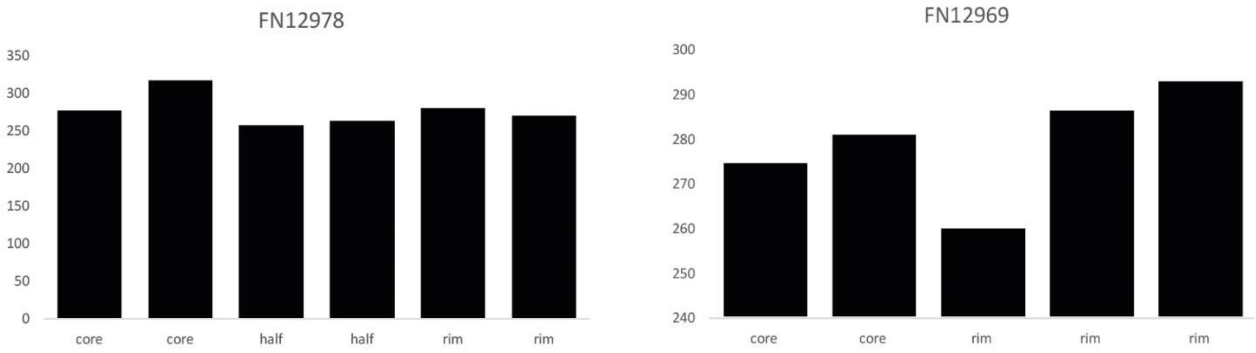

Figure 50: Chlorite temperatures (Cathelineau, 1988). The distribution between the core and the rim are homogenous and do not show a temperature gradient

Annex XXII: Major, minor (and trace) elements concentrations core to rim by EPMA

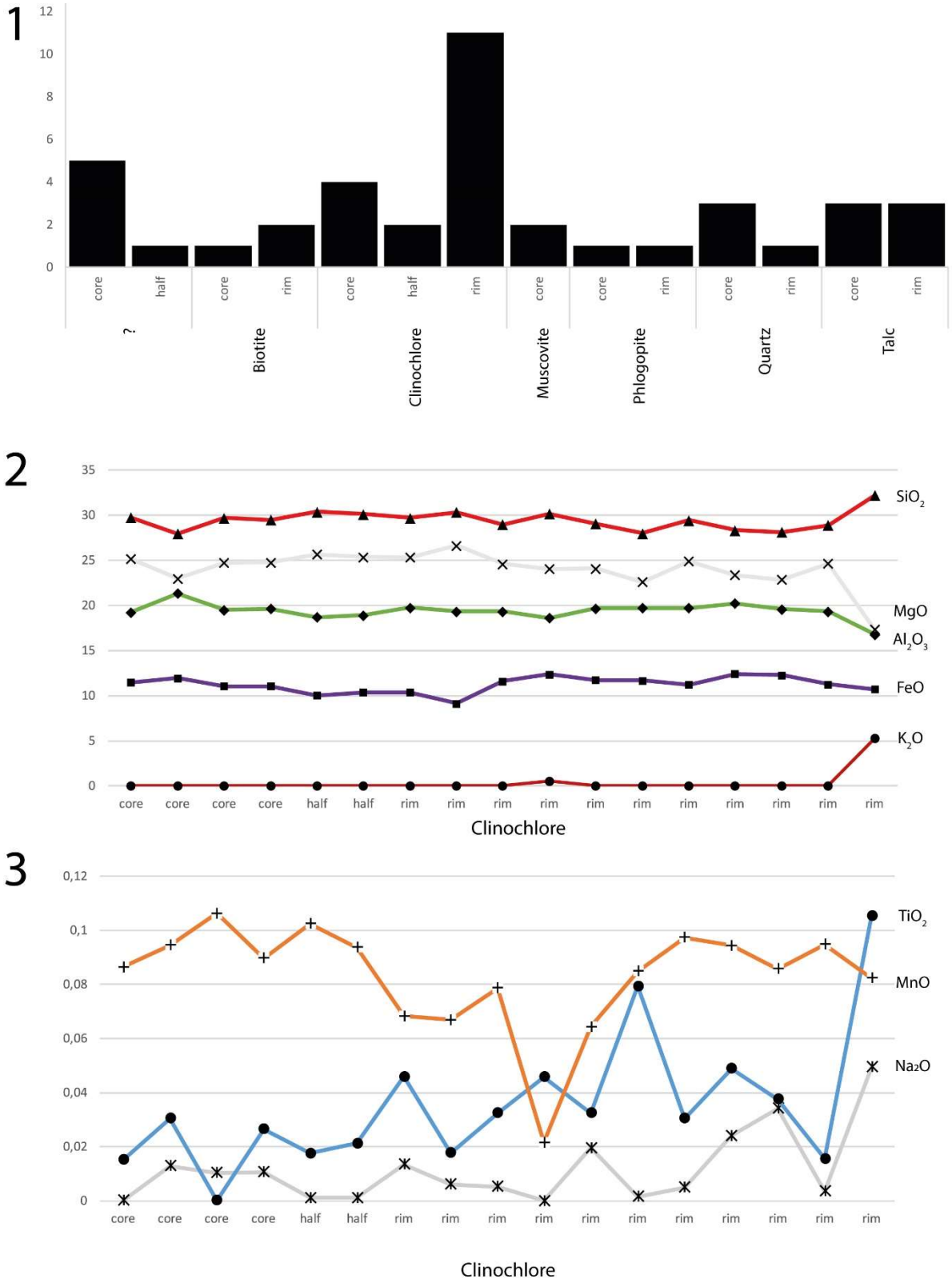

*Figure 51: **1**) Core, half-way, rim sectors and the relative distribution of the inclusions analyzed by microprobe. **2**) Major elements concentrations in the samples analyzed by microprobe, organized by sector. **3**) Minor (and trace) elements in concentrations in the samples analyzed by microprobe, organized by sector.*

Annex XXIII: Preparation of the emerald samples and location of the analyses

Sample number	Modifications of the sample	Microscopic observations	IR Spectrometry	UV-VIS-NIR Spectometry	ED-XRF	XRD	FT-Raman Spectrometry	Laser Raman Microspectrometry	EDX-SEM	EPMA
FN12490		GGTL Geneva	Nantes University	GGTL Geneva	GGTL Geneva					
FN12491	Polished Sawn A slice casted in epoxy	GGTL Geneva	Nantes University	GGTL Geneva	GGTL Geneva		Nantes University	Lausanne University	Lausanne University	Lausanne University
FN12968	Polished	GGTL Geneva		GGTL Geneva	GGTL Geneva					
FN12969	Polished Sawn in half Half casted in epoxy	GGTL Geneva		GGTL Geneva	GGTL Geneva			Lausanne University		Lausanne University
FN12970	Broken at polishing Crushed	GGTL Geneva				Lausanne University		Lausanne University	Lausanne University	
FN12971	Polished	GGTL Geneva						Lausanne University		
FN12972		GGTL Geneva		GGTL Geneva	GGTL Geneva			Lausanne University		
FN12973	Polished	GGTL Geneva		GGTL Geneva	GGTL Geneva			Lausanne University	Lausanne University	
FN12974	Polished Sawn in half Half casted in epoxy	GGTL Geneva		GGTL Geneva	GGTL Geneva			Lausanne University	Lausanne University	Lausanne University
FN12975	Polished	GGTL Geneva		GGTL Geneva	GGTL Geneva			Lausanne University	Lausanne University	
FN12976	Polished Sawn A slice casted in epoxy	GGTL Geneva		GGTL Geneva	GGTL Geneva					Lausanne University
FN12977	Polished	GGTL Geneva		GGTL Geneva	GGTL Geneva			Lausanne University		
FN12978	Polished Sawn A slice casted in epoxy	GGTL Geneva								Lausanne University
FN12979		GGTL Geneva		GGTL Geneva	GGTL Geneva			Lausanne University		
FN12980	Polished	GGTL Geneva		GGTL Geneva	GGTL Geneva			Lausanne University		
FN12981		GGTL Geneva		GGTL Geneva	GGTL Geneva					
FN12984		GGTL Geneva		GGTL Geneva	GGTL Geneva					
FN13153		GGTL Geneva		GGTL Geneva	GGTL Geneva					
FN13155		GGTL Geneva		GGTL Geneva	GGTL Geneva					
FN13156		GGTL Geneva		GGTL Geneva	GGTL Geneva					

Annex XXIV: Preparation of the rock samples and location of the analyses

Sample number	Modifications of the sample	Thin-sections	XRD	EDX-SEM
LC-khalid-1				
LC-khalid-2	Crushed		Nantes University	Nantes University
LC-khalid-3				
LC-khalid-4				
LC-khalid-5	Sawn	Nantes University		
LC-khalid-6	Sawn	Nantes University		
LC-khalid-7	Sawn	Nantes University		
LC-khalid-8	Sawn	Nantes University		
LC-khalid-9	Sawn	Nantes University		
LC-khalid-10				
LC-khalid-11				
LC-khalid-12				
LC-center-1	Crushed		Nantes University	Nantes University
LC-center-2	Crushed		Nantes University	Nantes University
LC-center-3				